

University of Alberta

**Aspects of the Thermo Elasto-Plastic Response for a Coke Drum
under Cyclic Loading**

by

John J. Aumuller, P. Eng.

A thesis submitted to the Faculty of Graduate Studies and Research
in partial fulfillment of the requirements for the degree of

Master of Science

in

Applied Mechanics

Mechanical Engineering

© John J. Aumuller

Fall 2009

Edmonton, Alberta

Permission is hereby granted to the University of Alberta Libraries to reproduce single copies of this thesis and to lend or sell such copies for private, scholarly or scientific research purposes only. Where the thesis is converted to, or otherwise made available in digital form, the University of Alberta will advise potential users of the thesis of these terms.

The author reserves all other publication and other rights in association with the copyright in the thesis and, except as herein before provided, neither the thesis nor any substantial portion thereof may be printed or otherwise reproduced in any material form whatsoever without the author's prior written permission.



Library and Archives
Canada

Published Heritage
Branch

395 Wellington Street
Ottawa ON K1A 0N4
Canada

Bibliothèque et
Archives Canada

Direction du
Patrimoine de l'édition

395, rue Wellington
Ottawa ON K1A 0N4
Canada

Your file Votre référence
ISBN: 978-0-494-81315-7
Our file Notre référence
ISBN: 978-0-494-81315-7

NOTICE:

The author has granted a non-exclusive license allowing Library and Archives Canada to reproduce, publish, archive, preserve, conserve, communicate to the public by telecommunication or on the Internet, loan, distribute and sell theses worldwide, for commercial or non-commercial purposes, in microform, paper, electronic and/or any other formats.

The author retains copyright ownership and moral rights in this thesis. Neither the thesis nor substantial extracts from it may be printed or otherwise reproduced without the author's permission.

AVIS:

L'auteur a accordé une licence non exclusive permettant à la Bibliothèque et Archives Canada de reproduire, publier, archiver, sauvegarder, conserver, transmettre au public par télécommunication ou par l'Internet, prêter, distribuer et vendre des thèses partout dans le monde, à des fins commerciales ou autres, sur support microforme, papier, électronique et/ou autres formats.

L'auteur conserve la propriété du droit d'auteur et des droits moraux qui protègent cette thèse. Ni la thèse ni des extraits substantiels de celle-ci ne doivent être imprimés ou autrement reproduits sans son autorisation.

In compliance with the Canadian Privacy Act some supporting forms may have been removed from this thesis.

While these forms may be included in the document page count, their removal does not represent any loss of content from the thesis.

Conformément à la loi canadienne sur la protection de la vie privée, quelques formulaires secondaires ont été enlevés de cette thèse.

Bien que ces formulaires aient inclus dans la pagination, il n'y aura aucun contenu manquant.


Canada

Examining Committee

Dr. Zihui Xia, Department of Mechanical Engineering

Dr. Yongsheng Ma, Department of Mechanical Engineering

Dr. Samer Adeeb, Department of Civil and Environmental Engineering

ABSTRACT

The financial viability of the Canadian oil sands industry is due in large part to the successful operation of upgrading facilities and the delayed coking unit which converts petroleum residuum into lighter liquid and gas products.

Since the development of this technology in the 1940's, a major source of unit failure has been drum shell cracking. There are very few studies in the open literature investigating the root cause, the mitigation of this failure mechanism and remaining life prediction.

In this work, the focus is on the thermo mechanical loading and its impact. Reconciliation with the available field data suggests that the field data is problematic, leading to an underreporting of the damage.

By the use of closed form expressions and non-linear, temperature dependant numerical modeling, understanding of the failure mode is improved and alternate approaches are possible to evaluate structure performance.

ACKNOWLEDGEMENTS

Sincere thanks are extended to Dr. Zihui Xia for his patience, guidance and enthusiasm to pursue these studies. I am indebted to his confidence and encouragement to persevere. Many thanks are extended to my colleague, Jie Chen and to Dr. Xejian Jiang, Dr. Feng Ju, and Dr. Yunfa Zhang for their kind assistance and patient support.

A very deep heartfelt thank you to my wife, Diana who spent many hours by herself during evenings, holidays, and weekends when my schoolwork demanded attention to assignments, projects or this thesis. How many times did she hear about the computer run that just did not seem to work out or the need to track down a research reference! Love is given in many ways.

When most engineers begin to think of retirement, I could only think of taking on a technical challenge that would reignite my enthusiasm for another 30 years in this profession. I have found again an eagerness for the forthcoming challenges as I felt at my first graduation so many years ago; but on the other hand, also only such a short time ago.

"Everything should be made as simple as possible, but not simpler."

Quote attributed to Albert Einstein according to Kevin Harris,
<http://rescomp.stanford.edu/~cheshire/EinsteinQuotes.html>, Stanford University, 1995
accessed 21 Feb 2009

Table of Contents

LIST OF TABLES

LIST OF FIGURES

LIST OF SYMBOLS, NOMENCLATURE AND ABBREVIATIONS

CHAPTER 1	INTRODUCTION	1
1.1	Background	1
1.2	Thesis Objectives	9
1.3	Coker Drum Operations Description	13
CHAPTER 2	LITERATURE REVIEW	17
2.1	Surveys	17
2.1	Papers	20
2.1.1	Analytical Studies	20
2.1.2	Empirical Approaches	24
2.1.3	Fabricaton Approach	30
2.2	Undisclosed Methodology	31
2.3	Unpublished Studies	31
2.4	Conclusions	32
CHAPTER 3	ELASTIC PLASTIC MATERIAL BEHAVIOUR	34
3.1	Stress – Strain Relationships	34
3.2	Plasticity	40
3.3	Isotropic Hardening.....	42
3.4	Kinematic Hardening.....	42
3.5	Temperature Effects	44
3.6	Low Cycle Fatigue	45
CHAPTER 4	MATERIALS TESTING.....	53
4.1	Primary Properties of Interest	53
4.2	Testing Results	53
4.3	Conclusions – Materials Testing	62
CHAPTER 5	CHARACTERIZATION OF THERMO MECHANICAL LOADING ..	
	64
5.1	Loads Imposed During Operational Sequencing	64
5.2	Heat Transfer Modes	70
5.2.1	Calculation of Heat Transfer Coefficients.....	73
5.3	Establishing Heat Transfer Coefficients by Thermal FEA.....	79

CHAPTER 6	ANALYSIS – CLOSED FORM MODELS	88
6.1	Closed Form Models.....	88
6.1.1	Stress and Strain Determination.....	92
6.1.2	Damage Accumulation Determination	99
6.2	Critique of Available Experimental Data	100
6.3	Reevaluation of Selected Experimental Data	103
6.4	Comment on Existing Evaluations.....	105
6.5	Re- evaluation of Existing Industry Data	105
6.5.1	Surface Temperature Change versus Through-Thickness Temperature Change	106
6.5.2	Consideration of Discontinuity Stresses caused by Clad Fabrication....	111
6.5.3	N _i Failure Determination Based on Bounding Approach	113
6.5.4	An Example of Cyclic Life Determination	115
6.5.5	Impact of Pressure Cycling.....	118
6.5.6	Impact of Live weight Cycling	119
6.5.7	Impact of Combined Pressure plus Live weight Cycling.....	119
6.6	Summary.....	120
CHAPTER 7	ANALYSIS – NUMERICAL MODELS	121
7.1	Introduction.....	121
7.2	Temperature Dependant Material Properties	122
7.3	Modeling Strategy.....	125
7.4	Radial Temperature Loading Models	127
7.4.1	Radial Temperature Model – No Defect	129
7.4.2	Radial Temperature Model – Defect Present.....	137
7.5	Longitudinal Temperature Loading Model	144
7.6	Reconciliation of Measured to Calculated Data.....	151
7.7	On Modeling of a Non-axisymmetric Defect	154
7.8	Summary	159
CHAPTER 8	CONCLUSIONS	160
CHAPTER 9	RECOMMENDATIONS FOR FUTURE WORK.....	164
REFERENCES	165
APPENDICES	170
APPENDIX 1	DISCONTINUITY STRESS IN CLAD PLATE	171

List of Tables

Table 1.1	Chemical Compositions for Materials of Construction	2
Table 1.2	Strength Requirements for Materials of Construction	7
Table 1.3	Coke Drum Operating Cycle	15
Table 2.1	Heuristically Determined Internal Film Coefficients.....	22
Table 3.1	Chemical Compositions for Materials of Construction	49
Table 4.1	Physical Properties for Materials of Construction	55
Table 4.2	Comparison of Specified to Measured Monotonic Properties – Room Temperature	61
Table 4.1M	Physical Properties for Materials of Construction– SI Units	63
Table 4.2M	Comparison of Specified to Measured Properties –SI Units	63
Table 5.1	Surface Condensation Conductances	74
Table 5.2	Surface Boiling Conductance by Equation 5.3.....	76
Table 5.3	Loading Characterization for Coke Drum Shell.....	78
Table 5.4	Temperature Ramp Matching to Determine Heat Transfer Coefficients	84
Table 5.4M	Temperature Ramp Matching to Determine Heat Transfer Coefficients – SI Units	87
Table 6.1	Lower Bound Life Determination for Coke Drum Shell	113
Table 6.2	Comparison of Cyclic Life Determinations for Coke Drum Shell ..	117
Table 7.1	Chemical Composition Requirements for Weld Metal.....	122
Table 7.2	Some Material Properties Derived from Testing	123
Table 7.2M	Some Material Properties Derived from Testing – SI Units	124
Table 7.3	Comparison of Cyclic Life Determinations for Coke Drum Shell ...	138
Table 7.4	Comparison of Measured to Calculated OD Surface Behaviour ...	151

Table 7.4M	Comparison of Measured to Calculated OD Surface Behaviour – SI Units	153
Table 7.5	Stress Concentration Factors for Elliptical Hole Models	155
Table 7.6	Stress Concentration Factors for Ellipsoidal Cavity of Varying Ratios	157

List of Figures

Figure 1.1	Photograph of Coke Drums in Process Unit	1
Figure 1.2	Laser Scan Image of Bulged Coke Drum Shell	4
Figure 1.3	Laser Scan Image of Bulged Coke Drum Shell	5
Figure 1.4	Photograph of Cracked Coke Drum Shell – Internal	6
Figure 1.5	Photograph of Cracked Coke Drum Shell – External	6
Figure 1.6	Delayed Coker Unit Process Flow Schematic	15
Figure 1.7	Shot Coke	16
Figure 1.8	Sponge Coke	16
Figure 2.1	Profile Scan of Damaged Coker Drum	26
Figure 2.2	Laser Scan of Drum with Complex Damage Profile.....	27
Figure 2.3	Characterization by Bulge Intensity Factor	28
Figure 2.4	Conventional versus Vertical Plate Construction	30
Figure 3.1	Material Monotonic Stress – Strain Curve	35
Figure 3.2	Material Stress – Strain Curve with Unloading	40
Figure 3.3	Material Stress – Strain Curve with Load Reversal.....	43
Figure 3.4	Fatigue Curve	45
Figure 3.5	Fatigue Data of Wöhler	47
Figure 3.6	Strain versus Cyclic Life	50
Figure 3.7	Cyclic Stress-Strain Curve – Grade 4340	51
Figure 3.8	Comparison of Mechanical to Thermal Strain Cycling	52
Figure 4.1	Monotonic Curves for SA 387 11 Plate - Room & Elevated Temperatures.....	54
Figure 4.2	Comparison of Monotonic to Cyclic Stress Strain Curve for Sampled SA 387 11 [1¼ Cr –½Mo] Plate – Room Temperature	56

Figure 4.3	Comparison of Monotonic to Cyclic Stress Strain Curve for Sampled SA 387 11 [1¼ Cr –½Mo] Plate – Elevated Temperature	57
Figure 4.4	Comparison of Monotonic to Cyclic Stress Strain Curve for Sampled SA 240 TP 410S Clad – Room & Elevated Temperatures.....	58
Figure 4.5	Comparison of Monotonic to Cyclic Stress Strain Curves for Sampled SA 240 TP 410S Clad – Room Temperature.....	59
Figure 4.6	Comparison of Monotonic to Cyclic Stress Strain Curves for Sampled SA 240 TP 410S Clad – Elevated Temperature	60
Figure 5.1	Vessel Shell Temperatures during Operational Cycle	68
Figure 5.2	Schematic Locations of Thermocouples.....	69
Figure 5.3	Thermal FEA Model at Circumferential Weld.....	82
Figure 5.4	Comparison of Calculated Temperatures to Measured	86
Figure 6.1	Vessel Shell Temperatures during Operational Cycle	89
Figure 6.2	Vessel Shell Temperatures during Operational Cycle	90
Figure 6.3	Vessel Shell Principal Strains for an Operational Cycle.....	95
Figure 6.4	Vessel Shell Principal Strains for an Operational Cycle.....	96
Figure 6.5	Strain and Operational Data from Reference.....	103
Figure 6.6	Thermal Strains Occuring in a Thin Plate	107
Figure 6.7	Low Cycle Strain Life for 2¼ Cr – 1 Mo Steel	114
Figure 6.8	Strain Range Frequency Data.....	115
Figure 6.9	Estimated Hoop Strain Range Frequency Data.....	116
Figure 6.10	Number of Drums Reporting First Through Wall Crack.....	117
Figure 7.1	Axisymmetric FEA Model at Circumferential Weld.....	128
Figure 7.2	Stress Profile for Radial Temperature Model.....	129
Figure 7.3	Temperature – Stress Comparison during Accelerated Loading...	131
Figure 7.4	Temperature Differentials – Nominal Loading	133
Figure 7.5	Temperature Differentials – Accelerated Loading.....	136

Figure 7.6	Rounded Indications Chart Acceptance Standard in Welds.....	137
Figure 7.7	Axisymmetric FEA Model with Defect in Circumferential Weld	139
Figure 7.8	Stress Profile for Axisymmetric Model with Defect.....	140
Figure 7.9	Temperature - Stress Comparison with Defect [time = 17,901 sec]....	142
Figure 7.10	Temperature - Stress Profile Comparisons [time = 17,965 sec]	143
Figure 7.11	Long Axisymmetric FEA Model with Defect in Weld	145
Figure 7.12	Stress Profile for Long Axisymmetric FEA Model with Defect...	147
Figure 7.13	Thermal – Displacement – Detailed Stress Profiles at 19,868 sec..	149
Figure 7.14	Thermal – Displacement – Detailed Stress Profiles at 20,468 sec..	150
Figure 7.15	Geometric Model for Experimental Photoelastic Studies of Hanus	155
Figure A - 1	Two Dimensional Stress in Clad Plate.....	172
Figure A - 2	Two Dimensional Stress in Bimetal Plate – X Direction	175
Figure A - 3	Two Dimensional Stress in Bimetal Plate – Z Direction	176

List of Nomenclature, Abbreviations, Symbols

Code	- the ASME Boiler and Pressure Vessel Code [BPV], a document governing the design, fabrication, construction and testing of pressure vessels and given the force of law in many legal jurisdictions, especially in Canada and the United States of America
Discontinuous yielding	- a hesitation or fluctuation of force observed at the onset of plastic deformation, due to localized yielding
Ductility	- ability of a material to deform plastically before fracturing and typically measured by elongation or reduction of cross-sectional area, among others
Elastic limit	- the greatest stress which a material is capable of sustaining without any permanent strain remaining upon complete release of the stress
Elastic modulus	- same as modulus of elasticity
Elastic true strain	- elastic component of the true strain
Engineering strain	- a dimensionless value that is the change in length per unit length of original linear dimension along the loading axis of the specimen, i.e. $e = \Delta L / L_0$
Engineering stress	- the normal stress, expressed in units of applied force, F per unit of original cross-section area, A_0 , i.e. $S = F / A_0$
Fatigue life	- the numbers of cycles of stress or strain of a specified character that a given specimen sustains before failure of a specified nature occurs, such as crack initiation or through section failure
Fatigue ductility	- the ability of a material to deform plastically before fracturing, determined from a constant-strain amplitude, low cycle fatigue test
Fracture ductility	- the true plastic strain at fracture
Fracture strength	- the normal stress at the beginning of fracture, fracture strength is the ratio of force at the beginning of fracture during a tension test to the original cross-sectional area of the specimen
Fracture stress	- the true normal stress on a minimum cross-sectional area at the beginning of fracture

Nomenclature – cont'd

Mechanical properties	- those properties of a material that are associated with elastic and inelastic reaction when force is applied, or that involve the relationship between stress and strain, c.f. physical properties which refer to properties in a general sense
Monotonic loading	- steadily rising portion of the stress-strain curve, with no reversal taking place during the continuously increasing loading path
Modulus of elasticity	- the ratio of stress to corresponding strain below the proportional limit
Nominal stress	- the stress at a point calculated on the net cross section by simple elastic theory without taking into account the effect on the stress produced by geometric discontinuities such as holes, grooves, fillets, etc.
Non-proportional loading	- in deformation theory, a state of loading in which the ratios among the stress components do not remain constant resulting in a more generalized application of theory
Normal stress	- the stress component perpendicular to a plane on which the forces act
Plastic true strain	- the inelastic component of true strain
Poisson's ratio	- the negative of the ratio of transverse strain to the corresponding axial strain resulting from axial stress below the proportional limit of the material
Proportional limit	- the greatest stress which a material is capable of sustaining without any deviation from proportionality of stress to strain
Proportional loading	- in deformation theory, a state of loading in which the ratios among the stress components remain constant resulting in limits of application
Strain	- the per unit change, due to force, in the size or shape of a body referred to its original size or shape. Strain is a non-dimensional quantity, but is frequently expressed in inches per inch, mm per mm or microstrain
Strain hardening	- the increase in strength associated with plastic deformation
Stress	- the intensity at a point in a body of the forces or components of force that act on a given plane through the point, expressed in force per unit area

Nomenclature – cont'd

Stress – strain diagram	- a diagram in which corresponding value of stress and strain are plotted against each other. Values of stress are usually plotted as ordinates and values of strain as abscissas
Secant modulus	- the slope of the secant drawn from the origin to any specified point on the stress – strain curve
Tangent modulus	- the slope of the stress-strain curve at any specified stress or strain
Tensile strength	- the maximum tensile stress which a material is capable of sustaining. Tensile strength is calculated from the maximum force during a tension test carried to rupture and the original cross-sectional area of the specimen
True stress	- the instantaneous normal stress, σ calculated on the basis of the applied force, F divided by the instantaneous cross-sectional area, A i.e., $\sigma = F/A$. If no necking has occurred, $\sigma = S \cdot (1+e)$ where $S \equiv$ engineering stress, $e \equiv$ engineering strain, all defined above
True strain	- the natural logarithm of the ratio of instantaneous gage length, L to the original gage length, L_0 . i.e., $\epsilon = \ln (L / L_0)$ or $\epsilon = \ln (1+e)$
Upper yield strength	- in a uniaxial test, the first stress maximum associated with discontinuous yielding at or near the onset of plastic deformation
Yield point	- term previously used to refer to upper yield strength
Yield point elongation	- the strain separating the stress-strain curve's first point of zero slope from the point of transition from discontinuous yielding to uniform strain hardening. If there is no point at or near the onset of yielding at which the slope reaches zero, the material has 0% yield point elongation
Yield strength	- the engineering stress at which, by convention, it is considered that plastic elongation of the material has commenced. This stress may be specified in terms of (a) a specified deviation from a linear stress – strain relationship, (b) a specified total extension attained, or (c) maximum or minimum engineering stresses measured during discontinuous yielding. In summary, (a) 0.2% offset strain (b) 0.5% extension under load (c) upper or lower yield strength
Young's modulus	- the ratio of tensile or compressive stress to corresponding strain below the proportional limit of the material

Nomenclature – cont'd

References for Nomenclature

ASTM, "E 6 – 06 Standard Methodology Relating to Methods of Mechanical Testing"
ASTM, West Conshohocken PA 2006

ASME, "VIII Division 1 Rules for Construction of Pressure Vessels", 2007 ASME, New York, NY

Rees, D.W.A., "Basic Engineering Plasticity, An Introduction with Engineering and Manufacturing Applications", Butterworth Heinemann, Oxford, UK 2006

Dowling, N.E., "Mechanical Behavior of Materials", 3rd Ed, Pearson Prentice Hall, Upper Saddle River, NJ 2007

Abbreviations

AET	Acoustic emissions testing
API	American Petroleum Institute
ASME	American Society of Mechanical Engineers
bbl	barrel
BIF	bulge intensity factor
C	carbon
Cr	chrome
CRD	collaborative research and development, an award designation from the Natural Sciences and Engineering Research Council of Canada
CS#	Shell course designator
CTE	Coefficient of thermal expansion
DCU	Delayed Cracking Unit
E	Young's modulus
ETAN, ET, E _T	Tangent modulus
FEA	Finite element analysis or alternatively, finite element method [FEM]
HAZ	Heat affected zone
HTC	heat transfer coefficient
ID	inside diameter
kPa	unit of pressure or force intensity in SI units, kilo-Pascals, 10^3 N/m^2
kPag	unit of pressure – gauge reading in SI units, kilo-Pascals, 10^3 N/m^2
Mo	molybdenum
Mn	manganese
MPa	mega Pascals, 10^6 N/m^2
MPC	Materials Property Council

Abbreviations – cont'd

MTR	Material test report as required by the ASME Code providing the results of chemical analyses and mechanical tests made in accordance with
NB	note bene [<i>Latin</i>]
NDE	Non destructive examination
OD	outside diameter
op. cit.	opus citatum: (L.) earlier citation
psi	unit of pressure or force intensity in US customary units, pound-force per square inch of area; ksi \equiv thousands pound-force per square inch area
psig	unit of pressure in US customary units, pound-force per square inch of area – gauge reading; ksig \equiv thousands pound-force per square inch area – gauge reading
PL	proportional limit
sic	it is thus [<i>Latin</i>], used within brackets to indicate that what precedes it is written intentionally or is copied verbatim from the original, even if it appears to be a mistake
S_a	allowable stress per ASME VIII Div 1
SCF	stress concentration factor
SEM	scanning electron microscope
S_m	allowable stress intensity per ASME VIII Div 2
SMTS	Specified minimum tensile strength as given in the ASME Code
SMYS	Specified minimum yield strength as given in the ASME Code
SS	Stainless steel
TC	Thermocouple, thermal conductivity
Temp	Temperature
TS	Tensile strength as measured and listed on a material test report
UYS	upper yield strength
YS	Yield strength as measured or listed on a material test report
YP	Yield point or departure from linear stress-strain behaviour

Symbols - [ROMAN]

A	area of cross section
$^{\circ}\text{C}$	degrees Celsius, indicating magnitude of temperature on Celsius scale
C°	Celsius degrees, indicating difference in temperature on Celsius scale
d, D	diameter
e, e_i, e_{ij}	engineering strain; $i, j = 1, 2, 3$ or x, y, z
e_f	engineering fracture strain
E	modulus of elasticity in tension or compression, weld joint efficiency
F	force
$^{\circ}\text{F}$	degrees Fahrenheit, indicating magnitude of temperature on Fahrenheit scale
F°	Fahrenheit degrees, indicating difference in temperature on Fahrenheit scale
G	modulus of elasticity in shear
H	height
L	length
M	bending moment
N	cycles
N_f	cycles to failure
$2 \cdot N_f$	stress reversals to failure
p, P	pressure, traction load
r, R	radius
RT	radiographic test
s, S	nominal engineering stress
S_H, S_L	nominal hoop stress, nominal longitudinal stress

Symbols [ROMAN] – cont'd

S_f	engineering fracture stress
Si	silicon
S_t	nominal tensile engineering stress
S_u	tensile strength
S_y	yield strength
T	temperature
ΔT	temperature difference
t	thickness
t	time
W	work or energy

Symbols [GREEK] — cont'd

α	coefficient of thermal expansion
δ	deviation
Δ	increment or change
$\Delta\epsilon$	strain range
$\Delta\sigma$	stress range
$\epsilon, \epsilon_i, \epsilon_{ij}$	strain, strain components; $i, j = 1, 2, 3$ or x, y, z
ϵ^e	elastic strain
ϵ_{eff}	effective strain
ϵ_f	true fracture strain
ϵ^p	plastic strain
$\epsilon_{\text{mech}}, \epsilon_M$	mechanical strain
$\epsilon_{\text{thermal}}, \epsilon_{TH}$	thermal strain
ϵ_T	total strain
γ, γ_{ij}	true shear strain, shear strain components, specific density
$\sigma, \sigma_i, \sigma_{ij}$	normal stress, normal stress components; $i, j = 1, 2, 3$ or x, y, z
σ_f	true fracture stress
σ_t	tensile true stress
τ, τ_i, τ_{ij}	shear stress, shear stress components; $i, j = 1, 2, 3$ or x, y, z
μ, ν	Poisson's ratio
σ_{yield}	normal stress yield point
$\mu\epsilon, \text{ue}$	microstrain, 1×10^{-6} strain or 1×10^{-6} inch per inch, 1×10^{-6} m per m

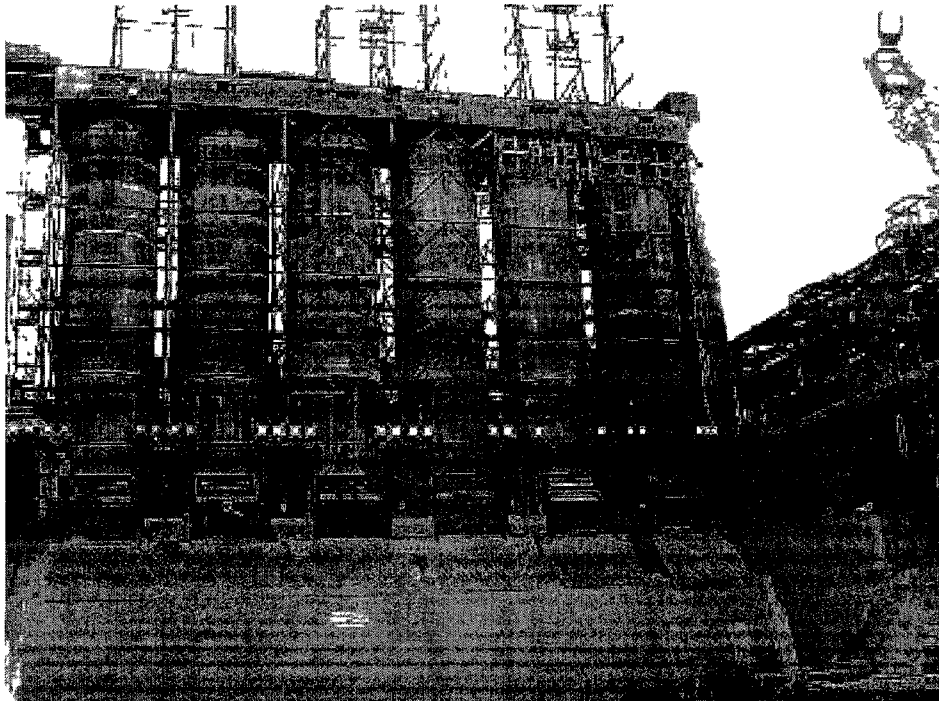
CHAPTER 1 INTRODUCTION

1.1 Background

Delayed coking is a processing technology used in oil refining and oil sands upgrading facilities to convert petroleum residuum into lighter liquid and gas product streams. The remnant material is a solid concentrated carbon material referred to as petroleum coke. The processing unit is commonly referred to as a Delayed Coker Unit [DCU]. [1]

Coke drums are large diameter, thin walled pressure vessels used in the Delayed Coker Unit where the coking separation step takes place. These vessels are manufactured with dimensions of 30 feet [9000 mm] diameter and 90 feet [28000 mm] of straight side height. The vessels operate at a pressure of 35 to 55 psig [240 to 380 kPag] and 900 °F [482 °C]. The drums are installed as paired units. Figure 1.1 shows three drum pairs located in a typical installation.

Figure 1.1 Photograph of Coke Drums in Process Unit [2]



The materials of construction for coke drums are low alloy carbon steel base plate with a high alloy internal cladding layer. The base plate materials vary depending on specific operating conditions and user discretion and include carbon steel and C – ½ Mo, 1¼ Cr – ½ Mo, and 2¼ Cr – 1Mo low alloy steels. Table 1.1 lists the range of materials used in the fabrication of these vessels with their chemical compositions. Clad plate materials are grades of 12 Cr or 13 Cr SS, either 405 or 410S stainless steel. The vessels are constructed using the rules of ASME VIII Division 1 Rules for Construction of Pressure Vessels [3] in Canada and the United States of America. There are similar Codes in other jurisdictions. The application of this specific Code to the design of this equipment provides a design-by-rules approach resulting in a vessel shell thickness based primarily on pressure considerations. Consideration of other loadings is typically not fully accounted for by practitioners of this Code, although the Code does require consideration of all influencing loads for final design.

Table 1.1 Chemical Compositions for Materials of Construction in [%] [4]

Material	C	Mn	Cr	Mo	P	S	Si	Ni
SA 240 TP 405	.08	1.0	13	-	.04	.03	1.00	.60
SA 240 TP 410S	.08	1.0	12½	-	.04	.03	1.00	.60
SA 516 70	.28	1.0	-	-	.035	.035	.45	-
SA 204 C	.26	.98	-	½	.035	.035	.29	
SA 387 12	.1	.5	1	½	.035	.035	.3	
SA 387 11	.1	.5	1¼	½	.035	.035	.6	
SA 387 22	.1	.5	2¼	1	.035	.035	.50	
SA 387 21	.1	.5	3	1	.035	.035	.50	

Notes to Table 1.1

1. Nominal compositions are given; see reference for composition limits.
2. Other trace and alloying elements may be present as provided for by Code

Since operating loads are not usually fully defined by User organizations, actual service loads are not accounted for and would also be beyond the design capability of the simplified Division 1 Code approach.

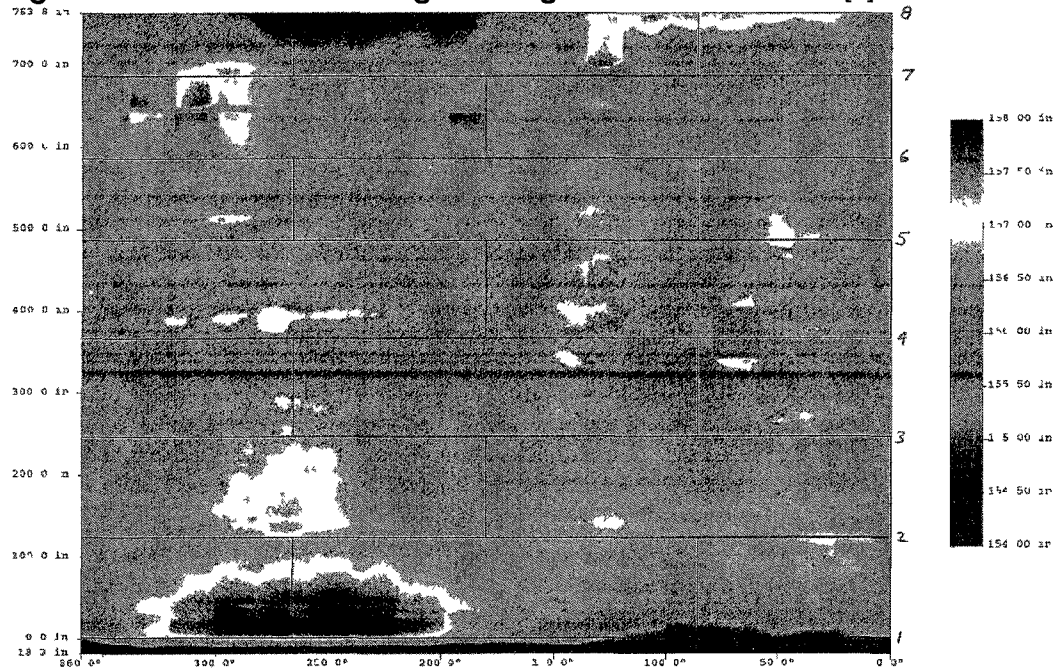
These vessels can exhibit early and repeated failure. A DCU unit processes upwards of 30,000 barrels of oil per day and it is becoming routine to process 100,000 barrels per day; therefore, equipment failure can cause economic losses in the hundreds of thousands to millions of dollars in lost revenue and repair costs.

Eight failure modes have been cited in the literature by means of surveys conducted over a 50 year time frame starting in 1958 [5] [6] [7].

- deformation of shell
- growth of shell
- irregular local warping of shell
- cracking of skirt attachment weld
- distortion of bottom manhole-neck flange
- weld cracking between bottom cone and manhole neck
- nozzle attachment cracking
- dishing of bottom cover

The most common and serious failure mode cited in the 1958 survey indicated deformation and growth of the shell. This bulging is typically accompanied by cracking in the circumferential and longitudinal weld seams required to fabricate the relatively long length and large diameter shell of the vessel, although cracking is also reported in non-bulged areas. Figure 1.2 is a projected image from a laser scan of the drum shell cylindrical surface showing bulged [red coloured] and indented [blue coloured] areas. The bottom cone and top head are not included as these components are not susceptible to failure.

Figure 1.2 Laser Scan Image of Bulged Coke Drum Shell [8]



The continuous horizontal and discontinuous vertical lines in the illustration represent shell weld seams. The horizontal seams are numbered from 1 to 8 along the right hand side of the image. Bulging is thought to occur mainly in a circumferential direction and is exhibited by the extended red coloured patch in the lower left of the image along weld seam 1 between azimuth angle 200° and 320°.

Figure 1.3 is an isometric projection image from another coke drum shell indicating that bulging can also occur in a predominately longitudinal direction.

Figure 1.3 Laser Scan Image of Bulged Coke Drum Shell [9]

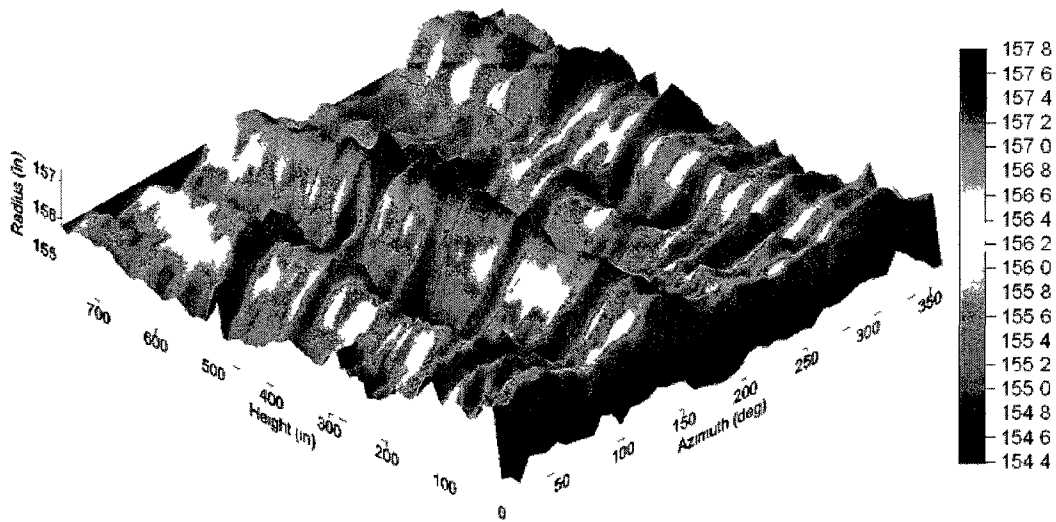


Figure 1.4 is a photograph of a through wall crack from the inside of a coker drum vessel. Figure 1.5 is a photograph of a through wall crack from the outside of a coker drum vessel. Through wall cracking will result in shutdown of the vessel and may result in fire. These fires have been reported as non-serious. By the 1996 survey, skirt cracking was reported as being the more common problem, followed by shell bulging and cracking. Equipment failure is seen to be a reliability issue and the consequential economic penalties are not held to be a concern for jurisdiction authorities since the overall safety performance has been considered acceptable.

Figure 1.4 Photograph of Cracked Coke Drum Shell – Internal [8]

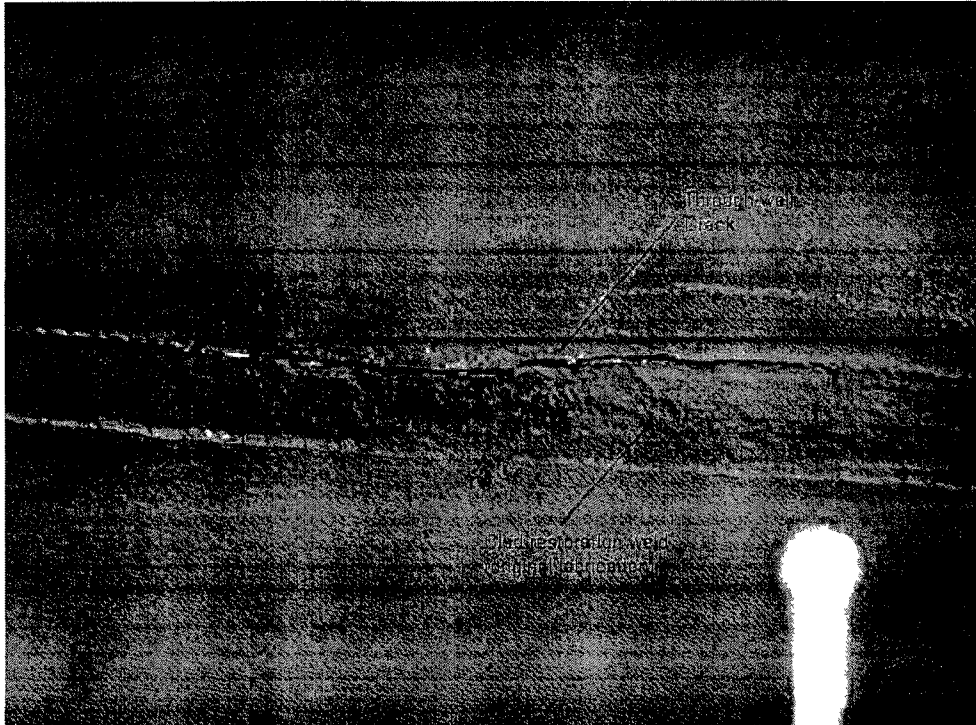
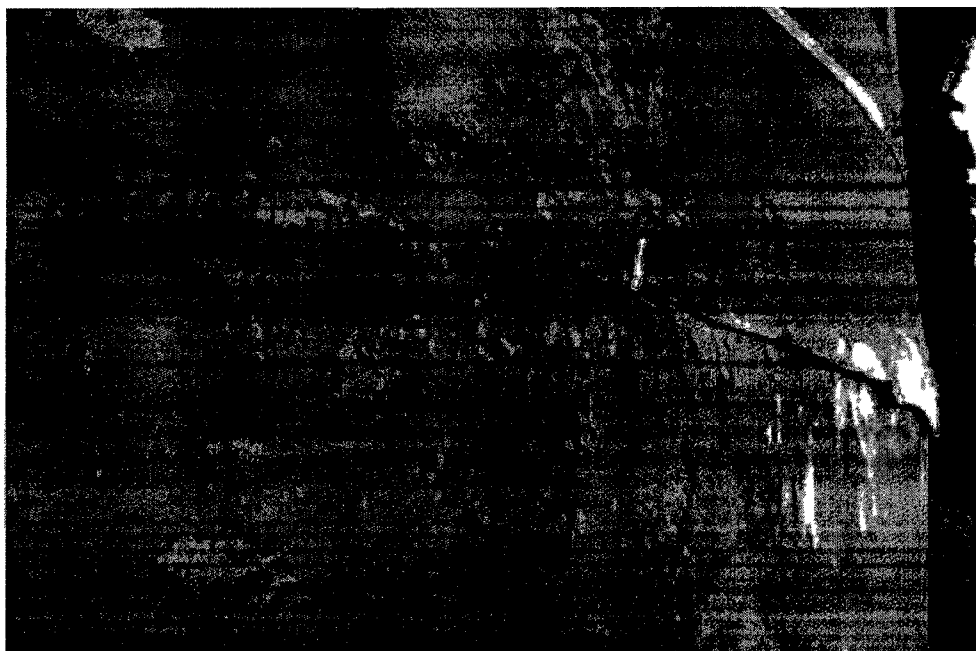


Figure 1.5 Photograph of Cracked Coke Drum Shell – External [8]



In an effort by the industry to address these failures, base material selection has progressed from plain carbon steel and C – ½ Mo compositions to higher alloy-containing materials of 1 Cr, 1¼ Cr, 2¼ Cr and 3 Cr due to a perceived opinion that these materials have decreased susceptibility to cracking. However, the recent survey data does not substantiate this [7]. Table 1.2 provides a listing of mechanical properties for base and clad materials used historically and currently. The SMYS and SMTS strength values refer to the minimum specified yield and tensile strength values required by Code [10] upon which the design allowable stresses are based. These values may differ from the actual yield strength, YS and tensile strength, TS values for a supplied material.

Table 1.2 Strength Requirements for Materials of Construction [10]

Material	SMYS				SMTS			
	[ksi]		[MPa]		[ksi]		[MPa]	
	100 °F	900 °F	37.8 °C	482 °C	100 °F	900 °F	37.8 °C	482 °C
SA 240 405	25.0	16.9	172.4	116.5	60.0	44.0	413.7	303.4
SA 240 410S	30.0	20.3	206.8	140.0	60.0	44.0	413.7	303.4
SA 516 70	38.0	24.0	262.0	165.5	70.0	52.3	482.6	360.6
SA 204 C	43.0	30.0	296.5	206.8	75.0	69.7	517.1	480.6
SA 387 12	33.0	30.0	227.5	206.8	55.0	51.4	379.2	354.4
SA 387 11	35.0	23.8	241.3	164.1	60.0	55.8	413.7	384.7
SA 387 22	30.0	25.6	206.8	176.5	60.0	58.2	413.7	401.3
SA 387 21	30.0	25.6	206.8	176.5	60.0	58.2	413.7	401.3

The design life of these vessels is nominally twenty five years, although experience proves that substantially longer service life is realized even when vessels have experienced the failures cited above [8]. Regular maintenance turnarounds are used to make planned repairs. Frequently, unplanned shutdown repairs are necessary to return a damaged vessel to service. A recent industry review of the 1996 API survey indicated that 11 cracks per drum may reasonably be expected during a 20 year period, of which only 30% will be repaired during a planned turnaround [11]. The direct costs of repair are quoted as \$3 million per drum with direct production losses of \$50 million to \$100 million per drum pair (NB - the drums operate in pairs).

1.2 Thesis Objectives

The overall objective of this thesis is **to identify the leading failure mechanism causing shell cracking**. An understanding of the mechanism will help identify avoidance and remediation opportunities in the specification, design, fabrication, operation, and inspection of coker drum vessels. Prediction of remaining life will be of significant benefit in the maintenance of this equipment.

Industry survey cites two primary failure modes occurring in delayed coker unit drums, namely bulging and cracking. Bulging is viewed by industry as a precursor to shell cracking. Cracking occurs in two general locations, straight side shell cracking at circumferential weld seams and at the skirt to shell weld. Both forms of failure have been attributed to low cycle fatigue cracking but the complete mechanism has not been satisfactorily explained. Some of these explanations have included “fast quench rate” and “coke crushing”.

Account will be taken of published material properties and the use of measured material properties.

Creep is not considered in this paper. Coker drums operate at the threshold of the creep regime and creep failure has not been identified in the various studies made to date. Creep effects can be considered above 800 °F [427 °C] for carbon steels and 900 °F [482 °C] for the Cr-Mo steels referenced in this thesis. While 900 °F [482 °C] is used as a design temperature, actual operation is up to 850 °F [454 °C] for the Cr-Mo steels and less than 800 °F [427 °C] for carbon steels. The industry practice is to use a higher design temperature to provide for an additional design margin.

In detail, our research objectives include:

1. Retrieval of the mechanical properties of interest for the materials of construction:

The current industry practice uses a rules-based design methodology to determine a thickness for the coke drum using an allowable stress value for the material of construction and the Code approved formula relating thickness to pressure for the component under consideration. For a cylindrical shell section, the circumferential stress is of interest, and the Code formula is [3]

$$t = \frac{P \cdot R}{S \cdot E - 0.6 \cdot P} \quad [1.1]$$

where, using consistent units:

t \equiv the required thickness,

P \equiv the design pressure of the component,

R \equiv the radius of the cylindrical section,

S \equiv the allowable stress as set out in the Code for the design temperature,

E \equiv weld joint efficiency for the component, dimensionless

This formula is to be used where the combined general membrane stress in the component is restricted to the stress limit defined by S , the allowable stress.

Other loads, if they cause general membrane stress to exceed the allowable stress limit must be considered and the component thickness then increased to account for additional loads. Some loads may be cyclic in which other appropriate failure criteria, such as the fatigue limit must be considered.

Therefore, the mechanical properties of interest include, at room and elevated temperature [i.e. 800 °F or 427 °C],

- yield strength
 - tensile strength
 - cyclic yield strength
 - fatigue strength
 - modulus of elasticity
2. Perform experimental tests to confirm the key mechanical properties listed in item 1.
 3. Identify loads acting during coke drum operation

The coker drum is subjected to other loads during operation which must be accounted for in the design. These include, in part

- hydrostatic load due to added coke residual weight
 - hydrostatic load due to water
 - mechanical loads due to differences in temperature between adjacent portions of the shell structure
 - mechanical loads due to differences in thermal expansion between clad and base material
4. Assessment of low cycle fatigue using a bounding limit approach in consideration of the lack of comprehensive and accurate strain data in the literature and private sources.

5. Conduct numerical modeling to determine plausible

- i. temperature history and distributions, and
- ii. resultant stress and strain distributions

Closed form expressions are not available or not readily developed for some aspects of loading, such as

- stress profile through the base material due to differential thermal expansion
- stress profile in radial direction through clad and base material during transient heating
- stress profile in axial direction during transient heating
- accounting for temperature dependency of material properties
- accounting for plasticity

Therefore, a finite element numerical analysis approach is necessary.

6. Evaluate which combination of loads leads to failure

The loads act in combination and therefore no single load may adequately account for the damage experienced in the operation of coker drums. Viable load combinations may need to be considered to account for the damage.

Assessment of low cycle fatigue cracking will be made using industry methodology cited in the literature.

7. Industry codes make provision for an acceptable level of defects in vessel fabrication. This means that vessel shell welds will contain defects. Analysis will be made as to the impact this practical provision has on the expected life of a coker drum.

1.3 Coker Drum Operations Description

The delayed coking process consists of heating reduced bitumen feed to a high temperature and injection into a large, cylindrical vessel commonly referred to in industry terminology as a coke drum. Lighter end hydrocarbons disengage as a vapour from the liquid stream and are conveyed to downstream processing equipment. The remaining solid portion of the high temperature reduced bitumen stream remains in the coke drum and will accumulate to a target level at which time the feed stream is diverted to a second drum. The filled drum is then emptied of the coke inventory, in an operation called decoking and then prepared for the next cycle of operation. When the second drum of the two drum set is filled, the reduced bitumen feed is diverted back to the first drum [12]. See Figure 1.6 for the process flow schematic.

Coker drums thus operate in a batch-continuous and paired operation. Typically three or 4 coke drum pairs will be located in a unit to process up to 100,000 bbl per day of reduced bitumen.

The operating cycle is summarized in Table 1.3. We briefly describe the operational sequencing of a coke drum cycle.

The cycle begins with steam testing to pressurize the drum to ensure it is leak tight for operation. The drum is coincidentally heated during this step as the steam is at saturated or even superheat temperature conditions. The next step, called vapour heating, uses a slipstream of hydrocarbon vapour, drawn from the drum currently in the coke filling sequence, to inject into the standby drum. As seen in Table 1.3, the purpose is to preheat the standby drum to receive the hot bitumen oil feed. During fill, exiting vapours are directed to a fractionator vessel. When the bitumen feed level reaches the target fill level, a steam quench sequencing step is made during which residual hydrocarbon vapours are stripped from the residual coke mass and directed also to the fractionator vessel.

A second and, more important function is for the steam to create flow channels by keeping the hot liquid at the top of the coke bed from flowing down the channels that were formed during coking. Once these vapours are recovered and channels established, water is slowly introduced to begin the cool down step. Initially the water converts to steam and these vapours are directed to a separate relieving system. As the cool down progresses, the water quench flow rate is increased until the coke drum becomes filled with water to the target level. The coke residual mass is now sufficiently cooled to allow drainage of the water portion to a separate closed recovery system. At this time, the vessel is depressured to atmospheric pressure, and a coke removal procedure is performed which completely empties the vessel of the cooled, coke mass residual. Coke removal is accomplished using high pressure water jet cutting and gravity dumping. Figure 1.7 is a photograph of “shot” coke as recovered from a coke drum [13]. There are three major forms to the coke mass residual, the preferential form being “sponge” coke, Figure 1.8 while the form having a shot-like appearance is not favoured. The shot form by experience, is more prone to upset drum operations apparently due to its loose agglomerate structure which impacts drum operations such as quenching and residual solids dumping. The third form is needle coke and is a premium commodity used in the manufacture of graphite anodes. It is not found in oil sands delayed coker units as the feedstock characteristics do not favour formation of this type.

Table 1.3 Coke Drum Operating Cycle [8]

Operating Step	Temp [°F]	Pressure [psig]	Temp [°C]	Pressure [kPa]	Duration [hrs]
Steam Test	220	35	104	241	< 3
Vapor Heat	600	35	316	241	3
Oil Fill – Coking	900	35	482	241	11 – 15
Steam Quench	350	35	177	241	< 1
Water Quench	200	35	93	241	3
Unhead	100	0	38	0	< 1
Decoke	100	0	38	0	1 – 3
Total Time	24 – 28				

Notes to Table 1.3

1. Indicated temperatures are stream temperatures. Pressures are vessel internal pressures.

Figure 1.6 Delayed Coker Unit Process Flow Schematic [8]

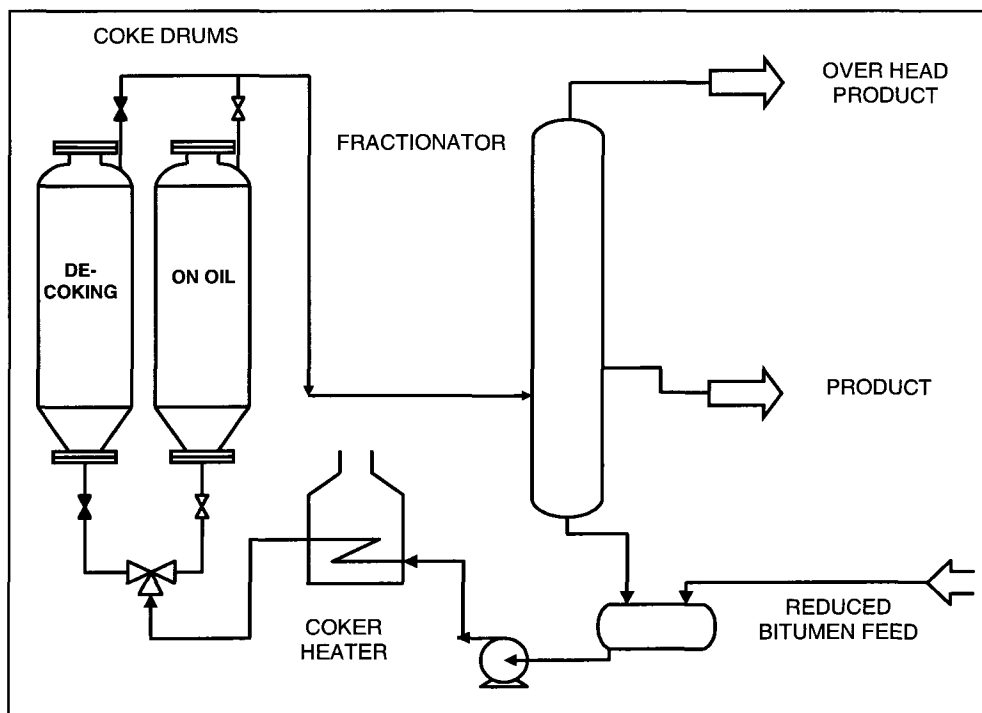


Figure 1.7 Shot Coke [13]

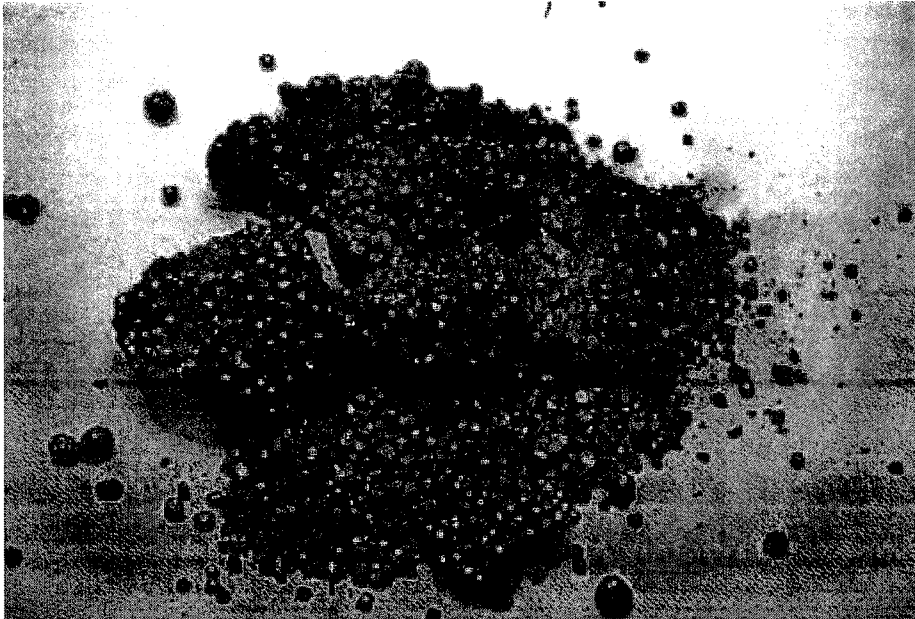
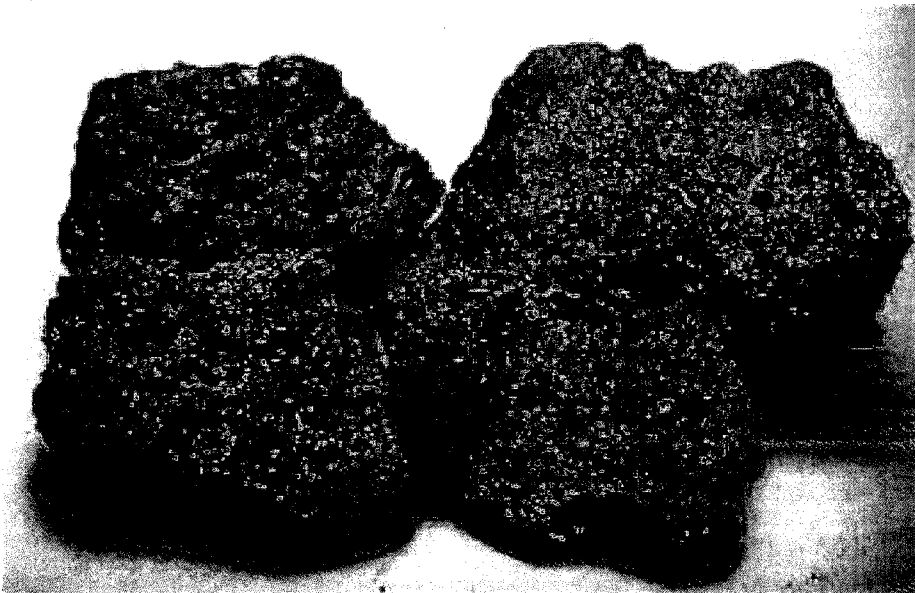


Figure 1.8 Sponge Coke [13]



CHAPTER 2 LITERATURE REVIEW

Prior work is reviewed here. A number of industry survey's are available as well as a few published reports examining the specific failure mechanisms, their characterization and potential solutions.

2.1 Surveys

The importance of this equipment for the industry is demonstrated by the ongoing surveys that have been undertaken since 1958 by the American Petroleum Institute [API].

The first survey covered units constructed from 1938 to time of publication in 1958 comprising some 16 units [5]. The survey is noteworthy in that it:

- provides a qualitative categorization of failures
- quantifies the amount of shell radial bulging
- quantifies the temperature gradient during water quench
- presents an operational criterion related to the water quench rate

A 1980 survey provides an update from a 1968 survey and new findings focusing on drum cracking [6]. Major findings from the 1968 survey include:

- C – Mo and plain carbon steel drums embrittle
- carbon steel drums display more bulging than C – Mo drums
- through wall cracks are circumferential
- vessels with thinner walls crack earlier

Additional observations and conclusions from the 1980 survey include:

- a shift in preference of materials of construction from carbon steel to C – Mo to Cr – Mo compositions, primarily 1 Cr or 1¼ Cr
- the drum shell bulging is characterized as balloon like with minimum radius at the circumferential welds
- first cracking is asserted to occur about 7 years after startup regardless of material [3,500 cycles]
- evidence suggesting that shell bulges fluctuate in radial deflection, from outward to inward, i.e. bulging is dynamic and shell radius may regain original dimension and even indent
- bulges extend approximately 1 inch to 7 inches in radius, both inward and outward [NB - no reporting is given in terms of strain]

The 1996 survey of 145 drums from API provides a more comprehensive review covering design, operation and deterioration. A number of findings appear to contradict prior survey findings [7]. Contradictory findings are marked with a "*" symbol.

- fires were reported for 12% of the drums surveyed, although there was no consequential damage to adjacent equipment
- Cr – Mo alloys continue to be used increasingly
- there is no correlation between material selection and drum life*
- drum cracking is seen to be related to quench rates
- incidents of shell bulging and cracking occur equally
- 80% of units experience bulging, 90% of bulged units experience cracking
- 80% of units experience cracking in non-bulged areas with accumulated cyclic life ranging from 1,980 to 6,100 cycles*
- first cracking occurred in 1,200 cycles minimum for C – ½ Mo vessels and 3,600 cycles minimum for carbon steel vessels, with Cr – Mo at 2,000 cycles
- 97% of respondents indicate circumferential cracking primarily but 52% responded that circumferential and longitudinal cracking occurred*
- most cracking and bulging occur in shell courses 3, 4 and 5*
- the oil fill cycle varies from 10 to 24 hours
- bulges average longer circumferentially than longitudinally but both are present*
- bulging deformation is between ¼" to 6" on radius with average 2" [no strain data given]
- ID initiated cracking occurred as often as OD initiated cracking

2.1 Papers

2.1.1 Analytical Studies

Ramos et al. [14] carried out a comprehensive mechanical integrity evaluation by examining the transient heat transfer profile, performing non-linear stress analysis and conducting low cycle fatigue testing of base and weld metal of 1 Cr and 1¼ Cr low alloy steels. The primary focus of their efforts was the skirt to shell junction. A heat transfer coefficient [HTC] of 200 Btu / hr-ft²-°F [1,134 W/ m²- °C] was used as a boundary condition for a finite element analysis of the skirt to shell junction. A maximum strain of 0.0663 [66,300 µε] was listed [assumed as total strain]. However, additional data in the paper indicates this value was in error and an equivalent strain of 0.015748 [15,748 µε] was given for specific node locations in the skirt. The strain was assumed as a total strain value since there was no indications that strain readings were reset at higher temperatures to remove the thermal strain portion of the measurement.

In an additional work, Ramos et al. [15] carried out an assessment of a 1 Cr drum. A dense grid of thermocouples was installed in order to determine the circumferential and longitudinal temperature gradients covering shell courses 3, 4 and 5. The temperature data revealed random and severe temperature gradients during water quenching. Cool spots of 400 °F [204 °C] occurred randomly. Strain measurements varied from 400 ue to 3,400 ue [micro-strain]. The largest strains were found to occur during the initial stages of quenching although quench rates were always lowest during quench start. The finite element modeling consisted of a shell patch of approximately 8½ feet x 4½ feet [2590 mm x 1222 mm] comprised of 2,640 8-node solid elements. Base metal, weld and cladding were modeled. Axial and circumferential temperature loading was applied to the model by manipulating the heat transfer coefficient to match the measured temperature data. The strain simulation was asserted to match measurement within 15%. It is not clear whether total or mechanical strains were used as the basis of evaluation.

Penso et al. [16] explored crack initiation and propagation mechanisms. Crack initiation was attributed to

- grain growth in the heat affected zone
- weld toe geometry
- strength mismatch between weld, clad and base metal
- thermal shock stresses

The work focused on shell circumferential welds and included extensive metallurgical examinations of samples obtained from 3 damaged coker units and 1 sample from new fabrication. Four types and sites for crack initiation and propagation were identified

- deep cracks in the clad HAZ
- clad shallow cracks
- interbead cracks in the high nickel alloy weld deposit
- inclusion [Mn, Si] cracks in the HAZ base metal

The most damaging cracks were the HAZ cracks because they grew deeper and were described as being perpendicular to the higher stresses. Guidelines were given for weld procedures and materials selection, of varying practicality.

A study by Kirkpatrick et al. [17] further examined the nature of thermal loading and calculated heat transfer coefficients for a coke drum based solely on external thermocouple measurements. A heuristic approach was used to match the calculated temperature profile against measured temperature data. Table 2.1 summarizes the findings of the study.

Table 2.1 Heuristically Determined Internal Film Coefficients per [17]

Operating Step	Time [hr]	Load Form	Internal Temp		Internal HTC	
			[°F]	°C	[Btu/ft ² -hr- °F]	[W / m ² - °C]
Steam Test	0	constant	150	65.6	-	
Vapor Heat	½	step	584	306.7	2.2	12.3
Oil in	9½	step	810	432.2	43.2	245.0
Quench	24	ramp	775	412.8	43.2	245.0
Quench	30	step	150	65.6	4.32	24.5

Boswell et al. [18] state that hot spots, a consequence of non-uniform cooling during quench, are a damage mechanism that is unpredictable and impossible to design for. Bulging is attributed to the relative strength of circumferential weld seam to base plate metal causing a “mechanical stress ratchet mechanism”. This description was not defined further in the paper. The specific equipment reviewed by Boswell displayed a radial deformation of 10% at the top of the 1st course [bottom course] extending for 100% of the circumference. Because of the extent of damage, it would be likely better to describe the deformation as a corrugation. Also, the deformation was not centred on the weld seam but migrated towards mid-level of the 2nd course over 50% of the circumference. Cyclic life evaluation using ASME VIII Div 2 methodologies was used to determine a predicted fatigue life of 4,390 cycles compared to actual usage of 5,500 cycles.

McGowin and White [19] describe in detail a failure occurring in a DCU coke drum with about 10 years of service. An ID surface horizontal crack of 14'-2³/₄" [4338 mm] length occurred with through thickness failure extending some 6'-6" [1981 mm]. The crack appears to have been located in a circumferential bulged zone some 24" [609.6 mm] above a circumferential weld. Secondary cracks on the ID surface had a depth of 0.10" [2.54 mm]. Ultrasonic inspection indicated subsurface defects of 3/32" [2.38 mm] depth or less at the ID surface. Scanning electron microscope [SEM] metallographic examination revealed a mixed ductile-cleaved failure surface. Fatigue striations were noted to be 2 mm in depth, coinciding with the thickness of the clad layer with cleavage failure extending through the base material thickness.

2.1.2 Empirical Approaches

Church Probabilistic Life Assessment

A probabilistic life assessment approach is described by Church et al. [20]. The approach is motivated by a risk based operating philosophy increasingly used by the hydrocarbon processing industry [21] to manage safety and costs. An advantage cited by the author is being able to reconcile variability of input data such as material properties and cyclic strains which are related to operational loads. Stress analysis is based on strain gauge readings that are modified using inferred temperature differences between inner and outer surfaces.

The general methodology consists of

- measuring strain data consisting of axial and hoop strain measurements located at unspecified locations on the drum OD
- measuring temperature data to provide temperature compensation for strain gauge readings in order to establish mechanical strains rather than free thermal strains
- determination of strain distribution i.e. histogram showing the number of occurrences for various strain levels
- determination of stress from strain data
- determination of crack initiation using established industry practice, in this instance, using British standard BS 5500 Annex C [22]
- using Paris crack growth model to determine time for crack propagation
- using Monte Carlo simulation to condition the prediction of crack initiation

Clark Combined Approach

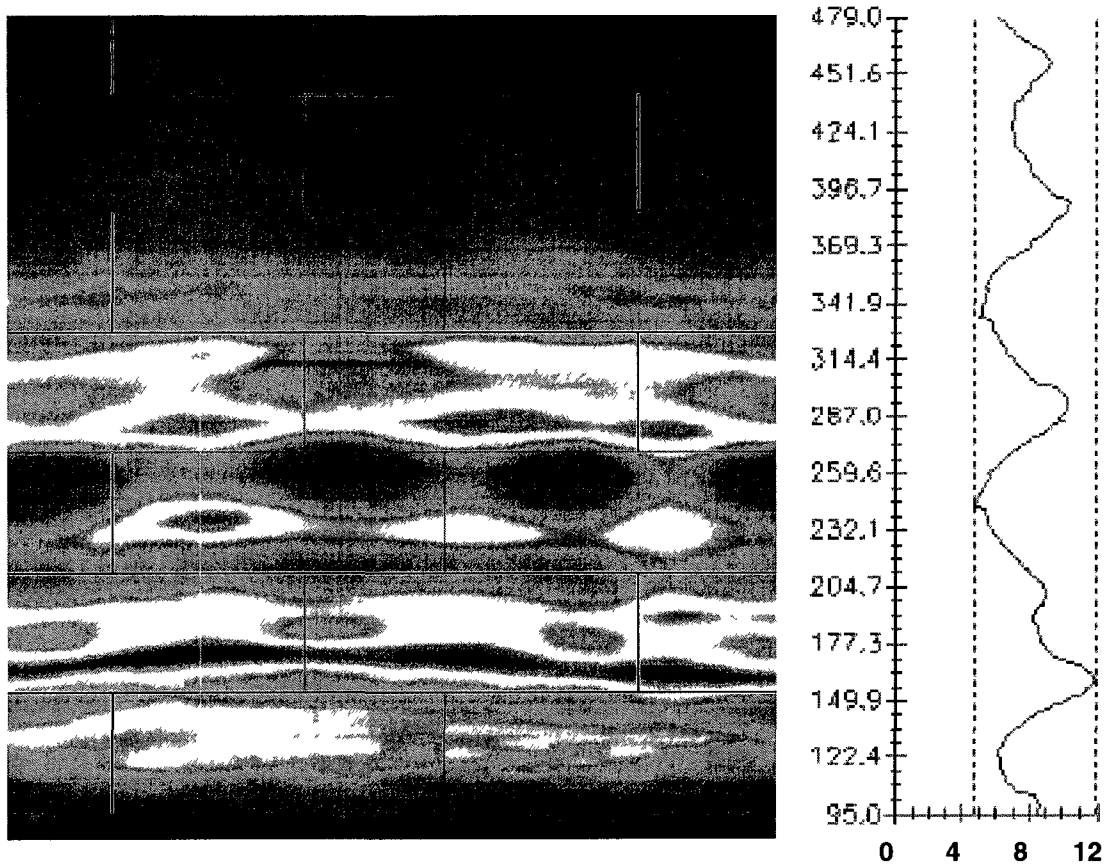
A combined approach advocated by Clark et al. [23] uses a number of explicit technologies to provide a more deterministic tool whereby crack locations are identified, before failure, using non-destructive techniques. Laser profiling, illustrated in Figure 2.1 is used in conjunction with acoustic emission testing to locate and repair shallow cracks prior to failure. Laser profiling identifies bulged and dented portions of the three dimensional coke drum vessel and presents the data as a two dimensional surface mapping. This allows effective identification of candidate trouble areas, these presumably being associated with the bulged areas.

The general procedure is to

- perform the laser profile mapping
- install strain gauges at candidate locations, typically at the bulged locations
- determine stresses and evaluate, presumably using established industry practice
- confirm the evaluation with acoustic emissions testing to establish the presence of a crack like defect
- make a repair or replacement decision

Unfortunately, the example provided in the paper to illustrate the method was applied to a portion of a drum that had cracking identified by closed circuit video camera and was a location identified as susceptible to failure due to prior existing distortions in the cladding liner. The example, therefore, was not a clear demonstration of the method.

Figure 2.1 Profile Scan of Damaged Coker Drum

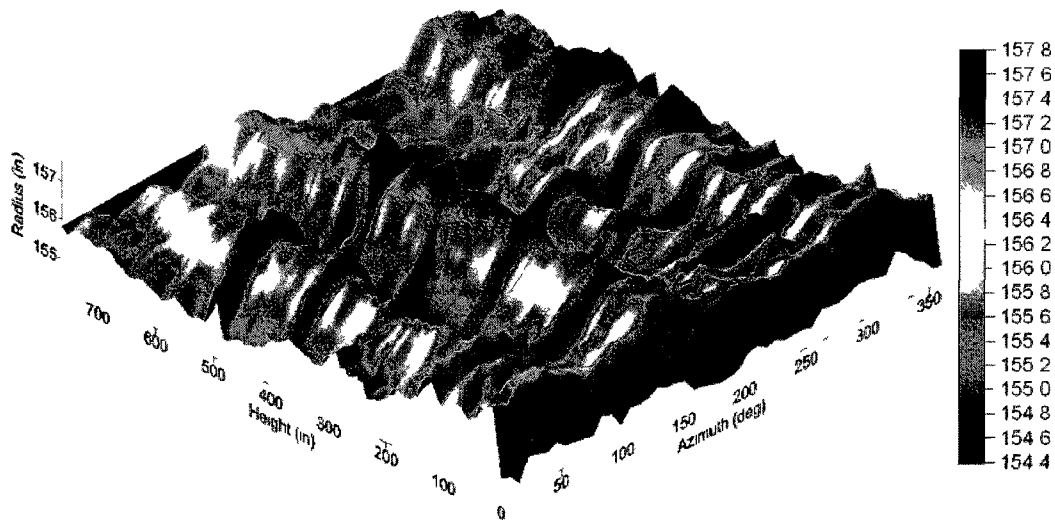


Samman – DuPlessis Bulge Intensity Factor

A failure criterion is presented by Samman and DuPlessis [9] called the Bulging Intensity Factor [BIF] which uses a pattern recognition comparison approach to rank cracking failure susceptibility. The authors assert that radial growth is the more likely damage mode to cause cracks, leaks, fires, operations delays and potentially catastrophic accidents. Bulging is held by the authors as accelerating the formation and propagation of cracks. The motivation in determining the factor is to provide a quantitative assessment of the laser profiling results which may not lend themselves to visual assessment of bulge severity. Analysis provides a non-dimensional severity parameter to be used for integrity management decisions. A single parameter is calculated and presented as the BIF value.

Figure 2.2 illustrates a laser profile where visual evaluation is problematic since the amount of bulging damage is extensive thereby requiring a large number of strain gauges and producing a commensurate amount of data to be further evaluated. Figure 2.3 illustrates the resolution provided by the BIF approach. A BIF value greater than 1.5 is considered severe.

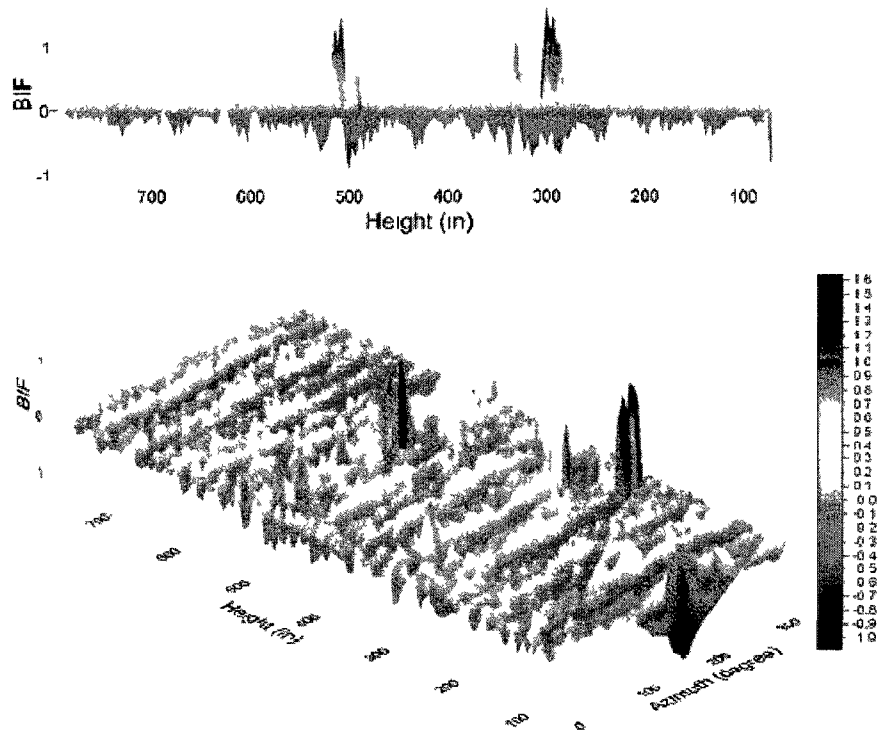
Figure 2.2 Laser Scan of Drum with Complex Damage Profile [9]



Notes to Figure 2.2

1. Nominal radius of drum = 156 inches
2. Circumferential and longitudinal weld seams are shown by darkened lines
3. 3 full drum-height sine waves, 4th half drum-height sine wave exhibited
4. Maximum bulging occurs in shell courses 4 and 5

Figure 2.3 Characterization by Bulge Intensity Factor [9]



The technical details underlying the BIF approach are found in waveform pattern recognition and rely on heuristic methods to improve correlations between the amount of bulging and eventual crack failure. The authors of this approach have disclosed that this predictive methodology using biaxial bulge frequency, magnitude and curvature processing can allow correlation to crack failure history for a specific drum. The algorithm has not been disclosed.

One can reasonably infer that the factors being considered to calculate the BIF may include:

- the radial distortion from original radius, being a general indicator of strain
- the distance over the shell surface in which the change in radius occurs, a steeper transition being more severe than a gradual transition [curvature processing mentioned above]
- whether the transition occurs longitudinally or circumferentially, the longitudinal bending stiffness of a cylinder being greater than the circumferential stiffness
- the location relative to weld seams, with the portions of bulges transitioning at welds ranking higher than the transition portions of bulges occurring at locations away from the seam

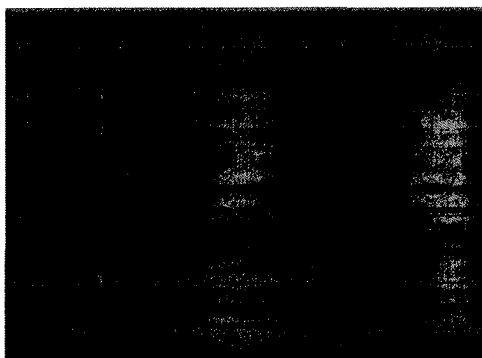
The literature indicates that waveform recognition technology was identified about 1965 in a patent granted to R.E. Milford at the General Electric Company [CA 701165] [24]. Practical application of waveform recognition has been applied in determining the probability of death of cardiac patients [CA 1323431] [25]. In the specific patent, sixteen factors are ranked to calculate a probability of death. The ranking is used to assess the level of appropriate care to be administered to a patient.

2.1.3 Fabrication Approach

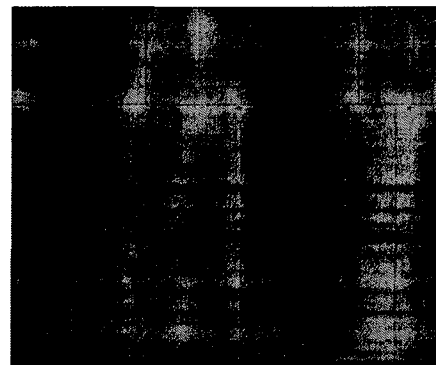
An alternative fabrication scheme is used to repair damaged drums and eliminate future damage. This alternative design uses vertically oriented shell plates rather than circumferential plate construction to eliminate “inherently susceptible” circumferential weld seams [11]. The essential premise is that shell integrity failures occur at the weld seams therefore, minimizing weld seams affords the best probability of avoiding failures. Figure 2.4 provides an illustration. The technique is a recent development, the approach is essentially intuitive and there is no data or analytical work supporting its benefits.

Although circumferential seams have been removed from the active portion of the coke drum, the length of vertical seams in this portion is increased. The vertical seams are aligned transverse to the hoop stress direction and may thus conceptually, pose a greater risk of longer crack failures in comparison to cracks forming in the circumferential seams.

Figure 2.4 Conventional versus Vertical Plate Construction [11]



New Drum – Conventional Plate Layout



New Drum – Vertical Plate Layout

2.2 Undisclosed Methodology

A proprietary assessment technology is provided by the Materials Property Council [MPC] named *CokerCOLA* [26]. The MPC is a not-for-profit scientific and technical corporation supported by industry [27]. Details are unavailable for non-members but Anderson [28] reports that the software predicts bulge formation, bulge growth, fatigue initiation and fatigue propagation in coke drums. This appears to be a fully analytical approach.

2.3 Unpublished Studies

Coker drums are found in refineries and oil sands operations and a significant body of work is available from individual owner organizations. Access was given to some of these studies [8] from a specific facility owner. The work is consistent with the published papers found in the literature. Of note is that the proprietary body of work is much more restricted in scope than that found in the open literature. For example, the number of measurement points for temperature and strain were limited to some 6 locations on a single drum, with only a single drum studied.

No alternative assessment approaches are given nor are any differing conclusions provided in the unpublished work sampled for this thesis. This private body of work does, however, provide greater insight into the calculation methodologies used in conducting integrity assessments and will be discussed later in this thesis.

2.4 Conclusions

The literature review indicates that the body of literature regarding coke drum damage and evaluation is limited and, either private or, in one instance, confidential. There exists a mix of qualitative information, a simplified level of analytical effort [governed by circumstances] and three empirical approaches for making proactive repair decisions. One approach uses Monte Carlo simulation [20]. The second approach utilizes geometric profiling with non-destructive AET to determine a repair decision [23]. The third approach is reliant on ranking the severity of geometric relationships in the pressure containing envelope [9]. The alternative fabrication approach is intuitive [11]. Data is unavailable for the confidential methodology [27, 28].

There are several difficulties in obtaining the needed data for performing a principles-based analytical evaluation for this specific equipment, including

1. economic restrictions
 - the need to maintain production making equipment inaccessible
 - cost and practicality of mounting a sufficient number of high temperature strain gauges and thermocouples
2. equipment size and operating environment
 - requires very large numbers of strain gauges and thermocouples to obtain meaningful data – one study used 75 thermocouples and 6 strain gauge pairs
 - many studies use as few as 5 thermocouples and matching strain gauge pairs, giving very limited coverage of the equipment surface
 - atmosphere in operating units is corrosive for some of the delicate instrumentation leading to limited life

3. unit reliability

- notwithstanding the failures listed previously, the coker drum design can be considered a qualified success with some units in service for over 50 years

4. variable loading

- although the operational steps are repeated nominally from cycle to cycle, the exact conditions of a specific cycle can vary significantly as described in detail earlier

The API industry survey data illustrates the diverse and contradictory experience in operating this equipment. Three of the more pertinent contradictions come from the 1996 API survey [7] indicating that

- while 80% of units surveyed experience bulging with 90% of these reporting cracking associated with the bulges, 80% of all units surveyed also experience cracking in non-bulged areas
- most cracking occurs in the upper shell courses, numbered 3, 4 and 5 while the prior surveys indicated bulging and presumably, cracking to be most severe at shell course 1 and decreasing in upper shell courses as indicated in Figure 2.1
- bulges average longer in length circumferentially than longitudinally but both are present. Figure 2.1 is nominally consistent with this statement, whereas data shown in Figure 2.2 from a unit in long-time service indicates bulges extend full vessel height

The literature is consistent in ascribing the cause of failure to low cycle fatigue induced by thermal loading.

CHAPTER 3 ELASTIC PLASTIC MATERIAL BEHAVIOUR

3.1 Stress – Strain Relationships

In large-scale mechanics, the intensity of force applied to a continuum is designated stress. To describe the complete state of stress acting upon any arbitrary portion of the body, it is necessary to describe the magnitudes and directions of the forces acting on all the planes passing through a point in the continuum. We accomplish this through the stress tensor, σ [29, 30] for which the components are defined:

$$\sigma_{ij} = \begin{bmatrix} \sigma_{xx} & \sigma_{xy} & \sigma_{xz} \\ \sigma_{yx} & \sigma_{yy} & \sigma_{yz} \\ \sigma_{zx} & \sigma_{zy} & \sigma_{zz} \end{bmatrix} = \begin{bmatrix} \sigma_{xx} & \tau_{xy} & \tau_{xz} \\ \tau_{yx} & \sigma_{yy} & \tau_{yz} \\ \tau_{zx} & \tau_{zy} & \sigma_{zz} \end{bmatrix} \quad (\text{for } i \text{ and } j = x, y \text{ and } z) \quad [3.1]$$

and, since $\tau_{xy} = \tau_{yx}, \tau_{xz} = \tau_{zx}, \tau_{yz} = \tau_{zy}$ due to equilibrium

$$\sigma_{ij} = \begin{bmatrix} \sigma_{xx} & \tau_{xy} & \tau_{xz} \\ \tau_{yx} & \sigma_{yy} & \tau_{yz} \\ \tau_{zx} & \tau_{zy} & \sigma_{zz} \end{bmatrix} = \begin{bmatrix} \sigma_{xx} & \tau_{yx} & \tau_{zx} \\ \tau_{xy} & \sigma_{yy} & \tau_{zy} \\ \tau_{xz} & \tau_{yz} & \sigma_{zz} \end{bmatrix} = \sigma_{ji}, \quad [3.2]$$

thus requiring six components of stress to specify the general state of stress at a point, three normal stresses, $\sigma_{xx}, \sigma_{yy}, \sigma_{zz}$ and three shearing stresses,

$\tau_{xy}, \tau_{xz}, \tau_{yz}$.

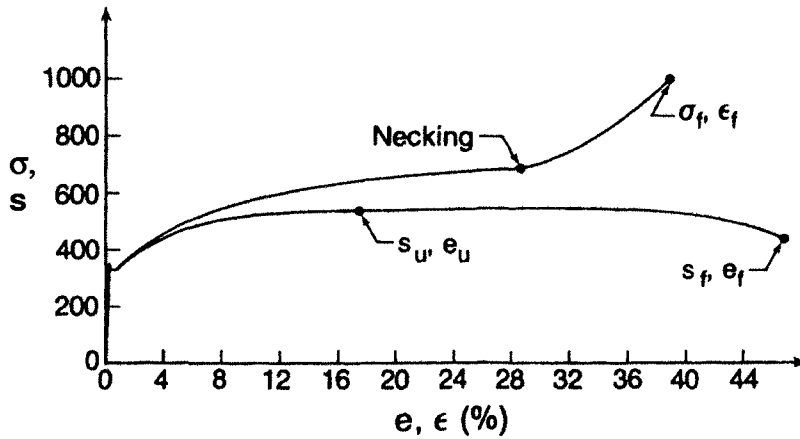
Similarly, the intensity of deformation of a volume of a body can be described in terms of magnitude and direction as a strain tensor ϵ , for which the components are defined:

$$\epsilon_{ij} = \begin{bmatrix} \epsilon_{xx} & \epsilon_{xy} & \epsilon_{xz} \\ \epsilon_{yx} & \epsilon_{yy} & \epsilon_{yz} \\ \epsilon_{zx} & \epsilon_{zy} & \epsilon_{zz} \end{bmatrix} \quad [3.3]$$

where ε_{ij} describes the total strain arising from the direct strain, ε_{ii} due to application of the normal stress components of the stress tensor σ , and ε_{ij} , where $i \neq j$, due to shear stresses $\tau_{xy}, \tau_{xz}, \tau_{yz}$. [29]

The relationship between strain and stress is exhibited by Figure 3.1 for a metal undergoing a uniaxial tension test to full failure [30]. There is an initial linear elastic portion. The transition from linear elastic to inelastic is termed the yield point. Up to approximately 4% elongation, the engineering stresses and strains are equivalent to the true stress and strain [31].

Figure 3.1 Material Monotonic Stress – Strain Curve [30]



We define the following

- true stress, $\sigma = \frac{P}{A_i}$ where [3.4]
P \equiv current load,
A_i \equiv instantaneous area

- true strain, $\varepsilon = \int_{l_0}^{l_f} \frac{\partial l}{l} = \ln \frac{l_f}{l_0}$ where [3.5]
 ∂l = infinitesimal elongation
l = instantaneous length
l_f = final length
l₀ = original length

- engineering stress, $\sigma = \frac{P}{A_0}$ where [3.6]
P \equiv current load
A₀ \equiv original cross-sectional area

- engineering strain, $e = \frac{\Delta l}{l_0}$ where [3.7]
 Δl = incremental elongation
l₀ = original length

The linear portion of the stress – strain curve extends for a very small portion of the total curve. By convention, an offset strain value of 0.2% is taken to be the yield strength of engineering materials [32, 33]. Deformation after the yield point is considered non-recoverable in comparison to elastic behaviour where unloading brings the body to its undeformed, original configuration. In Figure 3.1, the upper curve depicts the true stress-strain relationship and the lower curve depicts the engineering stress-strain relationship.

For linear isotropic elastic solids, the generalized Hooke's law can be stated in component form as [34]

$$\sigma_y = \begin{bmatrix} \sigma_{xx} \\ \sigma_{yy} \\ \sigma_{zz} \\ \sigma_{xy} \\ \sigma_{yz} \\ \sigma_{xz} \end{bmatrix} = \frac{E}{(1+\nu)(1-2\nu)} \begin{bmatrix} 1-\nu & \nu & \nu & 0 & 0 & 0 \\ \nu & 1-\nu & \nu & 0 & 0 & 0 \\ \nu & \nu & 1-\nu & 0 & 0 & 0 \\ 0 & 0 & 0 & 1/2-\nu & 0 & 0 \\ 0 & 0 & 0 & 0 & 1/2-\nu & 0 \\ 0 & 0 & 0 & 0 & 0 & 1/2-\nu \end{bmatrix} \begin{bmatrix} \epsilon_{xx} \\ \epsilon_{yy} \\ \epsilon_{zz} \\ \epsilon_{xy} \\ \epsilon_{yz} \\ \epsilon_{xz} \end{bmatrix} \quad [3.8]$$

Specialization to plane stress and restating in terms of the operative stress components, gives:

$$\epsilon_y = \begin{bmatrix} \epsilon_{xx} \\ \epsilon_{yy} \\ \epsilon_{zz} \\ \epsilon_{xy} \\ \epsilon_{yz} \\ \epsilon_{xz} \end{bmatrix} = \frac{1}{E} \begin{bmatrix} 1 & -\nu & -\nu & 0 & 0 & 0 \\ -\nu & 1 & -\nu & 0 & 0 & 0 \\ -\nu & -\nu & 1 & 0 & 0 & 0 \\ 0 & 0 & 0 & 2(1+\nu) & 0 & 0 \\ 0 & 0 & 0 & 0 & 2(1+\nu) & 0 \\ 0 & 0 & 0 & 0 & 0 & 2(1+\nu) \end{bmatrix} \begin{bmatrix} \sigma_{xx} \\ \sigma_{yy} \\ 0 \\ \sigma_{xy} \\ 0 \\ 0 \end{bmatrix}, \quad [3.9]$$

from which,

$$\left. \begin{aligned} \epsilon_{xx} &= \frac{\sigma_{xx}}{E} - \frac{\nu}{E} \sigma_{yy} \\ \epsilon_{yy} &= -\frac{\nu}{E} \sigma_{xx} + \frac{\sigma_{yy}}{E} \\ \epsilon_{zz} &= -\frac{\nu}{E} (\sigma_{xx} + \sigma_{yy}) \\ \epsilon_{xy} &= \frac{2(1+\nu)}{E} \sigma_{xy} \end{aligned} \right\} \xRightarrow{\text{and inverting}} \begin{aligned} \sigma_{xx} &= \frac{E}{(1-\nu^2)} (\epsilon_{xx} + \nu \epsilon_{yy}) \\ \sigma_{yy} &= \frac{E}{(1-\nu^2)} (\nu \epsilon_{xx} + \epsilon_{yy}) \\ \sigma_{xy} &= \frac{E}{(1-\nu^2)} \left(\frac{1-\nu}{2} \epsilon_{xy} \right) \end{aligned} \quad [3.10]$$

Classical elasticity defines the yield point as the failure limit. For uniaxial stress, we then define a failure when uniaxial stress $\sigma_{ii} \geq \sigma_{yield}$ [35]. [3.11]

For a multiaxial state of stress, the Huber-von Mises theory specifies that failure occurs when an equivalent stress, $\sigma_{eq} \geq \sigma_{yield}$, where

$$\sigma_{eq} \equiv \frac{1}{\sqrt{2}} \sqrt{(\sigma_{xx} - \sigma_{yy})^2 + (\sigma_{yy} - \sigma_{zz})^2 + (\sigma_{xx} - \sigma_{zz})^2 + 6 \cdot (\sigma_{xy}^2 - \sigma_{yz}^2 - \sigma_{xz}^2)^2}$$
[3.12]

Alternatively, principal normal stresses may be defined which are defined to occur on planes through the point of interest where the shearing stresses are zero. The principal normal stresses are local extremes of stress that include the maximum value of normal stress that can occur on any plane through the point.

$$\sigma_1 = \sigma_x$$
[3.13]

$$\sigma_2 = \frac{\sigma_y + \sigma_z}{2} + \sqrt{\left(\frac{\sigma_y - \sigma_z}{2}\right)^2 + \tau_{yz}^2}$$
[3.14]

$$\sigma_3 = \frac{\sigma_y + \sigma_z}{2} - \sqrt{\left(\frac{\sigma_y - \sigma_z}{2}\right)^2 + \tau_{yz}^2}$$
[3.15]

In terms of principal stresses, the equivalent stress may then be defined as

$$\sigma_{eq} \equiv \frac{1}{\sqrt{2}} \sqrt{(\sigma_1 - \sigma_2)^2 + (\sigma_2 - \sigma_3)^2 + (\sigma_1 - \sigma_3)^2}$$
[3.16]

The competing theory of failure is the Tresca maximum shearing stress theory which simply states that elastic failure occurs when the principal shear stress exceeds the principal shear stress in failure in a uniaxial test, $\tau \geq \tau_f$ [3.17]

Therefore, since $\tau_f = \frac{\sigma_f}{2}$, failure in a multiaxial state of stress is [3.18]

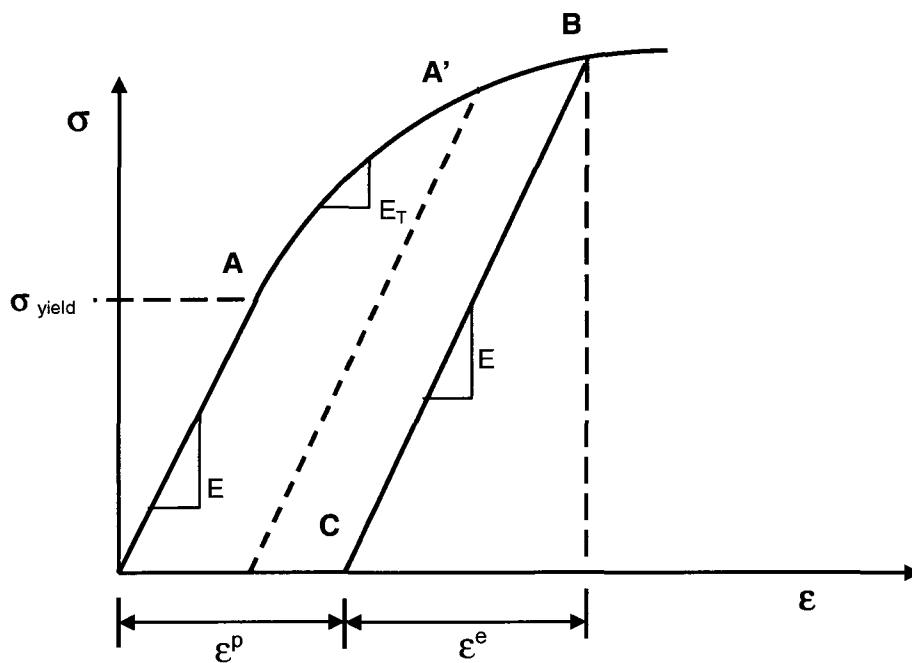
defined to occur when any of $\tau_i = \frac{\sigma_i - \sigma_j}{2} \geq \frac{\sigma_{yield}}{2}$. [3.19]

Industrial design codes have used this definition of failure because of the slightly greater conservatism provided by this criterion [36].

3.2 Plasticity

The action of the stress-strain curve beyond the elastic limit is characterized as the flow curve. The state of stress after initial yield is defined coincident with the Huber - von Mises stress definition. There are three features of interest in the flow curve which are of interest for this thesis.

Figure 3.2 Material Stress – Strain Curve with Unloading [37]



In reference to Figure 3.2:

- increasing stress as strain increases or strain hardening, as point A progresses to point B
- the special case of non-hardening plasticity, where the path from A to B is parallel to the strain axis, i.e. tangent modulus, $E_T = 0$
- linear unloading behaviour as B progresses to C

The first feature provides a criterion by which a structure, on reaching yielding does not risk imminent failure. This forms the basis of the limit load concept.

The second feature provides a mechanism by which incremental distortion occurs but without a corresponding increase in stress.

The third feature is that the modulus of elasticity on unloading is equal to the modulus of elasticity on original loading.

In general, the elastic-plastic stress-strain relationship can be given in the Prandtl-Reuss form as $d\epsilon_y^t = d\epsilon_y^p + d\epsilon_y^e$; the total strain increment being composed of the plastic strain portion, $d\epsilon_y^p$ and elastic strain increment portions, $d\epsilon_y^e$.

The elastic strain increment portion, $d\epsilon_y^e$ may be further simplified as $d\epsilon_y^e \propto d\sigma_y$, the generalized Hooke's law. The incremental plastic portion of the Prandtl-Reuss relationship $d\epsilon_y^p$ is equated by the associated flow rule as,

$$d\epsilon_y^p = d\lambda \cdot \frac{\partial f(\sigma_y)}{\partial \sigma_y} \text{ where } \partial f(\sigma_y) \text{ is a plastic potential, or the yield stress}$$

surface and, $d\lambda$ characterizes the incremental hardening behaviour of the material, but is a non-negative scalar quantity, is not a material constant and may vary throughout the stress history.

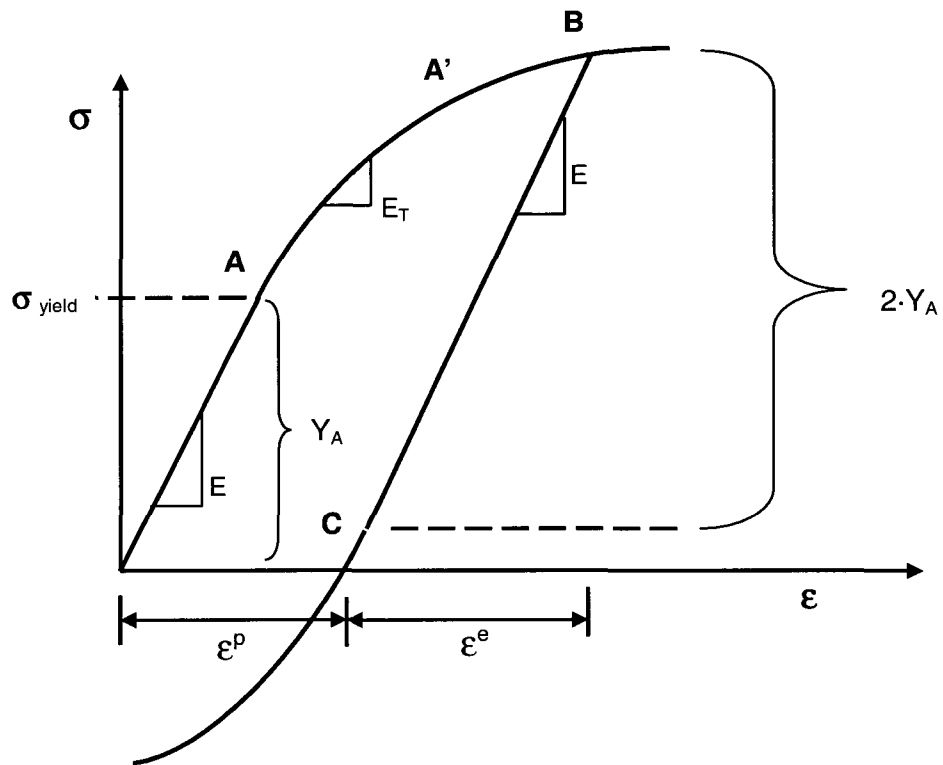
3.3 Isotropic Hardening

Referring to Figure 3.2, as the yield surface expands beyond the yield point A, increasing stress is required to increase plastic flow. When the stress direction is reversed, the material unloads elastically parallel to the line from the origin to A. If initial yielding is designated Y_A and the increased yield point is designated intermediate to a point between A and B at point A', designated $Y_{A'}$, then on reloading, the yield strength point will be at $Y_{A'}$. For isotropic hardening, the yield strength range is idealistically taken to be $2 \cdot Y_{A'}$ under load reversal conditions. The yield strength range in isotropic hardening continues to expand as plastic strain increases to the tensile strength limit. [30]

3.4 Kinematic Hardening

In kinematic hardening, the yield strength range is limited to $2 \cdot Y_A$ but the yield strength value increases as strain is increased beyond the prior loading. That is, the yield strength can increase from point A' in Figure 3.2 to point B, i.e. Y_B but on reversal, the yield strength value will be $Y_B - 2 \cdot Y_A$. Therefore, in terms of a yield surface, the yield surface size remains the same but can translate in stress space. This observation in the response of real materials is known as the Bauschinger effect. Figure 3.3 illustrates the concept of kinematic hardening.

Figure 3.3 **Material Stress – Strain Curve with Load Reversal** [37]



3.5 Temperature Effects

For isotropic materials, the temperature rise ΔT results in a uniform strain which depends on the coefficient of linear expansion, α of the material [34], that is –

$\epsilon_{thermal} = \alpha \cdot \Delta T$, and for a linear, isotropic material

$$[\epsilon_{thermal}] = \begin{bmatrix} \alpha \cdot \Delta T \\ \alpha \cdot \Delta T \\ \alpha \cdot \Delta T \\ 0 \\ 0 \\ 0 \end{bmatrix} \quad [3.17]$$

and thus, the total strain is

$$\epsilon^T = [\epsilon_{mech}] + [\epsilon_{thermal}], \quad [3.18]$$

that is, a sum of mechanical and thermal strains.

The thermal strain does not cause any mechanical strains and stresses when the structure is free to deform. If constraint occurs, then mechanical strains and stresses will be induced. The constraint may be either external or internal. External constraint occurs, for example when a straight bar is subjected to a temperature change throughout while held at the ends. Internal constraint occurs, for example when a solid body, at uniform temperature, is suddenly subjected to a temperature change $\Delta T > 0$ resulting in compressive stress in the surface layers since the whole of the body is not able to instantaneously change to the new temperature, but requires a finite amount of time to equilibrate to a new, uniform temperature.

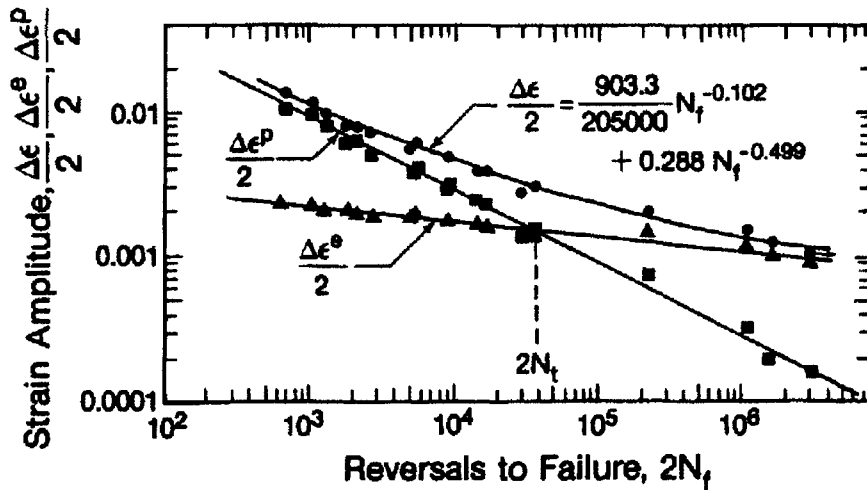
3.6 Low Cycle Fatigue

Low cycle fatigue is a material failure mechanism whereby fracture is associated with repeated loading and where the number of repetitions in loading is comparatively small in number. Low cycle fatigue may also be said to correspond to strain - controlled fatigue since fatigue is accompanied by a significant amount of plastic deformation. This is illustrated phenomenologically in Figure 3.4 [30] by means of the Coffin-Manson-Basquin law [38] being of the

$$\text{form } \frac{\Delta \epsilon}{2} = \frac{\Delta \epsilon^e}{2} + \frac{\Delta \epsilon^p}{2} = \frac{\sigma_f'}{E} \cdot (2N_f)^\beta + \epsilon_f' \cdot (2N_f)^\beta \quad [3.19]$$

showing that fatigue is a combination of elastic and plastic strain components but where the plastic strain component dominates at the lower number of cycles. Low cycle fatigue can generally be said to extend from 1 to 50,000 cycles, the latter value corresponding roughly to the crossover of elastic and plastic curves.

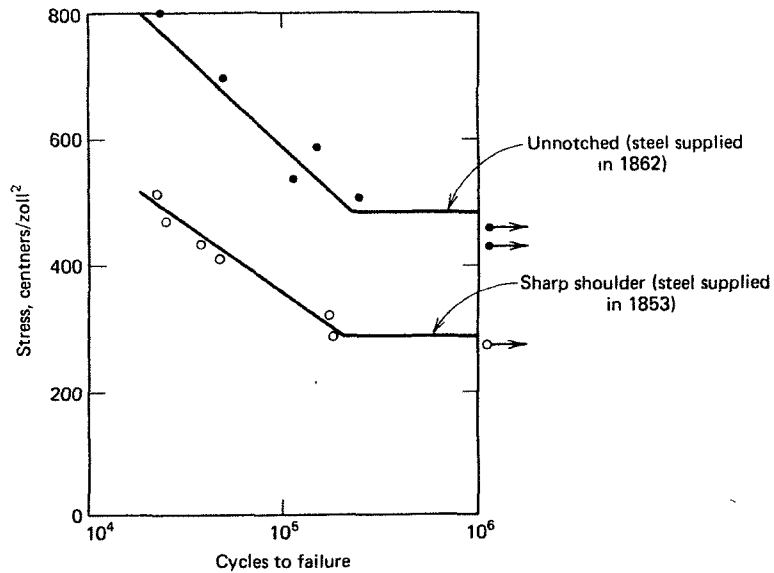
Figure 3.4 Fatigue Curve [30]



The plastic portion of the law attributed to Coffin and Manson is expressed in the form $N_f^\beta \cdot \Delta \epsilon^p = \epsilon_f'$ where N_f is the number of cycles, ϵ_f' is correlated with the tensile ductility and β is a material constant which ranges between 0.45 and 0.6. The elastic portion is given by the Basquin law, $\Delta \epsilon^e = \Delta \sigma / E = (B/E) N^{-\beta'}$. B is a material constant; E is Young's modulus and β' is another material constant ranging between 0.10 and 0.15.

Formal fatigue investigations are reported to have been first conducted in the mining industry in the early 18th century on iron chain and on the axles of stage coaches. The failure of stage coach axles carried through to failure of railcar axles as railway systems developed in the mid-18th century. The first systematic investigations were conducted by August Wöhler between 1852 and 1870 on both full size and laboratory scale specimens. The data collected from these tests were presented in the form shown in Figure 3.5 depicting stress as a function of cycles to failure. The present day terminology is to call the data presented in this manner an S-N diagram. Occasionally, reference is made to the Wöhler diagram [35]. Data presented in the form of strain versus cycles to failure is known as an ϵ - N diagram.

Figure 3.5 Fatigue Data of Wöhler [35]



The data in Figure 3.5 suggests a relationship between cyclic life and stress concentrations with specimens containing notched features, indicated by the sharp shoulder, causing reduced fatigue life.

The literature [35, 36, 39] indicates a number of factors affecting the determination of fatigue life which precludes attributing fatigue life as a material property.

These basic considerations include

- simple reversed loading versus mean load with alternating stress
- multiaxial state of stress
- effect of stress gradients
- effect of residual stresses
- effect of stress raisers
- effect of surface finish
- effect of temperature
- size effects
- statistical variation in fatigue measurement
- effect of environment
- interaction effects with other failure modes

While the data of Figure 3.5 provides conceptual understanding of fatigue, the failure mechanism is explained on a microscopic scale as a process of initiation and propagation of cracks to an unstable size. Dislocation theory is used to explain the development of fatigue crack nuclei and fine slip bands at crystal lattice surfaces which are the precursor to fine cracks that develop as loads fluctuate [40, 41].

As indicated in Figure 3.4, a cross over point in which fatigue passes from low cycle to high cycle fatigue occurs in the range of 30,000 to 50,000 cycles. In high cycle fatigue, the stresses are elastic and most of the life of the component is taken up in crack initiation. In low cycle fatigue, high levels of plastic strain occur resulting in low cycle counts to onset of crack initiation with the majority of cyclic life spent in crack propagation.

As an alternative description to low cycle fatigue, the term strain-controlled fatigue is frequently used and hence, the $\epsilon - N$ diagram. Table 3.1 compares the primary elements of ASTM A 322 Grade 4130 and Grade 4340 to SA 516 70 and SA 387 Grade 12. ASTM A322 4130 and ASTM A322 4340 are carbon, low alloy steels that are somewhat similar in composition to the SA 387 Cr – Mo alloys used for coke drum fabrication.

Table 3.1 Chemical Compositions of Materials of Construction

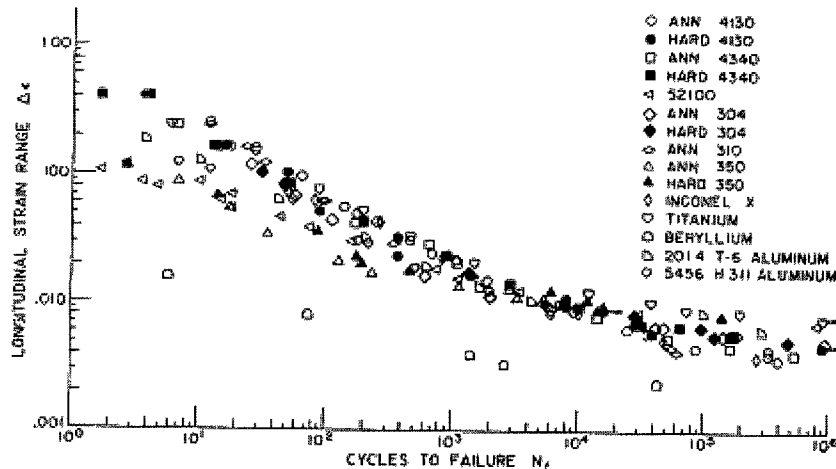
Material	C	Mn	Cr	Mo	P	S	Si	Ni
A322 4130	.31	.5	1	.2	.035	.04	.25	-
A322 4340	.41	.7	.8	.25	.035	.04	.25	-
SA 516 70	.28	1.0	-	-	.035	.035	.45	-
SA 387 12	.1	.5	1	½	.035	.035	.3	-

Notes to Table 3.1

1. Nominal compositions are given; see reference [4] for composition limits.
2. Other trace and alloying elements may be present as provided for by Code.

In Figure 3.6, the strain range is plotted against cycles to failure for a number of materials, including Grade 4130 and Grade 4340 materials.

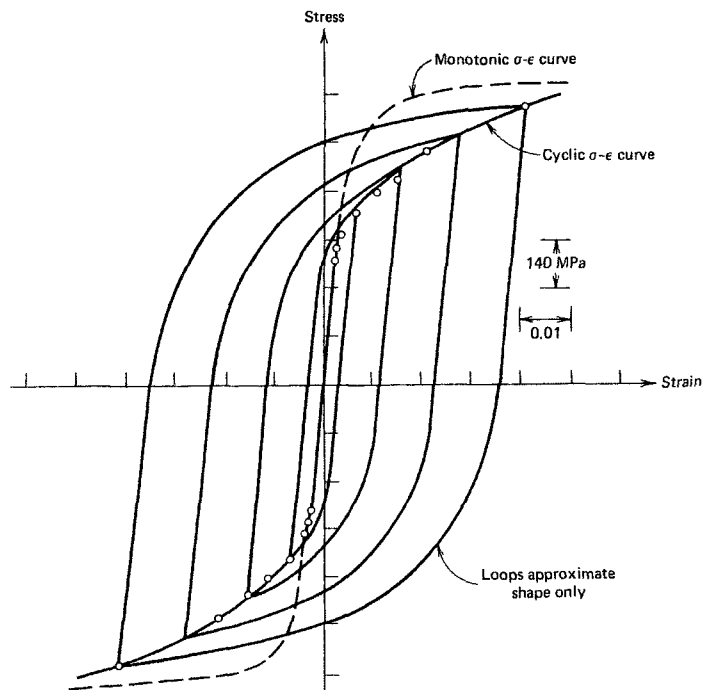
Figure 3.6 Strain versus Cyclic Life [42]



The data of Figure 3.6 suggest that low chrome – molybdenum alloy carbon steels may have a crossover point or “transition life”, in the vicinity of 10,000 to 20,000 cycles. This may have implication on the selection of materials for the coke drum which experience nominal lifetimes of approximately 9,125 stress reversals [$2 \cdot N_f$].

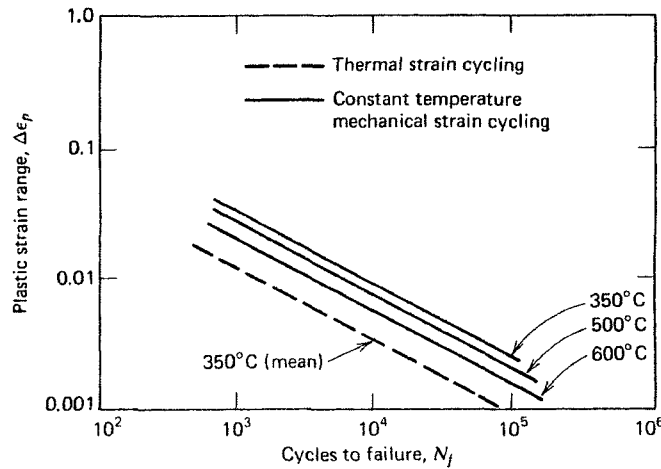
Cyclic straining into the plastic range alters the stress-strain response of metals leading to either cyclic strain hardening or cyclic strain softening. This response will deviate from the monotonic stress-strain curve which represents a $\frac{1}{4}$ cycle fatigue exposure. Figure 3.7 illustrates that ASTM A 322 4340 low alloy steel cyclic softens. The implication is that a stress based determination may not accurately determine the fatigue life without correction for the effects of cyclic softening and hardening. A strain based determination does not require correction.

Figure 3.7 Cyclic Stress-Strain Curve – Grade 4340 [42]



An important and unusual study reported in [43] on work conducted by Baldwin, Sokol and Coffin compares mechanically induced strain fatigue to thermally induced strain fatigue. The experiment involved determination of the mechanical fatigue life at varying high temperatures. The program was repeated for specimens cycled through the same strain range by varying the temperature of a constrained specimen. Figure 3.8 shows the results of this testing. For equal values of cyclic plastic strain, the number of cycles to failure for the thermal-strain cycled material was much less than for the mechanical-strain cycled specimen.

Figure 3.8 Comparison of Mechanical to Thermal Strain Cycling [42]



At a strain of 0.01, the thermal-strain cycled specimen has an approximate life of 1,000 cycles at a mean temperature of 350 °C, whereas the mechanical-strain cycled specimen has a measured life of nearly 10,000 cycles at a constant temperature of 350 °C and a life of nearly 3,000 cycles at 600 °C. The thermally strained specimen was cycled between 250 °C and 500 °C to obtain a mean temperature of 350 °C. Experimental error attributed to strain localization was cited by Manson; however, no satisfactory reconciliation of this behaviour was found. Manson suggested a strength reduction factor of 2.5 for thermal-stress strained loading.

CHAPTER 4 MATERIALS TESTING

4.1 Primary Properties of Interest

A number of basic mechanical tests were completed to provide a comparison to some of the mechanical properties data available in the literature which are listed in Table 4.1. The candidate test material was a section of clad plate provided by a local fabricator regularly engaged in the fabrication of coke drum vessels. The test piece, specifically SA 387 Grade 11 with a clad layer of SA 240 TP 410S, was surplus from a recently completed coke drum delivered to an oil sands facility. Testing was performed to establish for both base plate and clad material, the following:

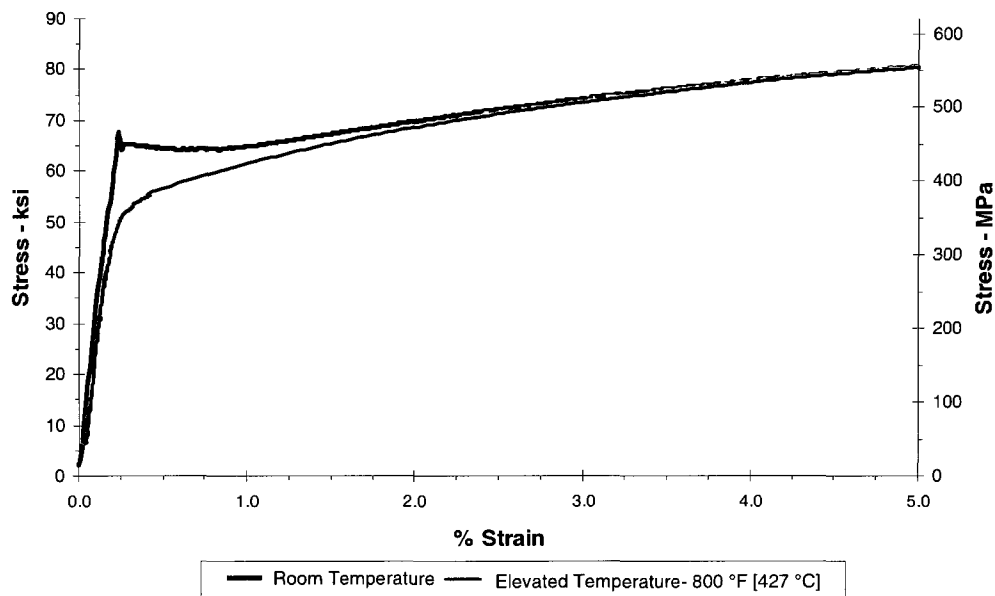
- monotonic stress-strain behaviour at room temperature
- monotonic stress-strain behaviour at elevated temperature
- cyclic stress-strain behaviour at room temperature
- cyclic stress-strain behaviour at elevated temperature

4.2 Testing Results

Figure 4.1 shows results for the monotonic testing of the base plate material to establish the stress – strain curve at room temperature and at an elevated temperature of 800 °F [427 °C]. There are two noteworthy observations. Firstly, the room temperature 0.2% offset yield strength value is approximately 65,000 psi [448 MPa]. Secondly, the room temperature flow curve, i.e. the extension of the stress strain curve past yield shows a decreasing trend to almost 1% strain and then begins to rise and surpasses the initial yield point at about 1.25% strain. Reference [43] shows a similar trend for 2¼ Cr – 1Mo alloy steel tested under monotonic conditions.

Whereas the room temperature monotonic curve exhibits initial strain softening post yield, the elevated temperature curve exhibits strain hardening.

Figure 4.1 Monotonic Curves for SA 387 11 Plate – Room & Elevated Temperatures



Notes to Figure 4.1

1. ASME SA 387 11 plate material is referred to as 1¼ Cr – ½ Mo plate for brevity.
2. Compare to monotonic cyclic stress-strain curve to Figure 3.7

The manufacturer's test results [MTR] is a certified legal document accompanying the plate supplied for pressure vessel construction. The MTR for this plate lists 0.2% offset yield strength measurements of 56,000 psi [386.1 MPa] and 60,200 psi [415.1 MPa]. The proportional limit of the current test is approximately 65,000 psi [448 MPa], being even greater than the 0.2% offset yield strength listed in the MTR, in this instance.

Note, that for the design of Code pressure vessels, the use of the specified-minimum-yield-strength [SMYS] value is mandated. The room temperature SMYS is 35,000 psi [241.3 MPa].

The monotonic 0.2% offset yield strength result at elevated temperature is approximately 56,000 psi [386 MPa] and compares to a SMYS value of 25,200 psi [173.8 MPa]. The proportional limit is 35,000 psi [241 MPa].

Table 4.1 Physical Properties for Materials of Construction [10]

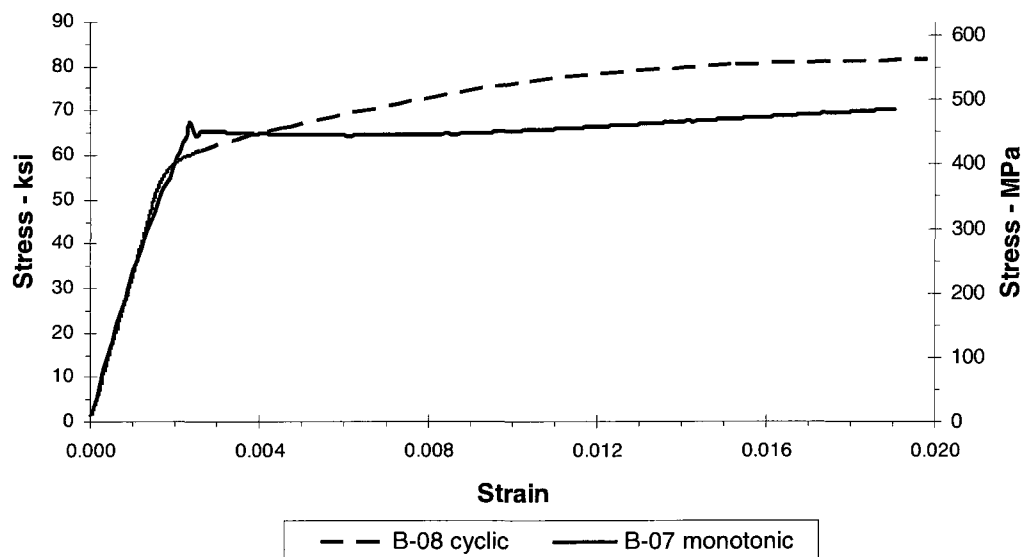
Material Description	Temp [F]	SMYS [ksi]	SMTS [ksi]	S _a [ksi]	S _m [ksi]	E [psi]	CTE [1/ F]	TC [Btu / hr-ft-F]
13 Cr – TP 410S	100	30.0	60.0	17.1	16.7	29.2 E6	6.0 E-6	14.2
SA 240	800	22.7	49.3	14.1	15.1	24.7 E6	7.1 E-6	14.7
12 Cr – TP 405	100	25.0	60.0	16.7	16.7	29.2 E6	6.0 E-6	14.2
SA 240	800	18.9	49.3	12.6	12.6	24.7 E6	7.1 E-6	14.7
ERNiCrMo-3	100	60.0	120.0	-	-	20.0 E6	6.8 E-6	5.8
UNS N06625	800	49.3	109.2	-	-	26.7 E6	8.0 E-6	9.1
2¼ Cr - SA 387 G22 Class 1	100	30.0	60.0	17.1	25.0	30.6 E6	6.5 E-6	21.0
	800	26.6	58.2	16.6	17.8	26.3 E6	8.9 E-6	20.2
1¼ Cr - SA 387 G11 Class 1	100	35.0	60.0	17.1	20.0	29.7 E6	6.5 E-6	23.6
	800	25.2	60.0	16.8	16.8	25.5 E6	8.9 E-6	21.0
C – ½ Mo -	100	43.0	75.0	21.4	25	29.2 E6	6.5 E-6	23.6
SA 204 C	800	32.1	75.0	21.4	*	23.9 E6	8.9 E-6	21.0

Notes to Table 4.1

- * ≡ not permitted above 700 F (S_m = 21.7 ksi @ 700 F) per ASME II Part D [10]
- Table 4.1M provides the data in SI units, at end of section

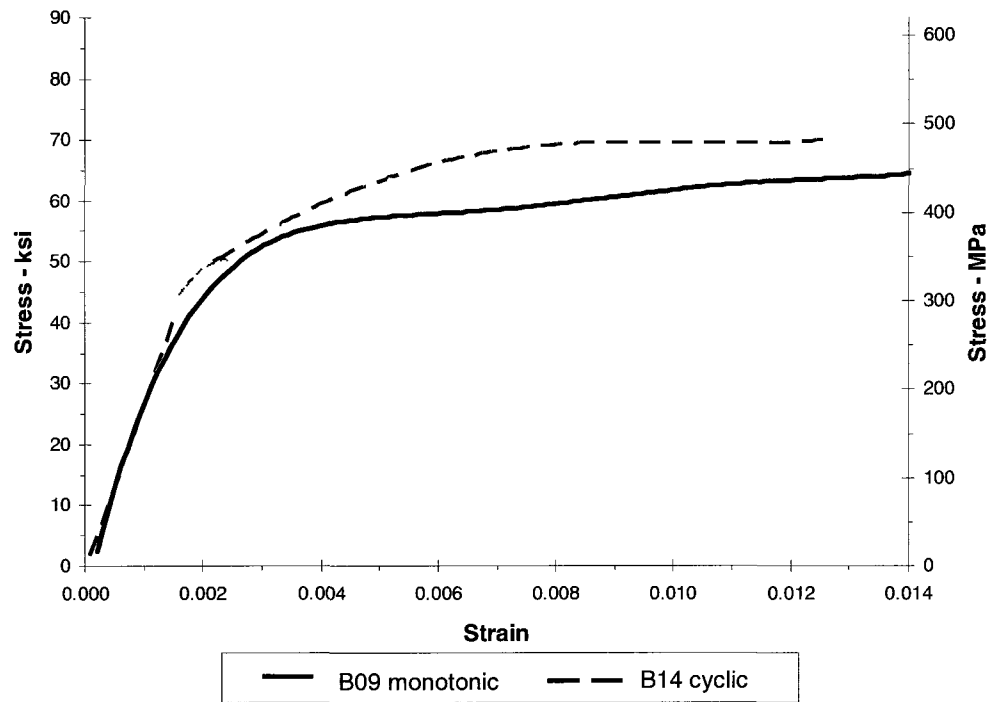
The cyclic stress strain curve in Figure 4.2 compares the room temperature cyclic stress-strain curve to the monotonic stress-strain curve. For the cyclic stress-strain curve, the proportional limit strength of 55,000 psi [379 MPa] is determined with initial softening occurring post yield and then hardening. A plateau occurs near a strain amplitude of 0.020 or 2.0%, although it is not evident from the figure.

Figure 4.2 Comparison of Monotonic to Cyclic Stress Strain Curve for Sampled SA 387 11 [1¼ Cr –½ Mo] Plate – Room Temperature



The comparison of the monotonic to cyclic stress strain curves at an elevated temperature of 800 °F [427 °C] is shown in Figure 4.3 up to a limited strain amplitude of 2%. For the monotonic stress-strain curve, the proportional limit strength is approximately 30,000 psi [207 MPa], slightly less than determined from Figure 4.1. The proportional limit for the cyclic stress curve is approximately 45,000 psi [310 MPa]. Both are greater than the Code required SMYS value of 25,200 psi [173.8 MPa] at 800 °F [427 °C].

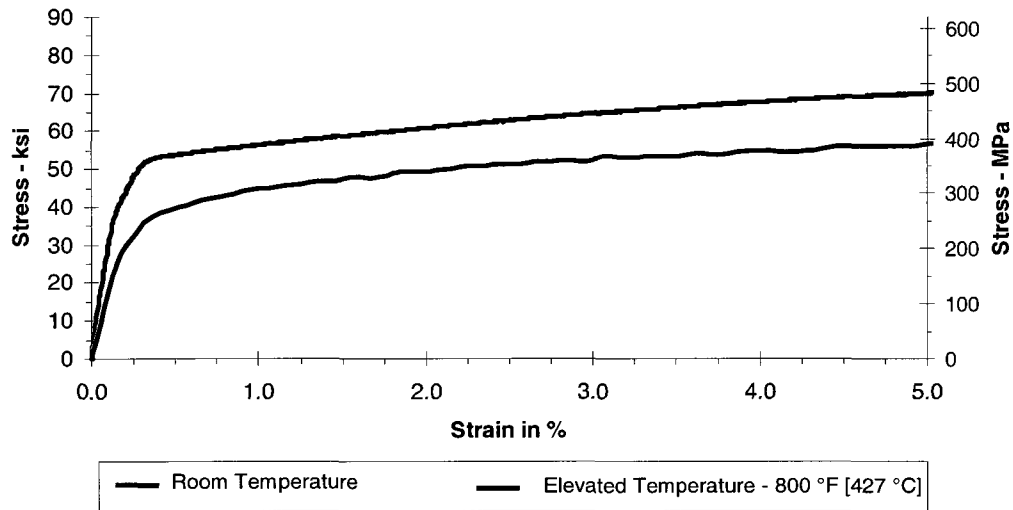
Figure 4.3 Comparison of Monotonic to Cyclic Stress Strain Curve for Sampled SA 387 11 [1¼ Cr – ½ Mo] Plate – Elevated Temperature – 800 °F [427 °C]



Notes to Figure 4.3

1. SA 387 11 is commonly referred to as 1¼ Cr – ½ Mo plate for brevity.

Figure 4.4 Comparison of Monotonic Stress Strain Curve for Sampled SA 240 TP 410S Clad – Room & Elevated Temperatures

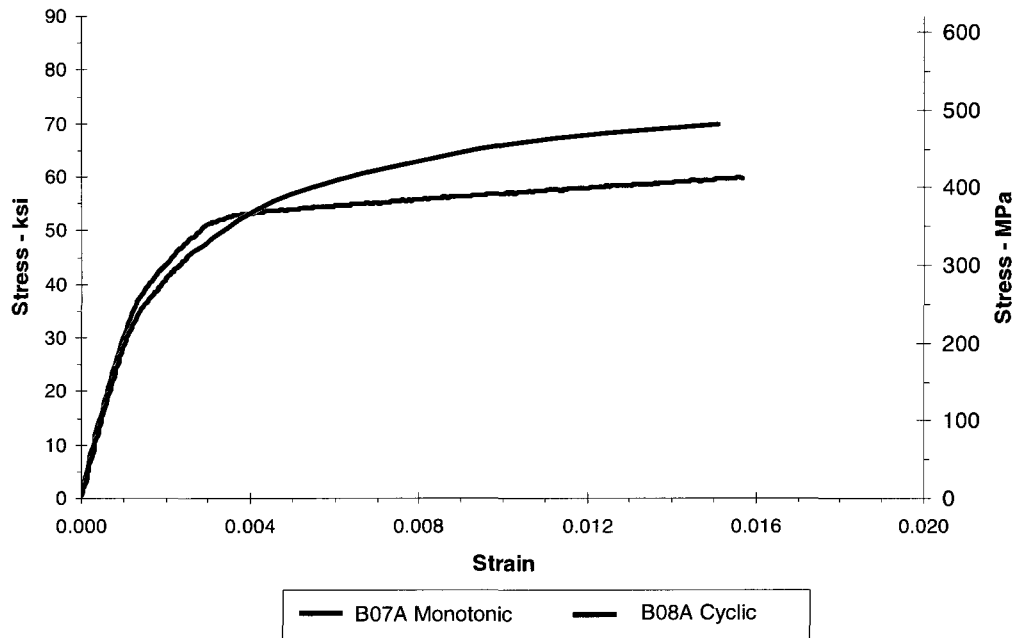


Notes to Figure 4.4

1. Test temperatures are at room temperature and 800 °F [427 °C]
2. SA 240 TP 410S is commonly referred to as 410S alloy for brevity.

At room temperature, the measured 0.2% offset yield strength for TP 410S cladding is 54,000 psi [372.3 MPa], shown in Figure 4.4 and this value is greater than the SMYS value of 30,000 psi [206.8 MPa]. The proportional limit is approximately 38,000 psi [262 MPa]. The high temperature stress strain curve shows a 0.2% offset yield strength of approximately 39,000 psi [268.9 MPa] compared to the high temperature SMYS of 22,700 psi [156.5 MPa]. The proportional limit is 24,000 psi [165.5 MPa].

**Figure 4.5 Comparison of Monotonic to Cyclic Stress Strain Curves for
Sampled SA 240 TP 410S Clad – Room Temperature**

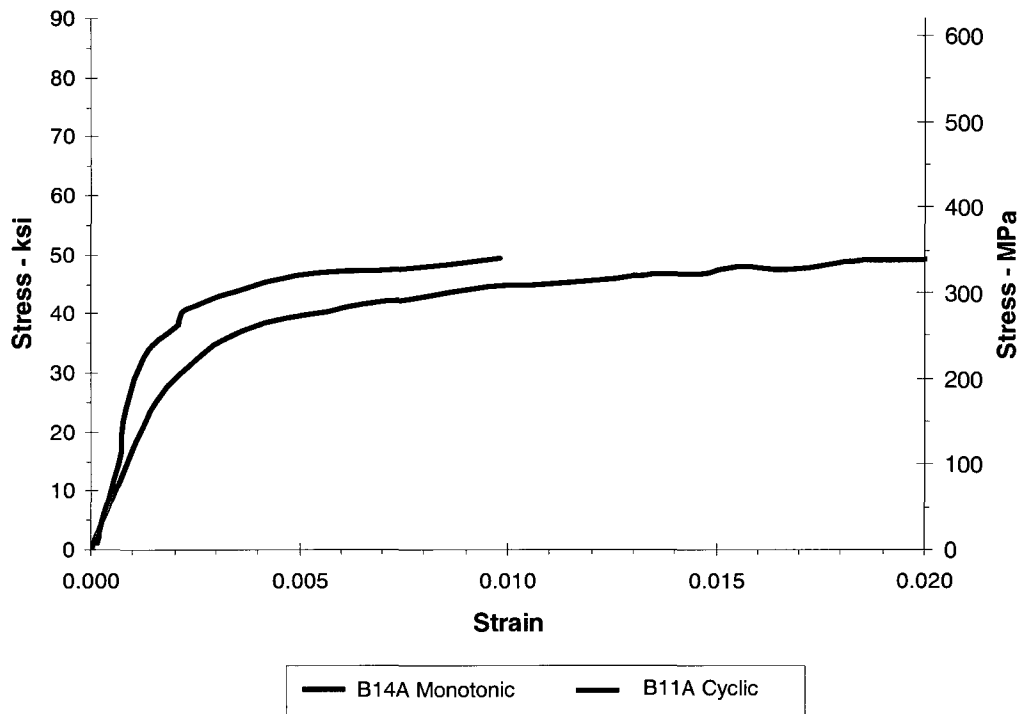


Notes to Figure 4.5

1. Test temperature is at room temperature
2. SA 240 TP 410S is commonly referred to as 410S alloy for brevity.

The cyclic stress strain curve at room temperature in Figure 4.5 shows a cyclic proportional limit of approximately 32,500 [224 MPa] and a monotonic proportional-limit of 37,000 psi [255 MPa]. A slight softening occurs to 0.004 strain followed by hardening.

**Figure 4.6 Comparison of Monotonic to Cyclic Stress Strain Curve for
Sampled SA 240 TP 410S Clad – Elevated Temperature –
800 °F [427 °C]**



The cyclic stress strain curve at an elevated temperature of 800 °F [427 °C] in Figure 4.6 shows a cyclic proportional limit approaching approximately 35,000 psi [241 MPa]. There is some difficulty in determining the cyclic data at elevated temperature, but the trend clearly shows that cyclic hardening takes place.

The above findings are summarized in Table 4.2.

Table 4.2 Comparison of Specified to Measured Monotonic Properties – Room Temperature

Material Description	SMYS	YS*	YS**	SMTS	TS*	TS**	E	E**	ETAN**
1¼ Cr - SA 387 G11 Class 1	35.0	62.5	64	60.0	80.3	86	29.7E3	28.8E3	2.02E3
13 Cr – TP 410S SA 240	30.0	n.a.	54	60.0	n.a.	76	29.2E3	29.1E3	1.03E3

Notes to Table 4.2

1. * indicates property as per manufacturer's Material Test Report
2. ** indicates property measured from testing data
3. All values in [ksi] at room temperature
4. Table 4.2M provides the data in SI units, at end of section

4.3 Conclusions – Materials Testing

Experimentally determined data obtained during the course of this thesis indicate that the materials of construction have

1. much greater yield strength than the industry practice specified minimum yield strength
2. the monotonic stress – strain curve for the base material behaves essentially elastic – perfectly plastic over the strain range of interest for this application
3. the cyclic stress – strain curve for the base material initially cyclic softens and then hardens over the strain range of interest at room temperature
4. the cyclic stress – strain curve for the clad liner cyclic softens and then hardens over the strain range of interest at room temperature
5. the cyclic stress – strain curve for the base material cyclic hardens over the strain range of interest at elevated temperature
6. the cyclic stress – strain curve for the clad liner material cyclic hardens over the strain range of interest at elevated temperature

Table 4.1M Physical Properties for Materials of Construction– SI Units [10]

Material Description	Temp [°C]	SMYS [MPa]	SMTS [MPa]	S _a [MPa]	S _m [MPa]	E [MPa]	CTE [1/ °C]	TC [W / m-°K]
13 Cr – TP 410S	37 8	206 8	413 7	117	115	201 E6	3 33 E-6	24 6
SA 240	427	156 5	340 0	97	104	170 E6	3 94 E-6	25 5
12 Cr – TP 405	37 8	172 4	413 7	115	115	201 E6	3 33 E-6	24 6
SA 240	427	130 3	340 0	87	87	170 E6	3 94 E-6	25 5
ERNiCrMo-3	37 8	413 7	827 4	-	-	138 E6	3 78 E-6	10 0
UNS N06625	427	340 0	752 9	-	-	184 E6	4 44 E-6	15 8
2¼ Cr - SA 387 G22 Class 1	37 8	206 8	413 7	117	172	210 E6	3 61 E-6	36 4
	427	183 4	401 3	114	122	181 E6	4 94 E-6	35 0
1¼ Cr - SA 387 G11 Class 1	37 8	241 3	413 7	117	138	204 E6	3 61 E-6	40 9
	427	173 8	413 7	115	115	175 E6	4 94 E-6	36 4
C – ½ Mo -	37 8	296 5	517 0	147	172	201 E6	3 61 E-6	40 9
SA 204 C	427	221 3	517 0	147	*	164 E6	4 94 E-6	36 4

Notes to Table 4.1M

- 1 * ≡ not permitted above 371 °C (S_m = 149 6 MPa @ 371 °C) per ASME II Part D [10]

Table 4.2M Comparison of Specified to Measured Properties – Room Temperature - SI Units

Material Description	SMYS	YS*	YS**	SMTS	TS*	TS**	E	E**	ETAN**
1¼ Cr - SA 387 G11 Class 1	241 3	431	441	414	554	593	205 E3	199 E3	13 9 E3
13 Cr – TP 410S SA 240	206 8	n a	372	414	n a	524	205 E3	201 E3	7 10 E3

Notes to Table 4.2M

- * indicates property as per manufacturer's Material Test Report
- ** indicates property measured from testing data
- All values in [MPa] at room temperature

CHAPTER 5 CHARACTERIZATION OF THERMO MECHANICAL LOADING

5.1 Loads Imposed During Operational Sequencing

There are 4 primary sources of loading on a coke drum.

- dead weight
- live-weight
- pressure
- temperature

Deadweight loading consists of the empty vessel weight and non-operating external loads from attached equipment. This load is essentially constant through the life of the vessel under all operating conditions.

Live-weight loading consists of the contents weight of the vessel consisting of coke and water. The live-weight loading is cyclic since the vessel is filled and emptied repeatedly with coke and water, sequentially. The rate of loading and unloading during coke and water filling and emptying can be characterized as ramped loadings.

Pressure is the internal operating pressure of the vessel. The pressure is increased sufficiently quickly from atmospheric to a target pressure to be considered a step increase. Pressure is held nominally constant starting at steam test through to completion of water quench when a step decrease occurs. The sequence of steps from steam test to completion of water quench can also be termed as the extended coking cycle. If the steam test does not hold, pressure is reduced to atmospheric conditions while correction is made. Therefore, the vessel could be exposed to multiple pressure-cycling for each coking cycle. This load is therefore cyclic and repeats essentially consistently from cycle to cycle. Pressure is normally a monitored and recorded parameter for this specific equipment.

As indicated in Table 1.3, there is a nominal temperature loading that repeats at each cycle of operation. These loads are the planned and operator controlled loads necessary for the effective operation of the vessel. The fluid streams entering the vessel are known and quantified with regard to volume rates, temperatures, pressures and other stream properties. Variations may occur due to operator intervention or plant conditions, such as delaying start and stop times, altering volumetric rates or modifying fluid stream temperatures.

The magnitude of deadweight, live-weight and pressure loads and their operating ranges are known and certain quantities. In comparison, while the range of temperature change is known, the spatial distribution of shell metal temperature and time at which the temperature occurs become uncertain during specific parts of the operational sequence leading to large temperature differences between adjacent portions of the coker drum shell and accompanying large, thermally induced strains. The detailed explanation of this difficulty follows.

Temperature changes occur in the vessel wall as the various operational steps progress. The temperature loading in Table 1.3 lists discrete increases from ambient temperature through to the “oil in” operational step and then step wise decrements. However, the temperatures of interest for this work are the vessel wall temperatures during this progression and in particular, as shown later, the differences in temperature between adjacent portions of the vessel. Figure 5.1 is a representative illustration of vessel wall temperatures during a coke cycle. The data is taken from five thermocouples mounted on the drum shell at three elevations. One thermocouple is mounted at the skirt [elevation 0' or 0 m] and two thermocouples are mounted approximately at the thirty foot elevation [elevation 30' or 9200 mm] of the drum cylinder and two thermocouples at the forty foot elevation [elevation 40' or 12200 mm]. The shell mounted thermocouples are also offset between elevations.

Shell metal temperature is not normally monitored or recorded in an operating facility. However, inlet oil temperature and outlet vapour temperatures are normally monitored and recorded as these are process parameters needed for operational control.

The temperature measurements show five distinct operating phases corresponding to the operational steps listed in Table 1.3. These are specifically, steam test, vapor heat, oil-in and fill, steam quench and, water quench. All thermocouples are seen to respond somewhat simultaneously during steam test, vapor heat and the beginning of oil in. As the oil-in step continues and the bitumen level rises past the skirt thermocouple, the temperature at that elevation begins to decline. After several hours, the bitumen level rises above the shell course 4 thermocouple level and the temperature trend indicates a decline. After some time, bitumen level passes the shell course 5 thermocouples and a declining temperature trend is indicated. At completion of oil in, the steam quench step occurs. Steam quench does not appear to have any impact on shell temperatures. Following immediately is the lengthy water quench step. The ramp down trend for shell course 5 remains consistent but shell course 4 does show a short and rapid rise midway through the step but then converges with the trend lines of shell course 5.

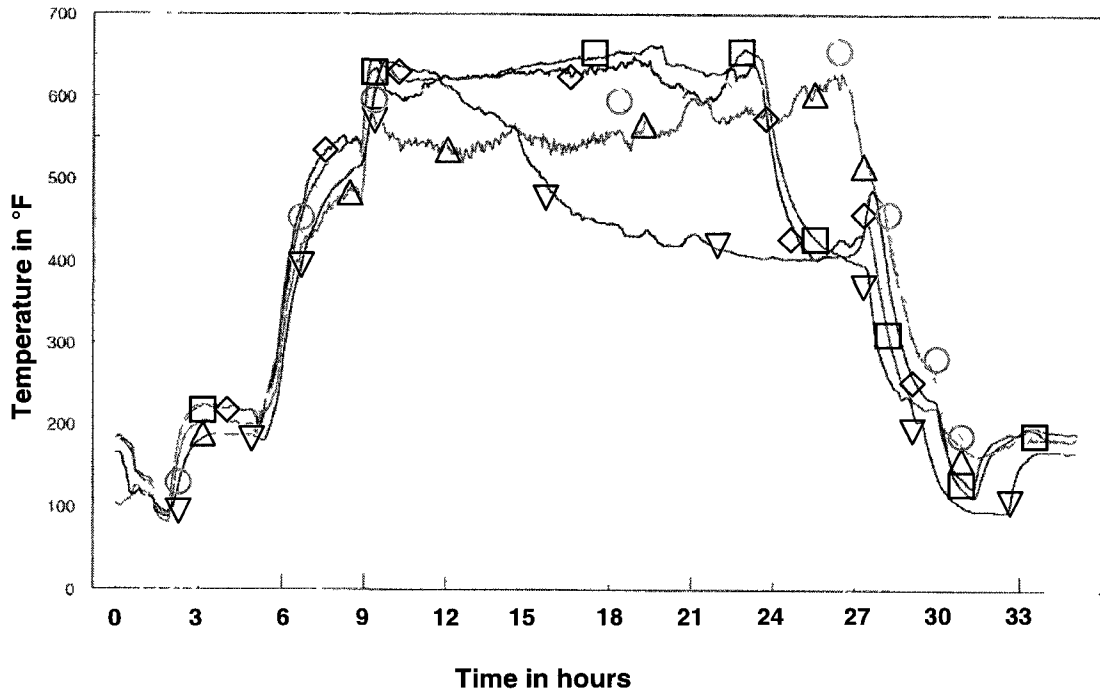
Superimposed on this nominal loading, are varying loads that are described as local deviation loads. Deviation loads are those loads occurring attributable to the nature of the drum fill operation. At the beginning of the fill cycle, the drum is empty. The introduction of steam and vapour occur under drum-empty conditions. It can be seen from Fig 5.1 that the response of the thermocouples is uniform and within $\pm 25\text{ F}^{\circ}$ [13.9 C°] at start of steam heat and diverging to $\pm 50\text{ F}^{\circ}$ [27.8 C°] at end of vapour heat.

As bitumen fill begins, the temperature spread is initially maintained but then begins to increase as the cylindrical portion of the vessel is reached and coke residual material accumulates. At that time, the skirt thermocouple temperature is seen to decline as the insulating effect of the coke begins to influence shell wall temperatures. As coke level continues to rise, the readings from the two lower thermocouples are seen to decline. At initiation of water quench, a relatively rapid fall in shell wall thermocouple readings initially takes place and is then seen to be discontinuous, with both temperature increases and holds occurring.

While the nominal features of this profile repeat cycle to cycle, the exact profile does not appear to repeat given the inherent variability of the operation. A complete definition of shell loading for the operating history of a coke drum needs to account for load type, and spatial and time descriptions for the nominal and local deviation loads. Conceptually, total load history TL is comprised of various nominal loads, L_i and local deviation loads, D_i occurring over all locations in the drum volume over the operating period or briefly, $TL = \sum [L_i(x, y, z, t) + D_i(x, y, z, t)]$. The data, as that depicted in Figure 5.1 indicates that the water quench stage of coker drum operation presents the most complex and variable loading imposed on the shell structure and provides the motivation to focus on the thermal loading of the coker drum for this thesis.

Knowledge of local loads is necessary in order to ascertain the impact on strains and stresses in the vessel shell. While specific loads, such as pressure and dead and live weight act on the structure to cause general strains and stresses, temperature loads will act locally and create additional strains and stresses important for evaluation of fatigue susceptibility. Note that pressure loads can also, due to drum geometric deviations cause local stress increments.

Figure 5.1 Vessel Shell Temperatures during Operational Cycle in °F [8]



Notes to Figure 5.1

1. Ordinate in degrees F

2. Legend

					
Location	CS 4	CS4	CS5	CS5	skirt

CS 4 \equiv thermocouple pair at shell course 4, 180 ° apart on east – west bearing

CS 5 \equiv thermocouple pair at shell course 5, 180 ° apart on north – south bearing

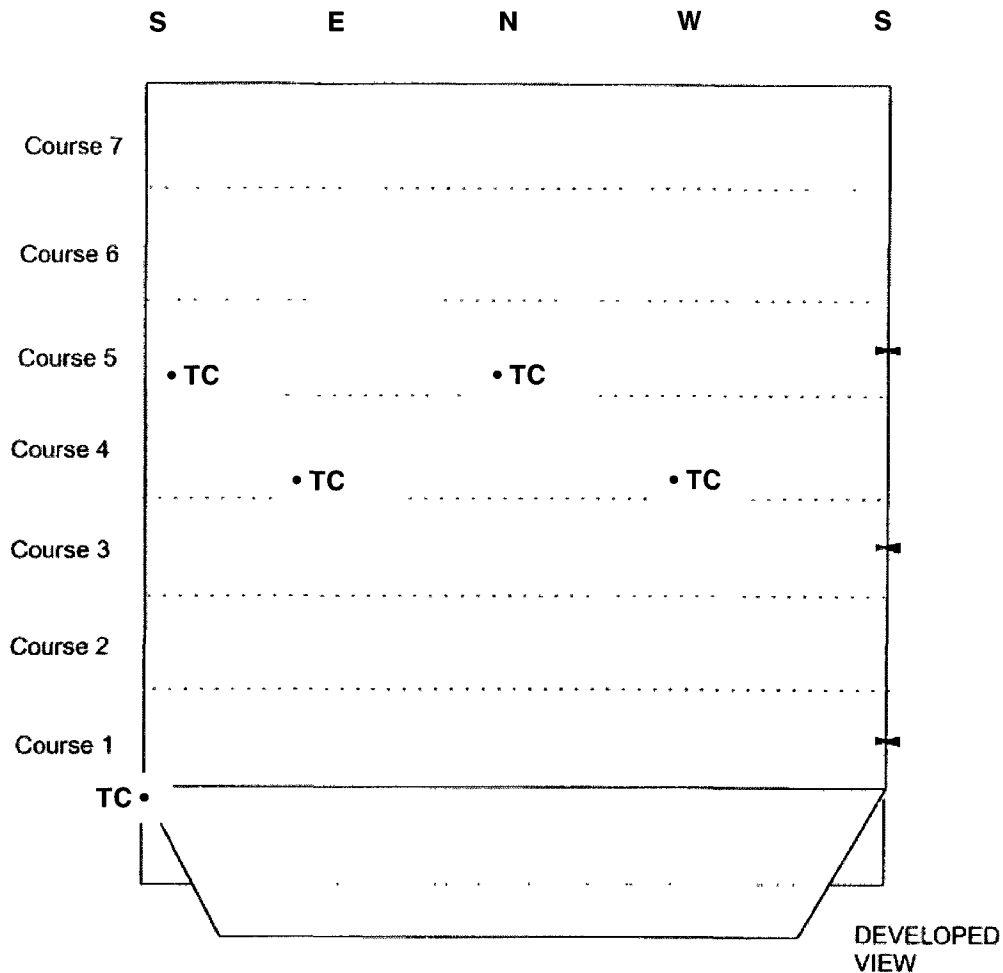
skirt \equiv thermocouple at skirt

3. Location CS 4 is at approximately 30'-10" feet [9398 mm] from the bottom of the drum cylinder section, location CS 5 is approximately 40'-10" feet [12446 mm] from the bottom of the drum cylinder section

4. The skirt location thermocouple is at the bottom of the cylinder section, with unknown bearing.

5. The location of the thermocouples is illustrated in Figure 5.2 for clarification.

Figure 5.2 Schematic Locations of Thermocouples [8]



Notes to Figure 5.2

1. TC \equiv location of thermocouple [5 locations, total]
2. Developed view of a coke drum cylinder, bottom cone and skirt section illustrating thermocouple locations. Not shown is the top head closure and remainder of bottom cone and closure.

These load situations can be damaging and are recognized by industry code design standards used for the design and fabrication of more critical equipment and are therefore codified in documents such as ASME VIII Division 2 [44] and ASME III [45].

5.2 Heat Transfer Modes

From Figure 5.1, it can be seen that as the steam test begins the drum shell and skirt thermocouples register a temperature increase with a reading lag at the skirt thermocouple. Shell course 4 and 5 appear to rise simultaneously. A steady state condition is reached between hours 3 and 6 as the steam testing procedure is completed. At hour 6, vapor heating commences with a near uniform rise to a temperature of 550 °F [288 °C] as indicated by the thermocouples. One of the CS5 thermocouples lags the other 3 thermocouples by a temperature difference of 100 F° [56 C°].

During this sequence, the energy transfer between the low alloy steel drum shell and the heating fluids takes place by a combination of several modes, these being

- convection
- radiation
- surface condensation

Then, as bitumen oil is introduced, disengagement between vapour and liquid occurs generating a high temperature vapour. As seen in Figure 5.1, shell courses 4 and 5 show a near immediate rise in temperature although the thermocouples are located in the upper elevations of the drum. Accordingly, the energy transfer mechanisms are likely as before, namely, convection, radiation and surface condensation.

As the bitumen level rises past the skirt elevation, a down trend in temperatures is noted. Heat transfer occurs by conduction between the bitumen / coke liquid-solid mixture. As the coke solidifies, it begins to act as an insulator. This effect is repeated as the bitumen level rises past the thermocouples at shell course 4. A decrease in temperature is noted at about hour 27. The lapsed time from start of oil in at hour 9 and completion at hour 27 is 18 hours and corresponds to the scheduled fill period. The nominal fill rate is simply calculated as $\sim 1/2$ inch per minute. This agrees with the ~ 4 hour delay exhibited by the temperature indication between shell course 4 and 5.

At completion of fill, steam is initially introduced and then water. There appears to be no discernible indication that steam has any influence on the temperature profile. As water quenching continues, the gradient for shell course 5 appears consistent with the gradient indicated for shell course 4 except for an up-spike in the temperature profile for shell course 4 halfway through the period of temperature decline. The gradient prior to oil in appears similar to the gradient during the water quench stage. However, the likely heat transfer modes that contribute to cooling during water quench are [46]

- convection
- conduction
- surface boiling

It should be noted that water quenching does not occur uniformly through the coke bed and is a source of operational difficulty. Flow channeling can result in “hot spots” and steam eruptions, termed geysering, during subsequent coke cutting [12]. The hot spots cause non-uniform temperature distributions. It is plausible that the increase in drum shell temperatures could occur if water flow becomes impeded to a local region.

To minimize flow channeling, a proof quench procedure is employed, for some units, which injects an initial high rate of quench water for a very short period of time, some 10 minutes for the purpose of preventing coking of existing flow channels in the coke mass. This procedure is based on operator preference and experience. The reasoning for this procedural step is thought to be that immediate injection of a large amount of water will cause flashing of the water to steam, creating a high velocity steam mass that will purge remaining liquid from the multiple flow channels in the residual coke mass and thus preserve the channels for subsequent water fill. Not all plant operators use this step as it has not been found to be generally effective.

The water quench step is scheduled for 3 hours followed by a ½ hour soak period. Water is then drained from the vessel and the vessel is depressured and opened to atmosphere for decoking. The nominal fill rate is approximately 2¾" per minute [70 mm per minute].

Since "hot" spots are cited as a probable explanation for the temperature spiking evidenced in Figure 5.1, it is equally reasonable to consider the formation of "cold" spots, wherein quench water is able to contact the shell at some locations and not others due to the distribution of internal flow channels in the residual coke mass.

Variations occur when the operational step timing is modified to meet production requirements. It is not unusual for deviations to occur during any of the listed operational steps. To recover schedule, portions of the sequencing are altered. A common procedural deviation is to truncate the vapor heating step or occasionally even forego this step entirely and introduce feed into the drum at completion of the steam test. Variations occur also because the flow channels developed during oil fill are not controlled nor do they likely develop identically from cycle to cycle due to the localized aspects of the process.

5.2.1 Calculation of Heat Transfer Coefficients

Values for thermal conductivity are included in Table 4.1. Heat transfer coefficients are estimated for the forced convection, surface condensation and surface boiling convection occurring during the operational steps.

Surface condensation is expected to be the dominant heat transfer mechanism during steam testing and initial warm up. The steam vapour is at a higher temperature than the vessel walls causing condensation to occur. A continuous flow of liquid occurs at the shell wall surface and the condensate flows downward under the influence of gravity. Kreith [46] states that the rate of heat flow depends primarily on the thickness of the condensate film unless vapor velocity is high or the liquid film is thick. The film becomes thicker from top to bottom. The unit surface conductance is given as

$$\bar{h}_c = 0.943 \left[\frac{\rho_\ell (\rho_\ell - \rho_v) g \cdot h'_{fg} \cdot k^3}{\nu_\ell L (T_{sv} - T_s)} \right]^{\frac{1}{4}} \text{ for } \underline{\text{average surface conductance over } L.} \quad [5.1]$$

Where,

- $\bar{h}_c \equiv$ average surface conductance
- $\rho_\ell, \rho_v \equiv$ density of liquid and vapour fractions
- $h'_{fg} \equiv$ latent heat of vaporization
- $\nu_\ell \equiv$ viscosity of liquid
- $k \equiv$ thermal conductivity of condensate
- $T_{sv}, T_s \equiv$ temperatures of saturated vapour, surface respectively
- $L \equiv$ total height of surface
- $g \equiv$ gravitational acceleration,

with all terms in consistent units.

As a function of distance from the top of the film - x , the local surface conductance is

$$\bar{h}_x = 0.943 \left[\frac{\rho_\ell (\rho_\ell - \rho_v) g \cdot h_{fg} \cdot k^3}{4 \cdot \nu_\ell \cdot x \cdot (T_{sv} - T_s)} \right]^{\frac{1}{4}} \quad [5.2]$$

Where, symbols are as given above, and

$\bar{h}_x \equiv$ local unit surface conductance
 $x \equiv$ distance from top of condensate film

Similarly, during the vapor heat step, the incoming oil vapours will condense on the drum shell due to the relative temperature differences between incoming vapour stream and shell wall. Similarly, introduction of reduced bitumen feed will also result in surface condensation.

Table 5.1 summarizes the average and local heat transfer unit surface conductances during vapour and bitumen feed in and steam heating steps for various film heights that may likely occur. The conductances are calculated on the basis of nominal fluid properties of the petroleum residuum feedstock for the delayed coker unit, using equations 5.2 and 5.3 [8, 46].

Table 5.1 Surface Condensation Conductances

Height of Film [feet]	Vapour [Btu / hr - ft ² - °F]	Steam	Height of Film [m]	Vapour [W / m ² - °C]	Steam
0.1	146.1	873.7	0.03	828.4	4,953.9
0.5	97.7	584.3	0.15	554.0	3,313.0
1	82.2	491.3	0.31	466.1	2,785.7
2	69.1	413.1	0.61	391.8	2,342.3
5	54.9	328.6	1.52	311.3	1,863.2
10	46.2	276.3	3.05	262.0	1,566.6
20	38.8	232.3	6.10	220.0	1,317.1
50	30.9	184.8	15.24	175.2	1,047.8
Average for 52'	43.3	258.7	Average for 15.8 m	245.5	1,466.8

The table indicates that very high heat transfer rates occur at the top of the film height where film thickness is small. These heat transfer rates have not been directly measured but do provide plausible explanation as to shell temperature rise occurring near simultaneously at the various drum elevations.

During water quench, water is slowly injected into the hot coke bed initially and then the rate is increased in order to minimize the quench time. At this time, the coke drum shell temperature varies between 400 °F [204 °C] in the lower sections and 650 °F [343 °C] in the upper sections, as shown in Figure 5.1. Local boiling of the water in the vicinity of the surface occurs even when the bulk temperature of the water is below its boiling point. The boiling process in a liquid with bulk temperature below the saturation temperature but whose boundary layer is sufficiently superheated that bubbles form next to the heating surface is called heat transfer to a subcooled boiling liquid or surface boiling.

Kreith [46] gives an expression for determining the value of the heat flux. The heat flux will vary by the excess temperature above boiling or simply termed, excess temperature, ΔT_x . The expression, in consistent units, is:

$$\frac{q}{A} = \left[\frac{c_\ell \cdot \Delta T_x}{h_{fg} \cdot \text{Pr}_l^{1/7}} \cdot \frac{1}{C_{sf}} \right]^3 \cdot \frac{\nu \cdot h_{fg}}{\sqrt{\frac{\sigma}{\rho_\ell - \rho_v}}} \quad [5.3]$$

$\frac{q}{A} \equiv$ average surface heat flux

$\rho_\ell, \rho_v \equiv$ density of saturated liquid and vapour fractions

$h_{fg} \equiv$ latent heat of vaporization

$\nu \equiv$ viscosity of liquid

$\sigma \equiv$ surface tension of the liquid-to-vapour interface

$\Delta T_x \equiv$ temperature difference between saturated vapour and surface

$C_{sf} \equiv$ empirical constant which depends upon the nature of the heating surface-fluid combination and whose numerical value varies from system to system

$c_l \equiv$ specific heat of saturate liquid

$\text{Pr}_l \equiv$ Prandtl number of the saturated liquid

Table 5.2 Surface Boiling Conductance by Equation 5.3

ΔT_x [F°]	Flux [Btu / hr - ft ²]	Conductance [Btu / hr - ft ² - °F]	ΔT_x [C°]	Flux [W / m ²]	Conductance [W / m ² - °C]
10	0.5	0.0	5.6	1.6	0.0
50	66.4	1.3	27.8	209	7.4
100	530.9	5.3	55.6	1,673	30.1
200	4,247.2	21.2	111.1	13,387	120.2
300	14,334.2	47.8	166.7	45,181	271.0
400	33,777.5	84.9	222.2	106,466	481.4
500	66,362.2	132.7	277.8	209,174	752.4
600	114,674.0	191.1	333.3	361,452	1,083.5
700	182,098.0	260.1	388.9	573,973	1,474.8

Table 5.2 summarizes values using equation [5.3]. From Table 5.1, the surface condensation conductance varies between a maximum of 146.1 Btu / hr - ft² - °F [828.4 W / m² - °C] / to a minimum of 30.9 Btu / hr - ft² - °F [175.2 W / m² - °C]. Similarly, the surface boiling conductance for the specifics of coke drum operation, varies from a maximum of 161.9 Btu / hr - ft² - °F [918.0 W / m² - °C] to a minimum 13.3 Btu / hr - ft² - °F [75.4 W / m² - °C]. The selection of these values for comparison is explained as follows.

The surface condensation conductances are calculated on the basis of vapour temperatures of 550 °F [287.8 °C] and shell temperatures of 250 °F [121 °C] forming a surface film over a height of some 50 feet [15.24 m].

The values selected for the surface boiling conductance represent the range of calculated conductance values caused by water at approximately 250 °F [121 °C] contacting hot metal at 800 °F [427 °C], resulting in a calculated surface conductance of 161.9 Btu / hr - ft² - °F [918.0 W / m² - °C]. Water at 250 °F [121 °C] contacting hot metal at 400 °F [149 °C] results in a calculated surface conductance of 13.3 Btu / hr - ft² - °F [75.4 W / m² - °C]. Consequently, temperature profiles should be nominally similar for heat up and cooldown phases.

Referring to Figure 5.1 indicates that the temperature rise during steam test and vapour heat, i.e. at start of operation, has an up-gradient similar in magnitude to the down-gradient during water quench, i.e. at end of operation. A value of 800 °F [427 °C] was taken as the upper limit since many coke drums operate with this temperature as an upper limit, in comparison to the particular data presented in Figure 5.1. There was also a question of data accuracy due to experimental error as discussed later, which motivated using the higher value for parts of the analyses.

In general, high heat transfer rates are expected to be uniform throughout the coke drum during steam, vapor and oil in heat up. Higher heat transfer rates are ordinarily expected in the lower vessel zones during the water quench phase where a combination of free water and high temperature in the coke residual and shell are present. High heat transfer rates are not expected in the upper shell since superheated steam would only be expected to be present here. However, if geysering occurs due to obstructed and re-directed or confined flow channels, then very high heat transfer rates would be induced as subcooled liquid contacts the high temperature shell in either lower or upper portions of the coke drum.

Ramos et al. [15] have measured this effect and show that cooling is non-uniform. Their data indicate portions of the vessel being 400 F° [222 C°] cooler than the surrounding shell. This uneven cooling was described as random in location and magnitude and not repeating cycle to cycle.

There is high sensitivity in the calculation to the surface-fluid combination parameter C_{sf} . An increase of an order of magnitude in the surface heat conductance rate occurs by reducing the value of C_{sf} by $\frac{1}{2}$.

Referring to Figure 5.1, it can be seen that the CS4 thermocouple readings do not continuously decrease but rather, a temperature spike can be noted approximately half way through the quench phase, at about hour 27. This is a clear indication that cooling does not proceed uniformly in both elevation and, very likely, circumferential directions, and could be attributable to the geysering effect.

The Coker drum shell temperature is governed by heat transfer from the various process streams flowing into the coke drum as operation is sequenced through the steps listed in Table 1.3. Figure 5.1 provides data to postulate an initial qualitative characterization of temperature loading and is summarized in Table 5.3.

Table 5.3 Loading Characterization for Coke Drum Shell

Step	start of step	intermediate	end of step
steam test	linear ramp, increasing	linear ramp, increasing	constant
vapor heat	linear ramp, increasing	linear ramp, increasing	linear ramp, increasing
oil in	linear ramp, increasing	constant	constant
quench	linear ramp, decreasing	linear ramp, decreasing	constant

Notes to Table 5.3

1. *Definition of qualitative nature of loading step*
 - start of step \equiv the initial, approximate $\frac{1}{3}$ portion of loading step or primarily transient portion at start of step
 - intermediate \equiv the middle $\frac{1}{3}$ portion or primarily steady state portion of loading step
 - end of step \equiv the concluding $\frac{1}{3}$ portion or primarily transient portion at end of step

The above definitions are qualitative and are meant to conveniently and briefly characterize the multiple steps of the coke drum cycle without becoming unnecessarily detailed

Determination of heat transfer coefficients using analytical methods will bound the heat transfer coefficients heuristically derived using the measured data similar to the data of Figure 5.1 and used in the thermal finite element analytical work.

5.3 Establishing Heat Transfer Coefficients by Thermal FEA

A thermal FEA was used to better determine the heat transfer rates suggested by the analytical expressions available in the literature. Whereas application of these expressions requires knowledge of the relevant physical properties of the fluid streams, the use of a heuristic approach by means of FEA is not reliant on detailed knowledge of these properties but rather requires only modification of a trial value over a period of time to match measured values.

The thermal FEA model can be extensive, modeling the entire coke drum structure or compact, and modeling only a small portion of the overall structure. Figure 5.1 clearly shows that thermal loading behaves in a global manner since the thermocouples installed on this specific coke drum respond somewhat uniformly with relatively small differences in temperature although these thermocouples are at relatively large distances from each other. Referring to Figure 5.2, the two thermocouples at shell course CS 5 are apart 180° in circumference and approximately ten feet [3.05 m] in elevation from the two thermocouples at shell course CS 4, which are also 180° apart and offset 90° from the CS 5 thermocouples. The thermocouples at shell course CS 4 are forty feet [12.2 m] in elevation from the skirt thermocouple. As can be seen in Figure 5.1, the thermocouples react simultaneously at specific triggers in the loading sequence and deviate at other specific times. For example, at both steam test and vapour heat, the thermocouples are seen to rise, more or less, at the same time and at the same rate.

Larger deviations occur during the “oil in” step and secondly, during the water quench step. At “oil in”, those portions of the drum shell above the oil and coke level are seen to respond, again more or less, uniformly. As the oil / coke residual level reaches a particular height, the thermocouple begins to track differently. For example, the skirt thermocouple of Figure 5.1 indicates a declining temperature as the coke residual level passes the thermocouple elevation. The thermocouples at elevations CS4 and CS5 track uniformly until the thermocouples at elevation CS4 are seen to fall off as the coke residual level reaches this elevation. The time interval between thermocouple readings at elevation CS4 and CS5 matches the volumetric flow rates and time schedule. Several general observations can be stated

- heat transfer is global in the “clean and empty” vessel condition
- heat transfer is global for the shell sections above the oil / coke residual level
- as coke residual level reaches a particular elevation, the heat transfer rate declines for the elevation below the coke residual level due to the insulating effect attributed to the coke residual
- heat transfer during water quench is also broadly uniform suggesting that the coke is generally porous
- anomalies in the temperature response of the shell thermocouples suggests that local effects take place during the water quench step and strongly influence local heat transfer rates

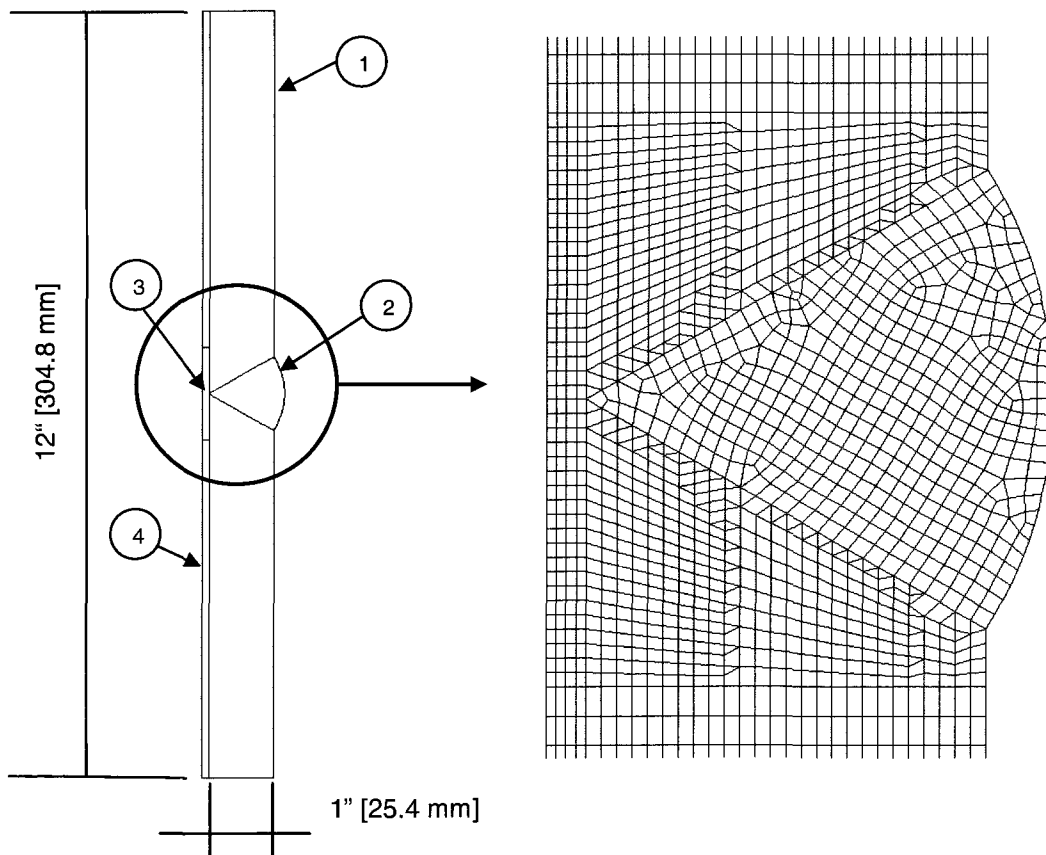
It is apparent that the dominant heat transfer modes are primarily convection and conduction attributable to the cooling coke mass residual. The convective and conduction heat transfer may be combined using an overall heat transfer coefficient [46]. Due to the generally symmetric action, the use of an axisymmetric thermal model will establish the nominal heat transfer coefficients during various operational steps. The thermal FEA model is shown in Figure 5.3. The model is constrained against heat loss along its bottom and top edges. The heat loss by conduction heat transfer through the insulating layer encapsulating the coke drum shell and to the environment via free convection is modeled using a single combined heat transfer co-efficient as the temperature gradient through the insulation is not of interest. The internal heat transfer coefficient is adjusted to match the specific operational step by adjusting its value so that the resulting shell temperature matches the measured temperature. The coefficients of conduction for the clad and base material are entered as temperature dependant values due to their variation over the temperature of interest [refer to Table 4.1]. In order to preserve computational resources, long steady state portions of the operating cycle are not modeled. The experimental data is limited in that only five thermocouples were located at relatively large distances from each other precluding determination of adequately accurate temperature gradients along the surface. The data is sufficient to support determination of the through-thickness temperature gradient.

It was deemed as not essential to match exactly the calculated profile to the measured profile since it has already been established that the operation of the unit is highly variable for a number of reasons, including

- operator intervention
- stream parameters are not rigorously controlled
- equipment troubles
- variable formation of coke residual mass causing geysering, blockage
- non-unique profile

The primary motivation was to establish a practical model that approximated the nominal temperature response of the coke drum shell to obtain a reasonable characterization of the through-thickness temperature profile. It would not be purposeful to duplicate exactly the measured response of Figure 5.1 since this specific loading profile is unique. This specific loading profile also may not be particularly severe. The primary learnings, at this time, are in being able to establish reasonably matching heat transfer rates and to obtain a first pass indication of impact upon stresses being generated in a section of the shell by temperature loading. The output of the thermal FEA is a through-thickness temperature profile of the shell which will be the input to the mechanical stress FEA model.

Figure 5.3 Thermal FEA Model at Circumferential Weld



Notes to Figure 5.3

1. Model element is a 2D axisymmetric element for thermal problems
2. The base material thickness is taken as 1" [25 mm] thick, clad liner is 0.100" [2.54 mm] thick
3. Four distinct metallurgical and geometric areas are modeled, 1 – base material, 2 – base material weld, 3 – clad restoration weld, 4 – clad liner
4. Heat transfer coefficient applied at exterior surface of the model is 2.70 Btu / hr – ft² – °F [15.31 W / m² – °C] since this surface is insulated for purposes of minimizing heat loss and protection of operating personnel.
5. Heat transfer from top and bottom surfaces is nil
6. No resistance to heat transfer occurs across material boundaries
7. Heat transfer coefficients applied at the interior surface of the model are the heuristically determined values given in Table 5.4.
8. Accelerated heat transfer coefficients at ID surface during water quench are an order of magnitude larger than corresponding coefficients applied under nominal temperature loading

Four distinct metallurgical zones were geometrically modeled; however, the thermal properties for base material and base material weld were taken as identical per industry references. [10]

The external insulation was not modeled for efficiency. An equivalent heat transfer coefficient, representing conduction through the insulation and convective heat transfer from the exterior surface from the insulation to the surrounding environment, was determined using accepted methods.

The results of the temperature matching are shown in Table 5.4. The calculated heat transfer coefficients, [HTC] are shown against those values published in the literature. The best matching occurs for vapour heating where a calculated value of 11.2 Btu / hr – ft² – °F [63.5 W / m² – °C] was obtained versus the literature reference value of 9.1 Btu / hr – ft² – °F [51.6 W / m² – °C]. The analytical prediction was determined in Table 5.1 to range from 30.9 to 146.1 Btu / hr – ft² – °F [175.2 to 828.4 W / m² – °C]. The heuristically derived HTC is much less than the analytically determined value but reconcilable on the basis that surface cleanliness in the actual equipment is much less in comparison to the calculation in which none of the parameters accounts for surface cleanliness.

Table 5.4 Temperature Ramp Matching to Determine Heat Transfer Coefficients

Operating Step	ΔT [°F]	Calculated		Literature Reference	
		$\Delta T / t$ [°F/min]	HTC [Btu/ft ² -hr- °F]	HTC [47] [Btu/ft ² -hr- °F]	HTC [17] [Btu/ft ² -hr- °F]
Steam Test	100 – 240	5.7	19.7	35.3	-
Vapor Heat	240 – 530	15.4	11.2	7.0 ~ 9.1	2.16
Oil in	530 – 650	7.5	14.8	4.5	43.2
Quench – initial	650 – 450	- 8.8	12.8	22.0	43.2
Quench – final	450 – 100	- 8.8	18.8	183.3	4.32

Notes to Table 5.4

1. $\Delta T \equiv$ temperature in shell metal from start to end of step interval
2. $\Delta T / t \equiv$ maximum temperature increment measured during step from Figure 5.1
3. See Table 5.4M for SI units

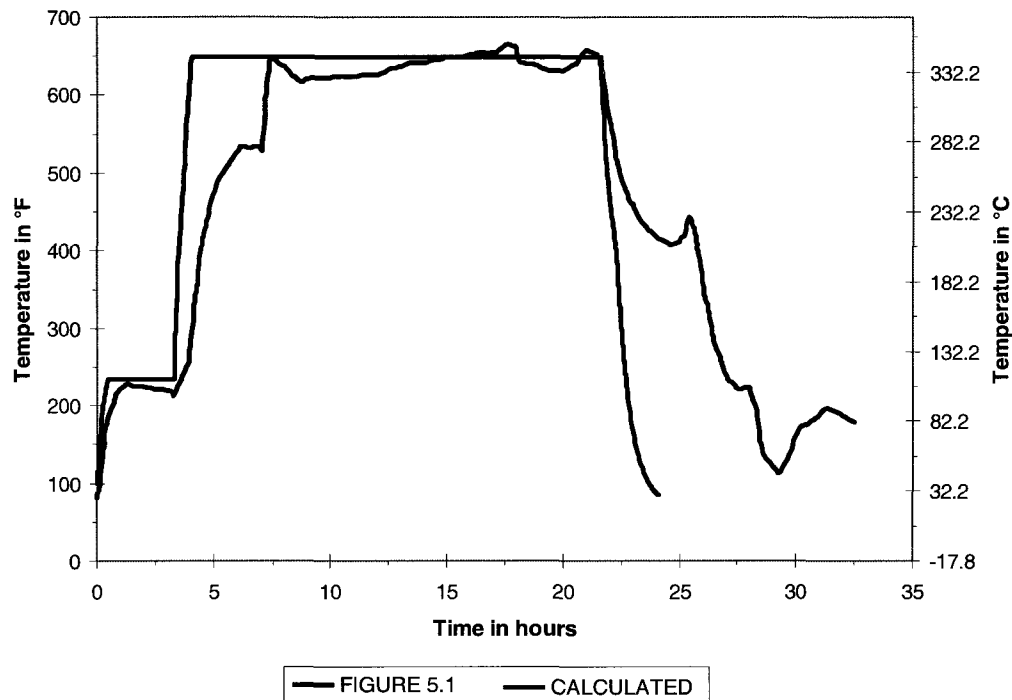
For the quench step, a value range of 12.8 to 18.8 Btu / hr – ft² – °F [72.6 to 106.6 W / m² – °C] was derived heuristically, while the analytically derived range of values determined in Table 5.2 is between 13.3 to 161.9 Btu / hr–ft²–°F [75.4 to 918.0 W / m² – °C]. There is matching at the lower end which presumes an excess temperature, ΔT_x of 150 F°, i.e. metal temperature of 400 °F and quench-water temperature of 250 °F.

From Figure 5.1, it can be seen that the metal temperature at shell course location CS4 is at 400 °F at the time of quench water initiation and there is very good alignment between the analytically derived and the heuristically derived results. Equation [5.3] contains an empirical constant that accounts for the surface-fluid combination and presumably accounts for surface cleanliness.

As a result of this, it can be seen that the HTC value of 183.3 9 Btu / hr-ft²-°F [1,042.7 W / m² -°C] found in the literature is a plausible value under the appropriate conditions and demonstrates that HTC values may vary by an order of magnitude, all in alignment with the analytical review in paragraph 5.2.1 above. The calculated HTC values given in Table 5.4 differ by a factor of 1.75x which likely indicates that the very few thermocouples placed on the shell of the coke drum were insufficient to detect the likely extreme local variations in temperature. The work of Ramos [15] presented in paragraph 2.1.1 above attests to this. The reported values in Table 5.4 from reference [17] match poorly with the values derived in reference [47]. There is broad matching of the values found in [47] with the calculated HTC and analytically derived values.

The calculated HTC values were utilized for the thermal FEA analysis and plotted against the measure values of Figure 5.1 and shown in Figure 5.4. To make best use of computer resources, repetitive calculations for the steady state portions of the cycle are eliminated in the thermal FEA and this shows as a horizontal line in the figure. The focus of interest is on the transient portions of the thermal profile which will induce stresses related to temperature differences. As seen in Figure 5.4, the use of a single valued HTC for each step of the operating sequence is adequate and seemingly conservative with respect to the measured data.

Figure 5.4 Comparison of Calculated Temperatures to Measured



Notes to Figure 5.4

1. — FIGURE 5.1 \equiv measured shell metal temperature from Figure 5.1
2. — CALCULATED \equiv calculated shell metal temperature for complete cycle

As previously noted, the quench phase, especially when proofing is used, can result in highly variable conditions and the use of a more aggressive HTC may be required. Additional data indicate that extreme temperature change rates of 80 F° / min [44.5 C° / min][45] to in excess of 200 F° / min occur [111 C° / min][48] in comparison to the change rates indicated in Table 5.4 and depicted in Figure 5.4.

Table 5.4M Temperature Ramp Matching to Determine Heat Transfer Coefficients – SI Units

Operating Step	Calculated			Literature Reference	
	ΔT [°C]	$\Delta T / t$ [C° / min]	HTC [W / m ² - °K]	HTC [47] [W / m ² - °K]	HTC [17] [W / m ² - °K]
Steam Test	38 – 115	3.2	111.7	200.2	-
Vapor Heat	115 – 277	8.6	63.5	39.7 ~ 51.6	12.3
Oil in	277 – 343	4.2	83.9	25.5	245.0
Quench – initial	343 – 232	- 4.9	72.6	124.7	245.0
Quench – final	232 – 38	- 4.9	106.6	1039.3	24.5

CHAPTER 6 ANALYSIS – CLOSED FORM MODELS

6.1 Closed Form Models

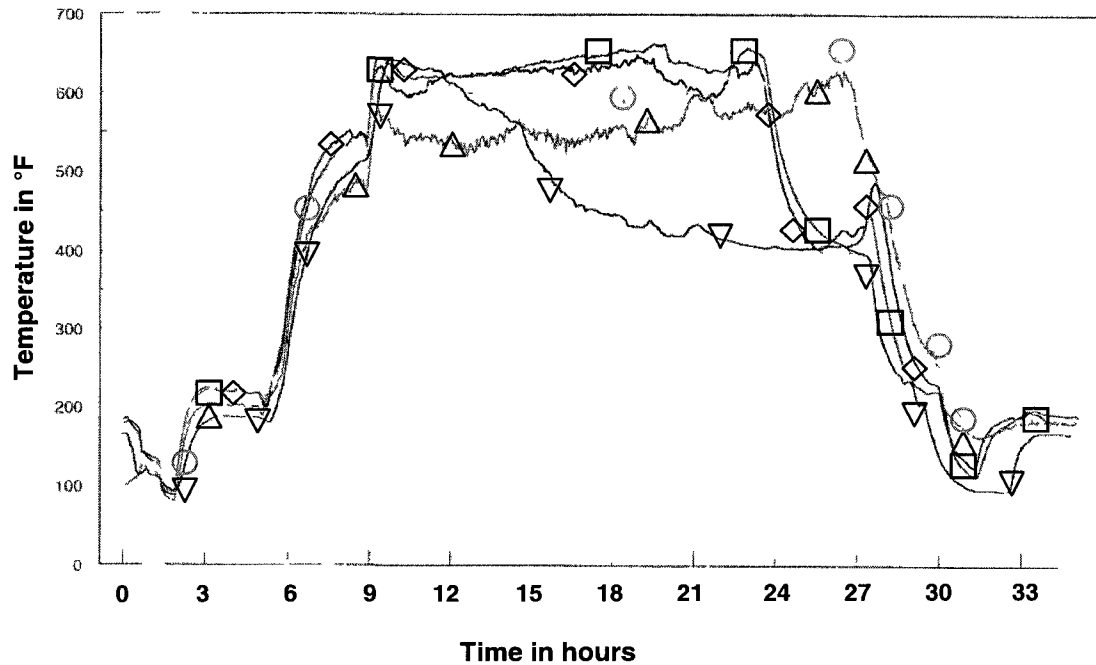
The analytical work available in the literature is limited and has not definitively identified the mechanisms leading to shell distortions and cracking of delayed coking drums. To analyze the coke drum involves a number of engineering concepts and their appropriate use:

- spectrum loading
- cycle counting
- nonzero mean strain
- cumulative fatigue damage
- stress and strain concentration

Figure 5.1 illustrates the shell temperature spectrum for a single cycle of operation of a coke drum from [8]. It is reprinted as Figure 6.1 for convenience. The spectrum is compared to Figure 6.2 illustrating the shell temperature plot for the same drum during a cycle several days later.

The two figures illustrate that cycle durations and temperature profiles can vary significantly. Temperatures at cycle start, during steam test are higher and held for an extended period, some 9 hours in Figure 6.2 compared to 3 hours in Figure 6.1. The water quench period in Figure 6.2 is also extended, from hour 30 to 42 versus from hour 24 to 30 in Figure 6.1. At hour 39 in Figure 6.2, all four shell thermocouples show a sudden and large spiking in temperature whereas Figure 6.1 shows a much smaller spiking by only 1 of the thermocouples.



Figure 6.1 Vessel Shell Temperatures during Operational Cycle in ° F [8]



Notes to Figure 6.1

1. Ordinate in degrees °F

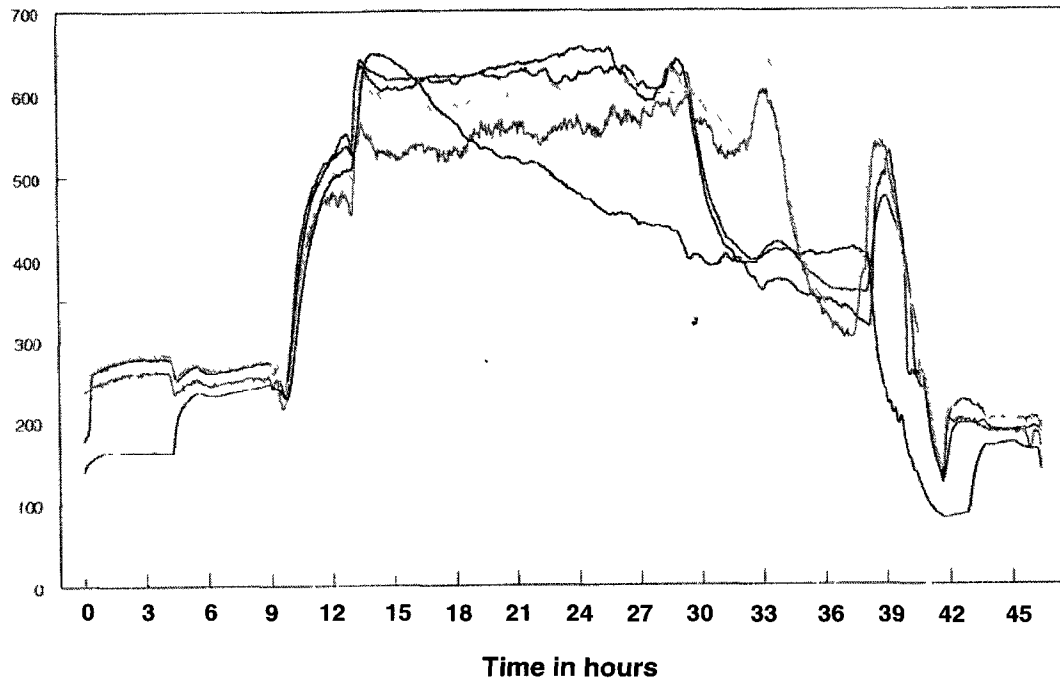
2. Legend

					
Location	CS 4	CS4	CS5	CS5	skirt

CS 4 ≡ thermocouple pair at shell course 4, 180 ° apart on east – west bearing
 CS 5 ≡ thermocouple pair at shell course 5, 180 ° apart on north – south bearing
 skirt ≡ thermocouple at skirt

3. See Figure 5.1 for additional notes

Figure 6.2 Vessel Shell Temperatures during Operational Cycle in °F [8]



Notes to Figure 6.2

1. Ordinate in degrees F

2. Legend

Location	CS 4	CS4	CS5	CS5	skirt
----------	------	-----	-----	-----	-------

Symbols not used since general trend is of interest, only.

3. See Figure 6.1 and Figure 5.1 for additional notes

Strain is simultaneously measured using gauges located coincident with the thermocouple locations given in Figure 5.2. The gauge mounted on the skirt is a single gauge arrangement. The shell mounted gauges are a two gauge arrangement; one gauge mounted circumferentially, the second gauge mounted axially. The assumption is that these gauges are mounted in the directions of principal stress.

The gauges are reported to be temperature compensated in order to provide a corrected strain calculation. It is not clear from the experimental reports as to what comprises the compensation. Correction is typically made to account for the change in resistivity of the gauge as temperature changes. In the case of the coke drums, a large amount of free thermal strain is experienced due to the change in temperature from ambient of approximately 100 °F [~37.8 °C] to operating temperatures of approximately 800 °F [~ 427 °C]. Note that the preceding figures indicate an apparent operating temperature of 650 °F [~ 343 °C] for the specific equipment tested.

The specific model of strain gauge used in the field measurement work is functional to 1,112 °F [600 °C] [8].

6.1.1 Stress and Strain Determination

The industry practice is to determine an equivalent stress value using the von Mises stress equivalent form, per [8, 20, 48, 49]:

$$S_{equiv}^2 = S_h^2 + S_a^2 - S_h \cdot S_a \quad [6.1]$$

where

$$S_h = \frac{E}{1-\nu^2} (e_h + \nu \cdot e_a) \quad [6.2]$$

$$S_a = \frac{E}{1-\nu^2} (e_a + \nu \cdot e_h) \quad [6.4]$$

and, an equivalent strain expression is used of the form,

$$e_{equiv} = \frac{1}{1-\nu^2} \left[(e_h - \nu \cdot e_a)^2 + (e_a - \nu \cdot e_h)^2 - (e_h - \nu \cdot e_a)(e_a - \nu \cdot e_h) \right]^{1/2} \quad [6.5]$$

[sic] where

$e_a \equiv$ principal mechanical strain in the axial direction of the drum

$e_h \equiv$ principal mechanical strain in the circumferential direction of the drum

It can be seen from the above that the expression for e_{equiv} is derived by

substitution of S_h and S_a into S_{equiv}^2 and taking $e_{equiv}^2 = \frac{S_{equiv}^2}{E^2}$ from which,

$$e_{equiv} = \frac{S_{equiv}}{E} = \frac{1}{1-\nu^2} \left[(e_h - \nu \cdot e_a)^2 + (e_a - \nu \cdot e_h)^2 - (e_h - \nu \cdot e_a)(e_a - \nu \cdot e_h) \right]^{1/2}$$

as given above in equation [6.5].

Following Rees [29], Hoffman and Sachs [31] and Salter [50], the von Mises equivalent stress is given as

$$\sigma_{equiv} = \frac{\sqrt{2}}{2} [(\sigma_1 - \sigma_2)^2 + (\sigma_2 - \sigma_3)^2 + (\sigma_3 - \sigma_1)^2]^{1/2} \quad [6.6]$$

where $\sigma_1, \sigma_2, \sigma_3$ are the principal stresses, from which, for a biaxial state of stress, i.e. $\sigma_3 = 0$;

$$\begin{aligned} \sigma_{equiv} &= \frac{\sqrt{2}}{2} [(\sigma_1 - \sigma_2)^2 + (\sigma_2 - 0)^2 + (0 - \sigma_1)^2]^{1/2} \\ &= \frac{\sqrt{2}}{2} [\sigma_1^2 - 2 \cdot \sigma_1 \cdot \sigma_2 + \sigma_2^2 + \sigma_2^2 + \sigma_1^2]^{1/2} \end{aligned}$$

$$\sigma_{equiv}^2 = \sigma_1^2 + \sigma_2^2 - \sigma_1 \cdot \sigma_2 \quad [6.7]$$

which is seen to be equivalent to equation [6.1] above.

Similarly, Hoffman and Sachs [31], and Salter [50] both cite an “effective strain” given by

$$e_{eff} = \frac{\sqrt{2}}{3} [(e_1 - e_2)^2 + (e_2 - e_3)^2 + (e_3 - e_1)^2]^{1/2} \quad [6.8]$$

in which, e_1, e_2, e_3 are the principal strains.

We can conclude the equivalent strain determination, equation [6.5] used by industry is inconsistent with the literature.

The literature shows that both a strain based approach [15] and a stress based approach [8, 18, 20, 51] are used for fatigue life determination, but the stress based approach being more popular.

The stress based approach calculates a maximum equivalent stress range for an operating cycle. The practice is to then use an industry recognized design publication such as ASME VIII Div 2 Code for Alternative Rules for Construction of Pressure Vessels [44] and compare results to design limits given therein. An undocumented practice has been to enter the design limits using a stress range value whereas the design criteria are based on the use of stress amplitude values [18, 51]. Since the range may be twice the amplitude, the effect is to build in conservatism which is justified on the basis of apparent effectiveness.

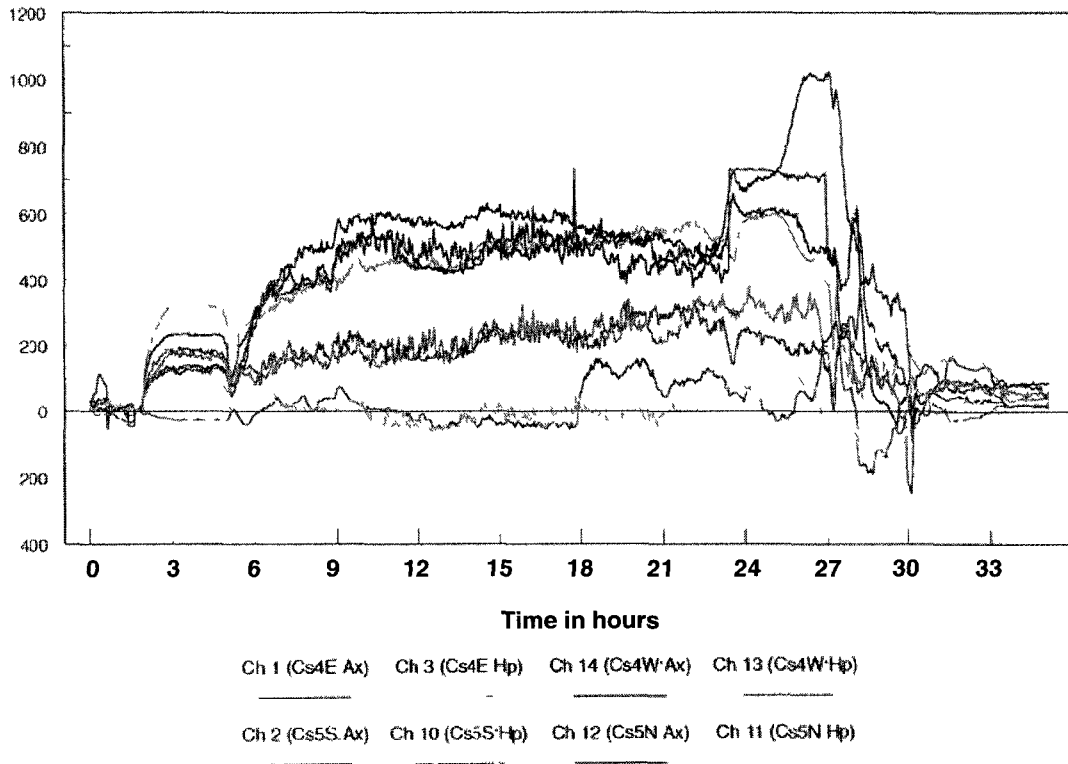
For the strain based approach, a maximum shell strain range is calculated based on the largest measured strain, $\max(e_j)$ less the smallest measured strain, $\min(e_j)$ measured at a point during an operating cycle [15], i.e.

$$\Delta e_j = \max(e_j) - \min(e_j) \quad [6.9]$$

Ramos et al. [14] developed low cycle $e - N$ life fatigue curves for base material, weld and HAZ for 1Cr – ½ Mo and 1¼ Cr – ½ Mo fabrications. The authors applied the data to failure of a skirt weld and demonstrated that failure was expected in two years. Follow-up publications showing application and efficacy for shell assessment were not found in the literature.

Inspection of the strain data are not consistent with the biaxial strain distributions expected during pressure and thermal loading. Under pressure loading, the biaxial strain distribution should approximate a 1:4 ratio for longitudinal to hoop directions for a value of Poisson's ratio of 1/3. The strain ratio is dependant on the exact value of Poisson's ratio. Under thermal loading, the biaxial strain distribution should approximate, since clad construction is present, a 1:1 ratio for longitudinal to hoop directions. Strain distributions for two different cycles of operation are given in Figure 6.3 and Figure 6.4.

Figure 6.3 Vessel Shell Principal Strains for an Operational Cycle in ue [8]



Notes to Figure 6.3

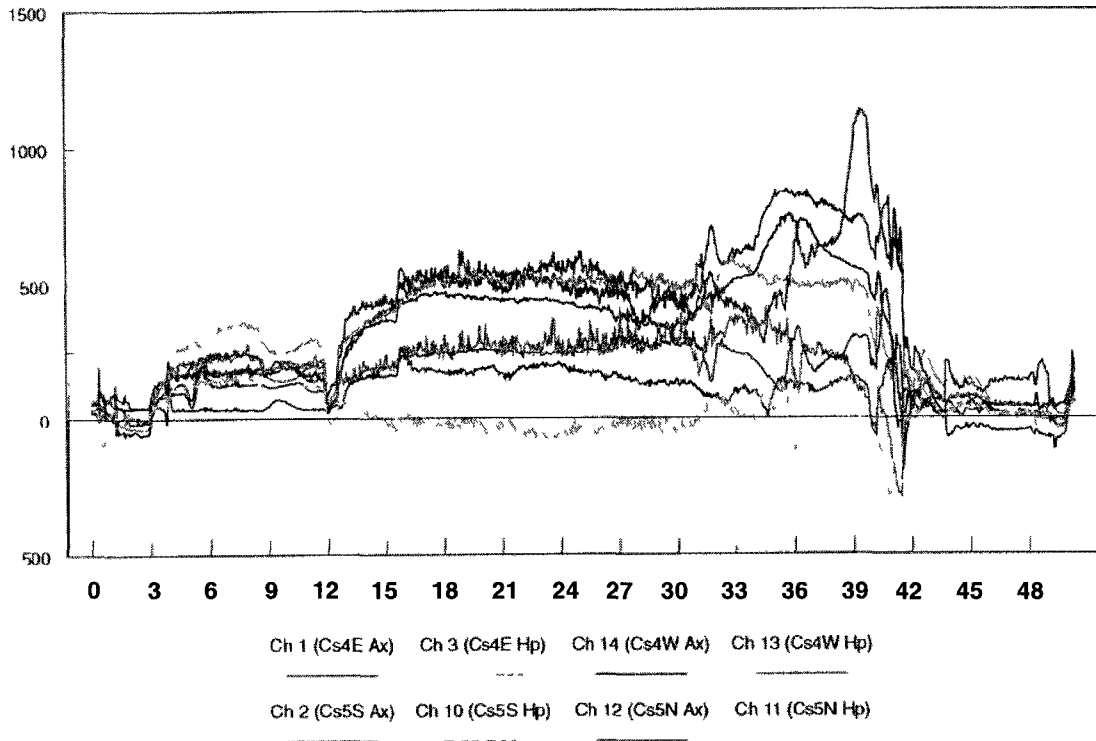
1. Abscissa indicates time in hours, ordinate indicates strain in microstrain [ue]
2. Abscissa is more or less coincident with Figure 6.1 and Figure 6.2
3. Strains are assumed to be total strains given the lack of specifics in the data.

Figures 6.3 and 6.4 display a number of trends, some of which are consistent with expectations while others are not.

The observations that are in accordance with expectations are:

1. There is a strain increment to approximately 200 to 250 ue [microstrain] on pressurization to 35 psig [241 kPag] in a drum diameter of 312 inch [7924 mm] and 1 " thick [25.4 mm] shell thickness. However, note that only some of the strain gauge readings reached this value during the steam test step [between hours 3 to 6 in Figure 6.3 and hours 3 to 12 in Figure 6.4].

Figure 6.4 Vessel Shell Principal Strains for an Operational Cycle in ue [8]



Notes to Figure 6.4

1. Abscissa indicates time in hours, ordinate indicates strain in microstrain [ue]
 2. Abscissa is more or less coincident with Figure 6.1 and Figure 6.2
2. In Figure 6.3, channel pair Ch 11 and Ch 12 do not show any strain increase during temperature rise which could be taken to be indicative of the expected behaviour of strain gauges to thermal strain. As indicated previously, the pressure vessel shell, remote from constraints, is free to expand during temperature loading. However, the strain readings of Ch 11 and Ch 12 are not consistent with the other gauges where increasing strain is indicated and ratios deviate substantially from a 1:1 ratio, especially channel pairs Ch 2 and Ch 10 and, pair Ch 13 and Ch 14.

-
3. There is thermal strain increments during temperature rise associated with steam, vapor and oil-in heat up for some of the strain gauges. The maximum temperature is about 650 °F according to the data of Figure 5.1 accounting for an approximate simple strain of 425 ue. Half of the strain gauges readings in each of Figure 6.3 and Figure 6.4 reach this value.
 4. Incoming oil and water quench flows enter the coke drum by means of a single nozzle entry at the bottom of the vessel. As a result, the flow distribution is uncontrolled and results in flow channeling and irregular contact of quench water with the coke drum shell. As a consequence, variability occurs in the temperature response at the drum wall during the water quench step resulting in variable strains being measured. This is clearly evident during the quench steps in Figure 6.3 [hours 24 to 30] and Figure 6.4 [hours 30 to 42].

The observations that are not in accordance with expectations are:

1. There are strain increments during temperature rise associated with steam, vapor and oil-in heat up. Since thermal growth is not restricted, no mechanical strain should exhibit or should show a slight negative strain due to the effect of cladding which has a lower coefficient of expansion than base material [Refer to Table 4.1]. Therefore, the strain data provided by the strain gauges is seen to measure total strain rather than mechanical strain.

-
2. The strain increments during water quench are expected and should range up to a mechanical strain of 3,000 ue based on a maximum temperature differential of 450 F° [250 C°] between shell temperature and incoming water temperature. Temperature exposure at any specific location may create either a “cold spot” or “hot spot” resulting in tensile or compressive strains, respectively suggesting an even larger strain range is possible and further detailed later in this work. The exhibited strain differences show approximately as 1,500 ue.
 3. The strain ratios between hoop and longitudinal directions are not uniformly consistent with pressure and thermal loading fields. The strain readings in Figure 6.3 were discussed above. The strain readings in Figure 6.4 are also somewhat in accordance with expectations for the steam test portion which is governed by pressure loading where hoop strain readings exhibit greater than axial strain readings. During the oil in portion, governed by temperature loading, seven of eight strain readings increase and deviate from the expected 1:1 ratio expected for temperature loading.

6.1.2 Damage Accumulation Determination

The stresses and strains due to cyclic loading are evaluated using standard S – N curves or e – N curves. The specific industry practice is to convert measured strains to stresses in order to enter the S – N curves presented in [44]. As indicated previously, a strain based approach is given in [18].

When the stress amplitude or strain amplitude are constant, the respective S – N or e – N curves may be used directly. However, actual operation presents variable stress and strain results as a direct consequence of the variable loading exhibited in Figures 6.1 and Figure 6.2. The corresponding strain measurements are given in Figure 6.3 and Figure 6.4 respectively. To evaluate cyclic loading where the loading amplitude is variable, referred to as spectrum loading, an evaluation technique must correlate the damage incurred by actual loading with damage incurred during constant amplitude loading. The premise is to ascribe a fatigue damage fraction to each level of cyclic loading until the damage fraction sums to a critical value.

Industry practice is to use the Palmgren – Miner linear damage accumulation model to determine failure life [44]. If the total number of load cycles at a given level of stress, S_i produce failure in N_i cycles, then exposure to only n_i cycles are then postulated to produce a damage fraction of n_i / N_i . The impact of operation at several levels of stress is a summation of damage fractions, where failure is held to occur when the summation equals or exceeds a value of 1.

$$\sum_{j=1}^i \frac{n_j}{N_j} \geq 1 \quad [6.10]$$

The hypothesis holds that loading sequence and temperature below an upper limit of 700 °F [371 °C] does not affect the rule [36, 44]. Extension to the higher temperatures experienced on the coke drum, i.e. 850°F [454 °C] is routinely made per industry practice for temperatures below the creep range.

6.2 Critique of Available Experimental Data

1. Strain Gauge Installation and Measuring Practice

Reference [8] indicates that thermocouples and strain gauges were not covered with insulation after installation. Increased convective and radiation heat loss is expected in the uninsulated shell areas resulting in localized “cool spots”. Tensile strains are to be expected at the strain gauge locations. With an oil-in temperature of 900 °F [482 °C], an insulated shell temperature of 800 °F [427 °C] is expected suggesting, based on other data, a cool spot of 150 °F [66 °C], i.e. the measured shell temperature measured is 650 °F [343 °C] at the gauge locations causing an apparent strain of 975 ue. This is directionally consistent with the measured strains of 500 ue to 600 ue exhibited in Figures 6.3 and 6.4 during the oil-in step. Some reduction due to compressive effects of the cladding can be accounted for in a detailed calculation.

2. Strain Gauge Measuring Practice

A second source of error in the data shows that strain gauges are installed based on the assumption that the principal stress directions are parallel to the circumferential and longitudinal directions of the pressure vessel [8, 18, 48, 49]. Therefore, industry practice is to install only two gauges at each location. This is adequate for pressure vessel equipment when gauges are mounted away from discontinuities under pressure loading. However, for equipment under randomly oriented thermal loading the principal stress directions will vary and must be established using a 3 gauge strain rosette [52] for accuracy in determining maximum magnitude and principal directions.

3. Thermal Strain

The third source of error is associated with failure to explicitly account for the free thermal strain of the shell. The available data indicates that free thermal strain was not accounted for in earlier work [8]. In Figures 6.3 and 6.4, it can be seen that strain readings increase as the operational cycles progress from steam testing to vapor heat up and to oil in stages. In Figure 6.3, strain readings begin to increase at hour 3 coincident with temperature and pressure increment caused by steam testing. At hour 6, vapor heat is initiated and oil-in is initiated at hour 6. The coincident strain increases generally match this pattern which indicates that the gauges are measuring the combined mechanical and thermal strain.

Review of more recent industry work indicates that strain gauge readings are currently zeroed shortly after steam testing begins [48, 51]. Although this partially reduces the error of reading thermal strains as mechanical strains, the error is not eliminated since further thermal strain occurs in rising from a steam test temperature of 250 °F [121 °C] to the shell temperature of 800 °F [427 °C], reached during oil in. There is no indication in the literature that further adjustment is made during water quench. Therefore, an error, due to lack of similar adjustment during cool down, results in reintroduction of free thermal strains into the assessment of mechanical strains.

The strain gauges that are mounted on the coke drum measure total strain, ϵ_T . The total strain is comprised of two parts, one part due to free thermal strain and the second due to mechanical strain such that , $\epsilon_T = \epsilon_{TH} + \epsilon_M$ [34]. When thermal expansion is not constrained, the total strain is equal to the thermal strain, i.e. $\epsilon_T = \epsilon_{TH}$. However, when thermal expansion is completely constrained, then $\epsilon_T = 0$ and $\epsilon_M = - \epsilon_{TH}$. The value of either ϵ_M or $E \cdot \epsilon_M$ is used then to evaluate the fatigue life, N_f .

4. Equivalent Stress and Strain

A coker drum vessel is essentially in plane stress given the small value of radial stress in the shell. However, the shell experiences general strain and an equivalent strain expression taking account of the 3 orthogonal components of strain needs to be utilized. Since low cycle fatigue is generally regarded as a strain controlled failure mechanism [36, 53], the three dimensional strain field must be accounted for in calculating the strain range for a load block. This has particular importance during thermal loading where the biaxial stress field tends to a 1:1 ratio and significantly affects the through thickness shell strain and life evaluation. Harvey [36] and Moguerou [54] illustrate the need to use the equivalent strain in evaluating low cycle, high strain fatigue life.

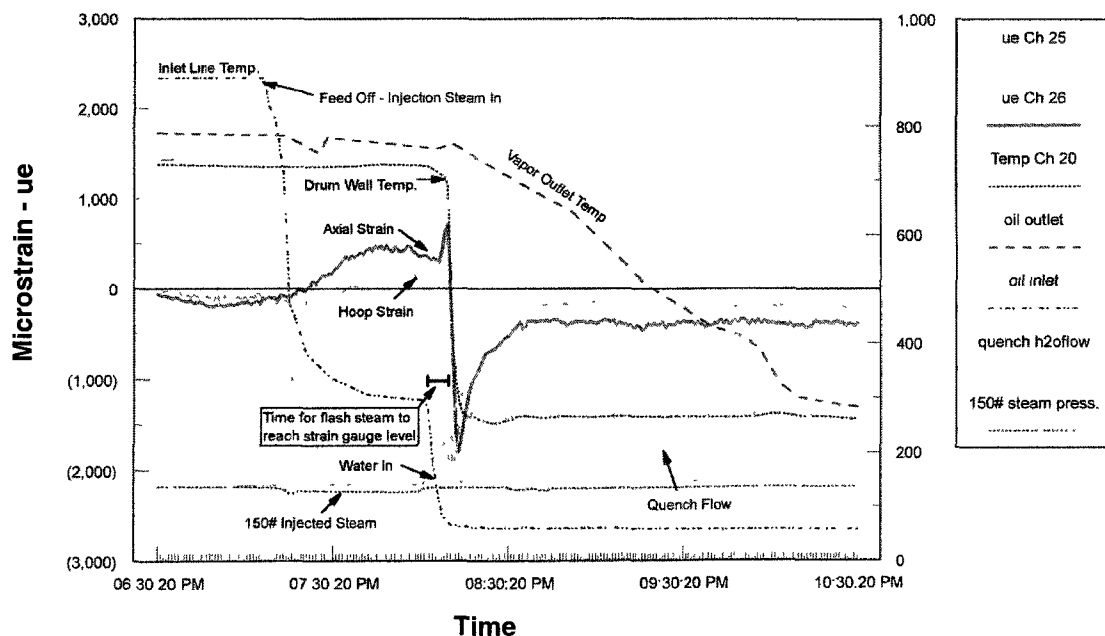
6.3 Reevaluation of Selected Experimental Data

Experimental data was provided in references [8, 48] for the same coke drum vessel taken almost 10 years apart. An additional study was provided for an adjacent vessel taken within the same time frame [49].

Temperature and strain measurements are given in Figures 6.1 through 6.4 from reference [8]. The authors report a maximum principal strain range of 1,700 ue (axial) measured during the series of measurements. The data presented in Figures 6.3 and 6.4 show a maximum strain range of 1,000 ue for the specific series. Of note is that tensile and compressive strains are exhibited indicating that both “cold” and “hot” spots occur during the operational phase.

The data from [49] superimposes operational and experimental data to show the relatively sudden reversal in strain during the water quench phase. A strain range of ~ 2,500 ue is exhibited in the specific sequence given in Figure 6.5 by the gauge reading labeled “ue Ch 26”.

Figure 6.5 Strain and Operational Data from Reference [49]



As discussed previously, the accuracy of strain gauge readings is suspect and therefore, an independent approach is required. An upper bound calculation is proposed based on the extremes in temperature shown in the figure.

In general, the upper bound calculation asserts that the possible set of numbers must be less than or equal to a limiting value. In order to determine the stresses and strains attributable to thermal loading, the upper bound temperature difference calculable is based on the simultaneous maximum and minimum temperatures realizable in the coke drum. With wall temperature showing as 750 °F [398 °C] prior to quenching and quench water temperature appearing to be 250 °F [121 °C], a maximum temperature difference of 500 F° [278 C°] is a reasonable bounding value. The accuracy of the temperature readings is assured in comparison to the accuracy of the strain gauge readings, which was discussed above. In addition, the temperatures of the plant operating streams is well monitored, accurately calibrated and maintained to ensure safety and economical operation of the plants and can be used to compare against temperature reading obtained by temporary thermocouples used to measure coke drum wall temperature.

6.4 Comment on Existing Evaluations

Review of the current literature and private reports made available for this thesis demonstrate that the experimental technique and evaluation of the data are inadequate and understate the amount of damage being incurred by the equipment. It was not possible to obtain new, more accurately derived data for this effort; however, a bounding approach may be applied to the problem from a better understanding of the available data.

6.5 Re- evaluation of Existing Industry Data

System parameters include stream temperatures and pressures as listed in Table 1.3. Experimental data taken by plant instruments support the accuracy of these data. In addition, coke drum shell temperatures, as measured by thermocouple devices are taken to be generally precise and accurate when properly mounted. As previously observed, error was likely incurred when insulation was not replaced over the thermocouples. Data from more recent investigations are taken to be correct, since insulation was replaced for these thermocouples.

As discussed, strain gauge readings are not considered accurate since a 2 gauge orthogonal arrangement has historically been used and appears to be the current practice. The tasks to be undertaken is to upper bound estimate the strain range and determine the cyclic exposure in order to estimate a lower bound fatigue life.

6.5.1 Surface Temperature Change versus Through-Thickness Temperature Change

The strain data can be bound based on maximum temperature difference realizable during operation. There are two possibilities:

- an idealized strain model whereby temperature in a plate is uniform through thickness but held at its edges, the strain amplitude is given by [36, 55, 56]

[6.11]

$$\varepsilon = \pm \alpha \cdot \Delta T / (1 - \mu),$$

where the use of '±' indicates that the local volume may be cooler, resulting in tensile strains, or hotter, resulting in compressive strains, than the surrounding volume of material. This expression is used to assess strain where the through thickness average temperature varies between adjacent portions of the shell.

- an idealized strain model whereby temperature varies from the inside face to the outside face, and therefore, the strain amplitude is given by [36, 55, 57, 58]

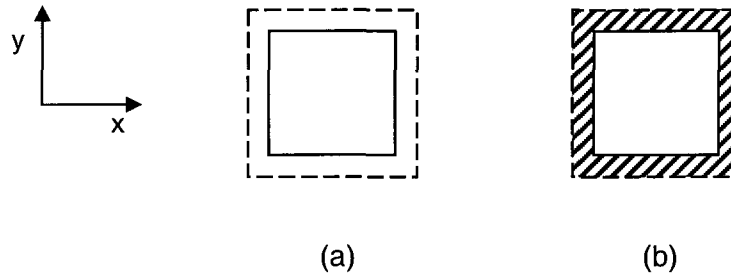
[6.12]

$$\varepsilon = \pm \frac{1}{2} \cdot \alpha \cdot \Delta T / (1 - \mu),$$

where use of '±' indicates that one surface area may be cooler, resulting in tensile strains, or hotter, resulting in compressive strains, than the opposite surface. The expression is valid for a uniform flat plate held at its edges but subjected to a uniform temperature on one face differing from the temperature on the opposite face. This expression is used to assess strain where sudden temperature transients are imposed such as during the steam quench and water quench phases where the incoming fluid stream temperature is different than the drum shell temperature.

The development of the expression given in equation [6.11] can be illustrated by a plate which is free to expand in all directions when heated by an incremental temperature of ΔT in Figure 6.6(a), in comparison to a plate constrained in both directions, Figure 6.6(b).

Figure 6.6 Thermal Strains Occurring in a Thin Plate



For the configuration illustrated in Figure 6.6(a), there are thermal strains in the two lateral directions, but no stresses occur since the plate is not constrained. The magnitudes of the thermal strains are,

$$\epsilon_{therm-x} = \epsilon_{therm-y} = \alpha \cdot \Delta T \text{ and do not result in mechanical strains.} \quad [6.13]$$

In Figure 6.6(b), expansion is constrained in the x-direction and y-directions leading to a bi-axial stress condition wherein:

$$\epsilon_x^T = \epsilon_{mech} + \epsilon_{therm} = \frac{\sigma_x}{E} - \frac{\mu \cdot \sigma_y}{E} + \epsilon_{therm-x} = 0, \text{ in the x – direction, and} \quad [6.14]$$

$$\epsilon_y^T = \epsilon_{mech} + \epsilon_{therm} = \frac{\sigma_y}{E} - \frac{\mu \cdot \sigma_x}{E} + \epsilon_{therm-y} = 0, \text{ in the y – direction.} \quad [6.15]$$

Multiply each side of [6.15] by μ , add to [6.14] and substitute per [6.13] to obtain;

$$\varepsilon_x^T = \frac{\sigma_x}{E} - \frac{\mu \cdot \sigma_y}{E} + \varepsilon_{therm-x} = 0$$

$$\mu \cdot \varepsilon_y^T = \mu \cdot \frac{\sigma_y}{E} - \frac{\mu^2 \cdot \sigma_x}{E} + \mu \cdot \varepsilon_{therm-y} = 0$$

$$\varepsilon_x^T + \mu \cdot \varepsilon_y^T = \frac{\sigma_x}{E} - \frac{\mu \cdot \sigma_y}{E} + \frac{\mu \cdot \sigma_y}{E} - \frac{\mu^2 \cdot \sigma_x}{E} + (1 - \mu) \cdot \alpha \cdot \Delta T = 0$$

and, rearrange in terms of σ_x and σ_y and, simplifying to obtain

$$\sigma_x = -\frac{E \cdot (1 - \mu) \cdot \alpha \cdot \Delta T}{1 - \mu^2} = -\frac{E \cdot \alpha \cdot \Delta T}{1 + \mu} \quad [6.16]$$

$$\sigma_y = -\frac{E \cdot (1 - \mu) \cdot \alpha \cdot \Delta T}{1 - \mu^2} = -\frac{E \cdot \alpha \cdot \Delta T}{1 + \mu} \quad [6.17]$$

Therefore, in terms of mechanical strain, using equations [3.10]

$$\varepsilon_x = \frac{\sigma_x}{E} - \frac{\mu}{E} \cdot \sigma_y = -\alpha \cdot \Delta T = \varepsilon \quad [6.18]$$

$$\varepsilon_y = \frac{\sigma_y}{E} - \frac{\mu}{E} \cdot \sigma_x = -\alpha \cdot \Delta T = \varepsilon \quad [6.19]$$

$$\varepsilon_z = -\frac{\mu}{E} \sigma_x - \frac{\mu}{E} \cdot \sigma_y = \frac{2 \cdot \mu}{1 - \mu} \cdot \alpha \cdot \Delta T = -\frac{2 \cdot \mu}{1 - \mu} \cdot \varepsilon \quad [6.20]$$

$$\text{for } \mu = \frac{1}{2}, \varepsilon_z = 2 \cdot \varepsilon \quad [6.21]$$

$$\text{for } \mu = 0.3, \varepsilon_z = -\frac{6}{7} \cdot \varepsilon \quad [6.22]$$

and, from equation [6.8]

$$\begin{aligned} \text{for } \mu = \frac{1}{2}, e_{eff} &= \frac{\sqrt{2}}{3} \left[(\varepsilon - \varepsilon)^2 + (\varepsilon + 2 \cdot \varepsilon)^2 + (-2 \cdot \varepsilon - \varepsilon)^2 \right]^{1/2} \\ &= 2 \cdot \varepsilon = -2 \cdot \alpha \cdot \Delta T \end{aligned} \quad [6.23]$$

$$\begin{aligned} \text{for } \mu = 0.3, e_{eff} &= \frac{\sqrt{2}}{3} \left[(\varepsilon - \varepsilon)^2 + \left(\varepsilon + \frac{6}{7} \cdot \varepsilon \right)^2 + \left(-\frac{6}{7} \cdot \varepsilon - \varepsilon \right)^2 \right]^{1/2} \\ &= 1.238 \cdot \varepsilon = -1.238 \cdot \alpha \cdot \Delta T \end{aligned} \quad [6.24]$$

For the expression given in equation [6.12], two situations are possible. The first situation is that of a steady state linear temperature gradient through the wall thickness and the expression given in equation [6.12] is taken as valid. In the event of a rapid transient, only a thin layer of material at the surface is exposed to the new temperature, while the bulk of the material remains at the initial temperature. In this event, the layer is constrained biaxially and the expression given in equation [6.11] is taken as limiting when using the temperatures of the contacting fluid and drum shell.

For the expression given in equation [6.11] the bounded range is determined to be:

- $\varepsilon = \pm \Delta T \cdot \alpha / (1 - \mu) = (750 - 400) \cdot 7.2E-6 / (1 - \mu) =$
 - $\pm 3,600$ ue for $\mu = 0.3$ and
 - $\pm 5,040$ ue using $\mu = 0.5$ due to plasticity
 - 750 is the drum wall temperature prior to quench in Figure 6.5
 - 400 is arbitrarily set as the surrounding through thickness drum wall temperature, occurring at some time during the quench step
 - the sign is dependant on whether a “cool” spot or “hot” spot is under consideration
 - the strain range is, $\Delta\varepsilon = 7,200$ ue for $\mu = 0.3$ and, $\Delta\varepsilon = 10,080$ ue for $\mu = 0.5$

Using the expressions of [6.24] and [6.23], strain $\varepsilon =$

- $\pm 3,120$ ue for $\mu = 0.3$ and
- $\pm 5,040$ ue for $\mu = 0.5$ and

For the expression given in equation [6.12] the bounded range is determined to be:

- $\varepsilon = \pm \frac{1}{2} \cdot \Delta T \cdot \alpha / (1 - \mu) = \frac{1}{2} \cdot (750 - 250) \cdot 7.2E-6 / (1 - \mu) =$
 - $\pm 2,570$ ue for $\mu = 0.3$ and
 - $\pm 3,600$ ue using $\mu = 0.5$ due to plasticity
 - 750 is the drum wall temperature prior to quench in Figure 6.5
 - 250 is the quench water temperature indicated in Figure 6.5
 - the sign is dependant on whether a “cool” spot or “hot” spot is under consideration
 - the strain range is, $\Delta\varepsilon = 5,140$ ue for $\mu = 0.3$ and, $\Delta\varepsilon = 7,200$ ue for $\mu = 0.5$

Using the limiting case caused by surface effects during transient heat transfer and the expressions of [6.11], [6.23] and [6.24] then, strain $\varepsilon =$

- $\pm 5,140$ ue for $\mu = 0.3$ and
- $\pm 7,200$ ue for $\mu = 0.5$
- the strain range is, $\Delta\varepsilon = 10,280$ ue for $\mu = 0.3$ and, $\Delta\varepsilon = 14,400$ ue for $\mu = 0.5$

6.5.2 Consideration of Discontinuity Stresses Caused by Clad Fabrication

It should be noted that the above have been developed for a single material thickness. Since the coker drum shell is a composite fabrication of clad and base material, some examination of stresses resulting from the discontinuity in material properties is necessary. The coefficient of thermal expansion [CTE] of the clad material, TP 410S stainless is given in Table 4.1 and is seen to differ from the CTE of base material by some 18% at ambient temperature to 37% at 800 °F [427 °C] as a percentage of the values of TP410S.

The expressions for stress generated in the clad and base material are developed in Appendix 1. For base material, the biaxial stress is given by –

$$\sigma_{1-x,z} = \frac{(\alpha_2 - \alpha_1) \cdot (T_1 - T_0) \cdot E_1}{1 + \frac{t_1}{t_2} \cdot \frac{E_1}{E_2}} \cdot \frac{1}{1 - \mu} \quad [6.25]$$

For the clad material, the biaxial stress is given by –

$$\sigma_{2-x,z} = - \frac{(\alpha_2 - \alpha_1) \cdot (T_1 - T_0) \cdot E_1}{1 + \frac{t_2}{t_1} \cdot \frac{E_1}{E_2}} \cdot \frac{1}{1 - \mu} \quad [6.26]$$

For the physical properties given in Table 4.1, and using the operating temperature difference typically encountered in a coker drum and, the thicknesses used in the numerical analysis of the following chapter, the stresses are

$$\sigma_{1-x,z} = -4,050 \text{ psi } [-28.0 \text{ MPa}]$$

$$\sigma_{2-x,z} = 41,600 \text{ psi } [286.8 \text{ MPa}]$$

Reference [36] gives a simplified expression for cladding stress as

$$\sigma = -\frac{(\alpha_{clad} - \alpha_{base}) \cdot (T_1 - T_0) \cdot E}{1 - \mu}, \text{ from which} \quad [6.27]$$

$$\sigma = -\frac{(7.1E-6 - 8.9E-6) \cdot (800 - 100) \cdot 26.3E6}{1 - \mu} = 47,340 \text{ psi } [326.4 \text{ MPa}]$$

which provides an upper bound value to the more accurate expression developed in equation [6.26]. Expression [6.27] calculates a larger value for the cladding stress since it disregards the finite rigidity of the base material. It can be seen from the fully developed expression in equation [6.26] that equation [6.27] is adequate where the cladding thickness is less than 10% of the thickness of the base material.

6.5.3 N_i Failure Determination Based on Bounding Approach

Using the strain life data of Sonoya [59] and Ramos et al. [14], we can summarize, per industry practice, the fatigue life capability at each range of strain, as follows:

Table 6.1 Lower Bound Life Determination for Coke Drum Shell

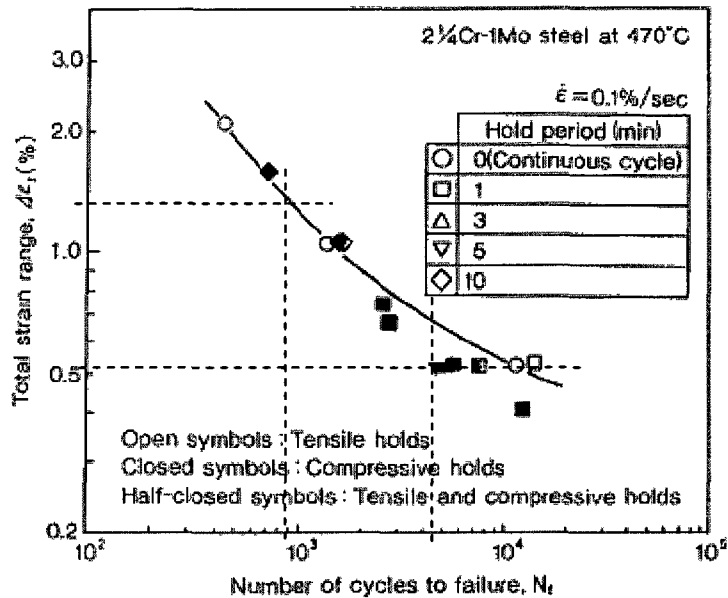
Expression	Eq'n	ΔT	μ	ϵ	$\Delta \epsilon$	N1	N2
$\pm \frac{1}{2} \alpha \cdot \Delta T / (1-\mu)$	[6.12]	500	.3	$\pm 2,570$	5,140	4,500	4,000
			.5	$\pm 3,600$	7,200	2,800	2,000
$\pm \alpha \cdot \Delta T / (1-\mu)$ [3]	[6.11]	500	.3	$\pm 5,140$	10,280	1,500	1,200
			.5	$\pm 7,200$	14,400	900	800
$\pm \alpha \cdot \Delta T / (1-\mu)$	[6.11]	350	.3	$\pm 3,600$	7,200	2,800	2,000
			.5	$\pm 5,040$	10,080	1,500	1,200
$\pm 1.238 \cdot \alpha \cdot \Delta T$	[6.24]	350	.3	$\pm 3,120$	6,240	-	-
$\pm 2 \cdot \alpha \cdot \Delta T$	[6.23]	350	.5	$\pm 5,040$	10,080	-	-

Notes to Table 6.1

1. N1 \equiv strain life in cycles [59]
2. N2 \equiv strain life in cycles for 1¼ Cr material [14]
3. Equation [6.11] is the limiting condition to [6.12] during transient heat transfer.

Application of strain life determination to the strain data given in Table 6.1 is illustrated below. Consider the first entry of Table 6.1 showing a strain range of 5,140 ue. The corresponding cycles to failure is approximately 4,500 cycles per Figure 6.7. This is the experimentally measured value for the indicated constant strain range loading of 5,140 ue. For the maximum constant strain range of 14,400 ue, the indicated cyclic life is 900 cycles. The values of 4,500 and 900 represent the N_i values, identified in section 6.1.2 above. Using the data of Ramos et al. [15] provides the cyclic life values in the column labeled N2.

Figure 6.7 Low Cycle Strain Life for 2¼ Cr – 1 Mo Steel [59]



In Table 6.1, N1 and N2 are based, respectively, on the use of 2¼ Cr – 1 Mo and 1¼ Cr – ½ Mo low alloy steel materials commonly used in coke drums. Industry practice [45] is to consider these steels using a single S – N curve. As shown in Table 6.1, there is a difference in the cyclic life determined between the two materials, amounting to some 12% to 40%. These values impact directly on any prediction of service life for actual equipment, the difference amounting to several years in operating life since the equipment is cycled only approximately once per day.

6.5.4 An Example of Cyclic Life Determination

The data of Ramos et al. [15] and Boswell [18] indicate that a single strain value is not experienced at the test locations during each cyclic exposure but, rather, a distribution occurs resembling a Poisson distribution [60]. Figure 6.8 is the normalized strain distribution of the data given in Ramos et al. [15]. Figure 6.9 is the normalized strain distribution of the data presented in [18].

Figure 6.8 Strain Range Frequency Data [15]

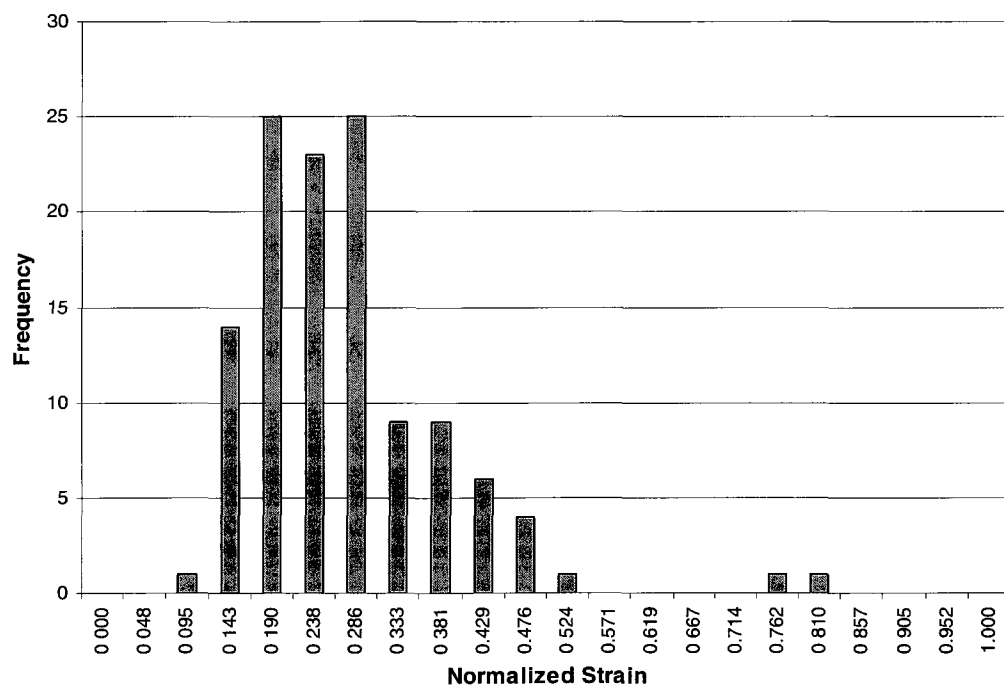
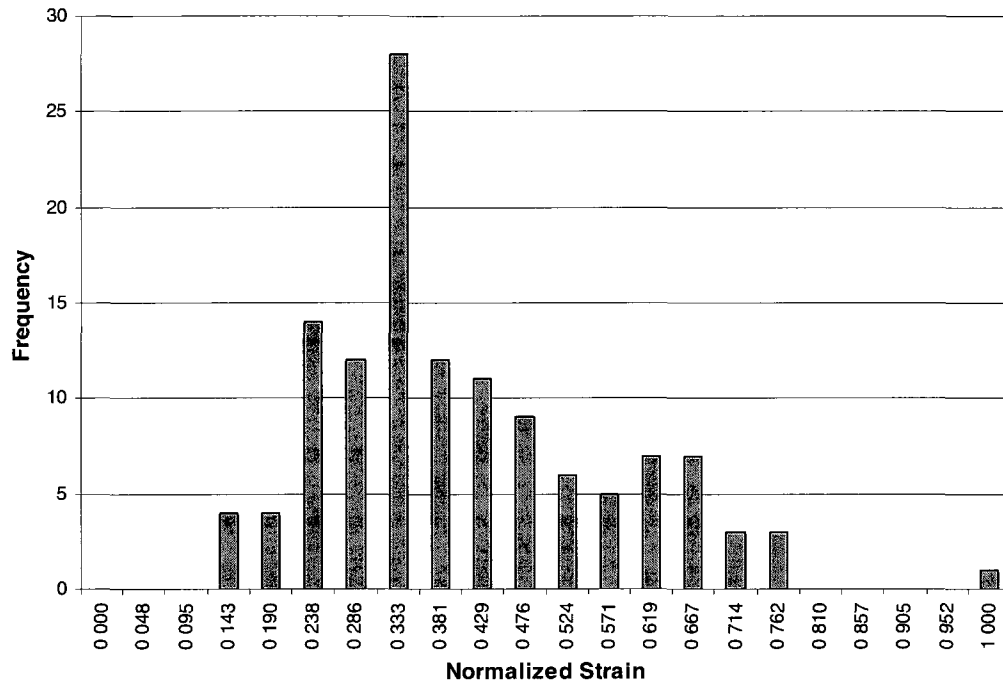


Figure 6.9 Estimated Hoop Strain Range Frequency Data [18]



The measurement of strain on the coker drum shell has been shown to be non-conservative. If the data presented in the original references is evaluated using conventional industry practice, the results given in Table 6.2 as “industry practice” values are obtained. If the normalized data of Figure 6.8 and Figure 6.9 are applied to the upper bound estimates of strain, the cyclic life determinations yield the additional results given in Table 6.2.

Table 6.2 Comparison of Cyclic Life Determinations for Coke Drum Shell

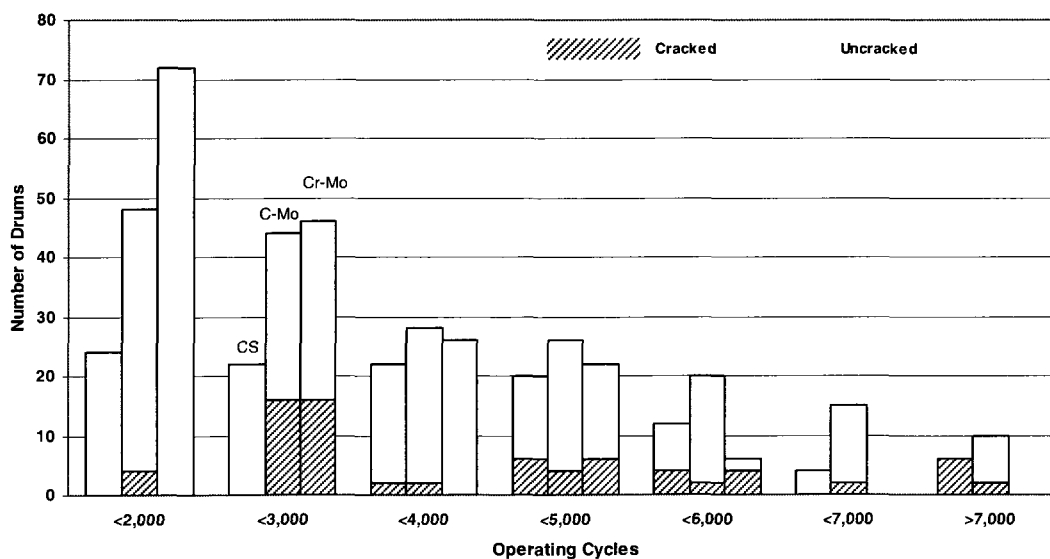
Distribution	Industry Practice		Upper Bound Estimate			
	[cycles]	[years]	$\Delta\epsilon = 7,200$ ue [cycles]	[years]	$\Delta\epsilon = 14,400$ ue [cycles]	[years]
Figure 6.8	99,970	273	73,490	201	3,948	10.8
Figure 6.9	93,250	255	28,593	78	4,603	12.6

Notes to Table 6.2

1. 7,200 ue upper bound \equiv an upper bound strain limit defined in Table 6.1
2. 14,400 ue upper bound \equiv an alternate upper bound strain limit defined in Table 6.1

Reference [7] provides a survey of 145 coke drums indicating as to when the first through-wall crack was experienced for drums constructed of carbon steel (CS), carbon-moly (C-Mo) and chrome-moly (Cr-Mo) base material. The data is presented in Figure 6.10. As can be seen, first crack failures occurred well below assessments utilizing the data of [15] and [18], evaluated according to conventional industry practice. Using the upper bound estimate approach exhibits improved correlation and reflects the use of improved analytical expressions and likely temperature exposure levels.

Figure 6.10 Number of Drums Reporting First Through Wall Crack [7]



6.5.5 Impact of Pressure Cycling

Per industry practice, the stress due to internal pressure in a cylinder is given by Timoshenko [61] simply as

$S_h = \frac{p \cdot d}{2 \cdot t}$, and for the specifics of this study, with $p = 35$ psig [241 kPa], $d = 312$ inches [7,924.8 mm] and, $t = 1$ inch [25.4 mm];

$S_h = 5,460$ psi [37.7 MPa] < 16,600 psi [114.5 MPa], the allowable stress for SA 387 22 i.e. 2¼ Cr – 1 Mo material of construction.

Stress due to pressure is bi-axial, with the stress in the hoop direction of the cylinder as stated above and, stress in the longitudinal or axial direction given as

$S_l = \frac{p \cdot d}{4 \cdot t}$. Evaluation for fatigue is made on the basis of the nominal stress of 5,460 psi [37.7 MPa] according to WRC 432 Figure 19 [62]. The effect of gross discontinuities and stress concentrations due to welds and defects requires additional evaluation. For shell sections remote from gross discontinuities such as the bottom or top head, no consideration is required. Stress concentrations caused by welds in a 2:1 biaxial stress field may be taken as 2.4, based on the calculated results of Table 7.6 and the guidance provided in reference [62]. The maximum stress is calculated as 13,104 psi [90.4 MPa] and the cyclic service life is estimated to be in excess of 1 E6 cycles. For a cyclic service life of 1E6 cycles, the maximum stress range is given as 20,000 psi [137.9 MPa] per reference [62]. Consequently, failure due to pressure cycling is not governing.

6.5.6 Impact of Live Weight Cycling

Live weight cycling occurs as a consequence of hydrostatic stress caused by the filling and emptying of vessel contents. This loading produces only a hoop stress since the ends of the vessel are free to deform and are unloaded. The equivalent pressure stress is given by Bernoulli's expression [63] as – $p = \gamma \cdot H$ and, for the specifics of this study, $\gamma = 62.4 \text{ lb}_f / \text{ft}^3$ [$1000 \text{ kg} / \text{m}^3$], $H = 600 \text{ inches}$ [$1,524 \text{ mm}$].

Therefore, hydrostatic pressure, $p = 21.7 \text{ psig}$ [149.6 kPa] and $S = 21.7 \cdot 312 / (2 \cdot 1) = 3,380 \text{ psi}$. From Table 7.6, a stress concentration factor of 2.5 is selected [1:0 biaxial stress field] and a maximum stress of 8,450 psi [58.2 MPa] is obtained. This is below the threshold value of 20,000 psi [137.9 MPa] for service failure in 1E6 cycles. Consequently, failure due to live-weight cycling is not governing.

6.5.7 Impact of Combined Pressure plus Live Weight Cycling

The combined stress due to pressure plus live weight cycling is simply calculated as $5,460 + 3,380 = 8,840 \text{ psi}$ [61.0 MPa]. Accounting for stress concentrations leads to a maximum stress of 21,550 psi [148.6 MPa] and is slightly greater than the threshold value of 20,000 psi [137.9 MPa] for service failure in 1E6 cycle. Consequently, failure due to combined pressure plus live-weight cycling is not governing.

6.6 Summary

The expressions used by industry to determine strains and stresses were found to be incorrect. The experimental technique used to measure strains in operating coke drums was also found to be incorrect since thermal strains were evaluated as mechanical strains.

The closed form solution models found in the literature for determination of thermal strains and stresses were found to be adequate and found to implicitly account for the multi-axial strain and stress state.

A review of the various loads acting on a coke drum identified pressure, dead weight and live weight cycling as not being sufficiently severe to influence the exhibited fatigue life. The primary load influencing the limited life of the equipment was identified as thermal loading caused by two primary mechanisms. The first mechanism is caused by the interface stress between clad and base material due to differential thermal expansion. Secondly, differential temperatures occurring in the coke drum shell during the quench phase when quench water is rapidly introduced into a hot coke drum vessel cause localized “hot” and “cold” spots depending on hydraulic conditions. Although the operational sequencing nominally repeats, vessel internal conditions cause random temperature loading of the shell.

CHAPTER 7 ANALYSIS – NUMERICAL MODELS

7.1 Introduction

The intent of the following numerical models is to confirm the upper bound determinations presented in the previous section. As already discussed, the strain measurements available for this work are inaccurate due to the testing methodology, but are helpful in regard to trends and establishing patterns of response. The temperature measurements taken by some investigators are compromised where insulation had not been replaced over the thermocouples. As well, even where temperature readings are likely accurate,

- a small number of data points were monitored
- the sampling rate is unknown
- cleanliness of heat transfer surfaces is not known

As a result, local temperature gradients could not be accurately determined from the available data.

Numerical models were therefore constructed to examine the impact of transient and steady state temperature loading. Temperature loading was applied to a series of models to test response to

- radial temperature loading
- longitudinal temperature loading
- radial and longitudinal temperature loading with weld defect

7.2 Temperature Dependant Material Properties

Temperature dependant material properties were used for clad, weld overlay and base material. Material non-linearity is accounted for by using a bi-linear kinematic hardening option with tangent modulus determined from the cyclic stress-strain results presented in Figure 4.1 thru Figure 4.6. The bi-linear model was used for simplicity and given the limited strain range of < 1%. Modeling of the clad-base metal interface is done by direct connection of elements on the basis of the metallurgical bond quality along essentially the entire surface as described in the material fabrication specification. Non destructive examination [NDE] testing assures this level of quality [4].

Typical butt-weld fabrication by Code allows for a cover pass weld profile. The practice in recent fabrication of DCU coker drums is to grind ID and OD weld surfaces to eliminate stress raisers. The models used in this work retain a weld cover profile since many existing units were fabricated in this manner and the data from these units is used in this work.

In the current numerical analysis, base weld properties were made identical to base material properties since fabrication practice is to match weld to base materials.

The clad restoration weld however, does not follow this philosophy. The past practice was to use a high nickel alloy rod, such as ERNiCrFe-3 [UNS W86133] but favoured recently is ERNiCrMo-3 [UNS N06625], a high nickel rod with molybdenum content, for new fabrication and weld repair.

Table 7.1 Chemical Composition Requirements for Weld Metal [%] [64]

Material	C	Mn	Cr	Mo	P	S	Si	Ni	Nb
ERNiCrFe – 3	.10	7.5	15	-	.03	.015	1.00	59	1.75
ERNiCrMo – 3	.10	.50	21.5	9	.02	.015	.50	58	3.65

Table 7.2 Some Material Properties Derived from Testing

Material		Monotonic		Cyclic	
		room – 70 F	high – 800 F	room – 70 F	high – 800 F
1¼ Cr – SA 387 G11 Class 1	E	28 2 E6	23 0 E6	28 2 E6	27 1 E6
	ET	465,000	1 25 E6	2 08 E6	2 72 E6
	YS	65,000	55,000	65,000	60,000
	PL	67,660	30,000	54,000	45,000
13 Cr – SA 240 TP 410S	E	28 0 E6	16 3 E6	30 0 E6	24 0 E6
	ET	1 14 E6	593,000	893,000	612,250
	YS	53,000	38,000	52,500	45,000
	PL	38,000	25,000	30 000	32,000
CLAD WELD UNS N06625 to 13 Cr	E	24 3 E6	27 3 E6	32 5 E6	26 7 E6
	ET	1 25 E6	550,000	2 50 E6	2 8 E6
	YS	57,500	57,500	65,000	45,000
	PL	40,000	32,500	55,000	20,000

Notes to Table 7.2

- 1 All values in [ksi]
- 2 Table 7 2M provides the data in SI units, following

Table 7.2M Some Material Properties Derived from Testing – SI Units

Material		Monotonic		Cyclic	
		room – 70 F	high – 800 F	room – 70 F	high – 800 F
1¼ Cr – SA 387 G11 Class 1	E	294.4 E3	158.6 E3	194.4 E3	186.8 E3
	ET	3.2 E3	8.6 E3	14.3 E3	18.8 E3
	YS	448	379	448	414
	PL	466	207	372	310
13 Cr – SA 240 TP 410S	E	193.1 E3	112.4 E3	206.8 E3	165.5 E3
	ET	7.9 E3	4.1 E3	6.2 E3	4.2 E3
	YS	365	262	362	310
	PL	262	172	207	221
CLAD WELD UNS N06625 to 13 Cr	E	167.5 E3	188.2 E3	224.1 E3	184.1 E3
	ET	8.6 E3	3.8 E3	17.2 E3	19.3 E3
	YS	396	396	448	310
	PL	276	224	379	138

Notes to Table 7.2M

1. All values in [MPa]
2. Table 7.2 provides the data in US Customary units

7.3 Modeling Strategy

The objective of the numerical modeling is to determine whether the closed form upper bound estimates can be affirmed given the lack of accurate experimental data. The lack of accurate data has been attributed to inadequacies in experimental methods. Therefore, only simplified models with specific loadings were considered.

The data in which there is reasonable confidence includes

- the operational data of Table 1.3
- some temperature data taken by thermocouple, except where deficiencies are known to have occurred [8]
- time durations as evidenced by interpretation of thermocouple data
- heat transfer rates determined from first principles indicated in Table 5.1 and Table 5.2
- heat transfer rates based on correct thermocouple readings
- the normalized strain and stress distributions

The data in which there is lower confidence and to be used with caution includes

- thermocouple readings which were mounted without replacement of insulation
- strain gauge readings which were not zeroed to account for thermal strain
- strain gauge readings which rely on assumed principal stress directions
- temperature change rates as measured by thermocouples since sampling rate is not known
- reported strain and calculated stress ranges

Two basic models were constructed

1. a short length axisymmetric model to test nominal and accelerated temperature loadings varying in the radial or through-thickness direction, with no defect and defect present in the base weld metal
2. a long length axisymmetric model to test nominal and accelerated temperature loadings varying in radial and longitudinal directions, no defect and defect present in the base weld metal

The results of the numerical modeling are presented as stresses for ease of comprehension and familiarity by industry readers. A normal practice in industry is to present non-linear strains as pseudo-elastic stresses by multiplication of the strains using Young's modulus. Referring to Figure 4.3 and Figure 4.6, it can be seen that for base materials, reporting stresses to 50,000 psi [345 MPa] and for TP 410S, reporting stresses to 35,000 psi [241 MPa] will not adversely affect comprehension of the low cycle fatigue mechanism for the scope of this work.

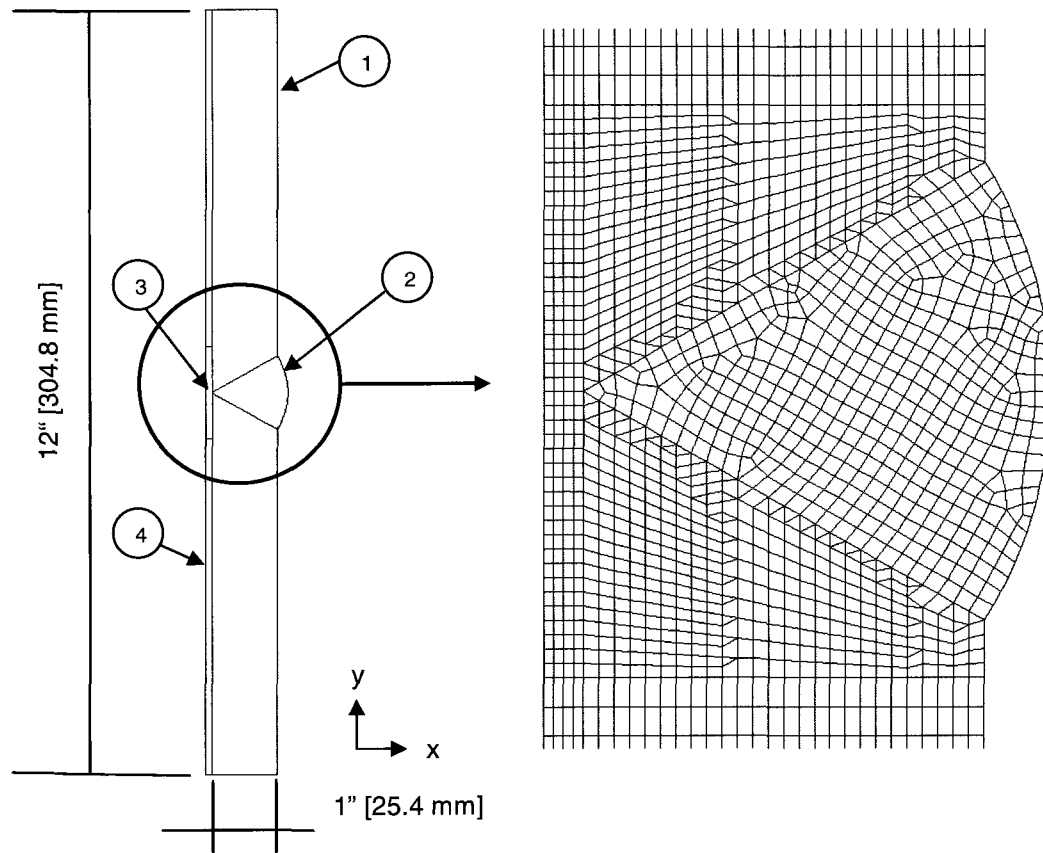
7.4 Radial Temperature Loading Models

The short length axisymmetric thermal FEA model was shown in Figure 5.3 and is modified to perform a multi-discipline analysis to determine the resulting stresses caused from the varying temperature loads. This is accomplished by appropriate definition of boundary conditions and applying thermal loads. The modified model is presented as Figure 7.1. The stress results are displayed in Figure 7.2. Two cycles of operation are shown with the first cycle representing the nominal temperature loading applied throughout the first operational cycle using the heat transfer coefficients [HTC] of Table 5.4.

The second cycle of loading represents an accelerated temperature loading indicative of the rapid temperature drop depicted in Figure 6.5 where a temperature drop of $80\text{ F}^\circ / \text{min}$ [$44.5\text{ C}^\circ / \text{min}$] is sustained. The nominal temperature drop in Table 5.2 is $8.8\text{ F}^\circ / \text{min}$ [$4.9\text{ C}^\circ / \text{min}$] during each half of the water quench step. Therefore, the HTC applied to simulate the accelerated temperature loading cycle was accomplished by increasing the HTC associated with the nominal HTC of Table 5.4 by an order of magnitude. The accelerated HTC, thus obtained, falls within the upper range of HTC calculated in Table 5.2 for surface boiling conductance.

Longitudinal stress is plotted as a function of time. The longitudinal stress is chosen as a stress category of interest as it is consistent with the stress category of interest for Mode I type cracking [65]. Also, some 97% of respondents to the 1996 API survey [7] discussed in chapter [2.1] indicated cracking was primarily in the circumferential direction.

Figure 7.1 Axisymmetric Stress FEA Model at Circumferential Weld



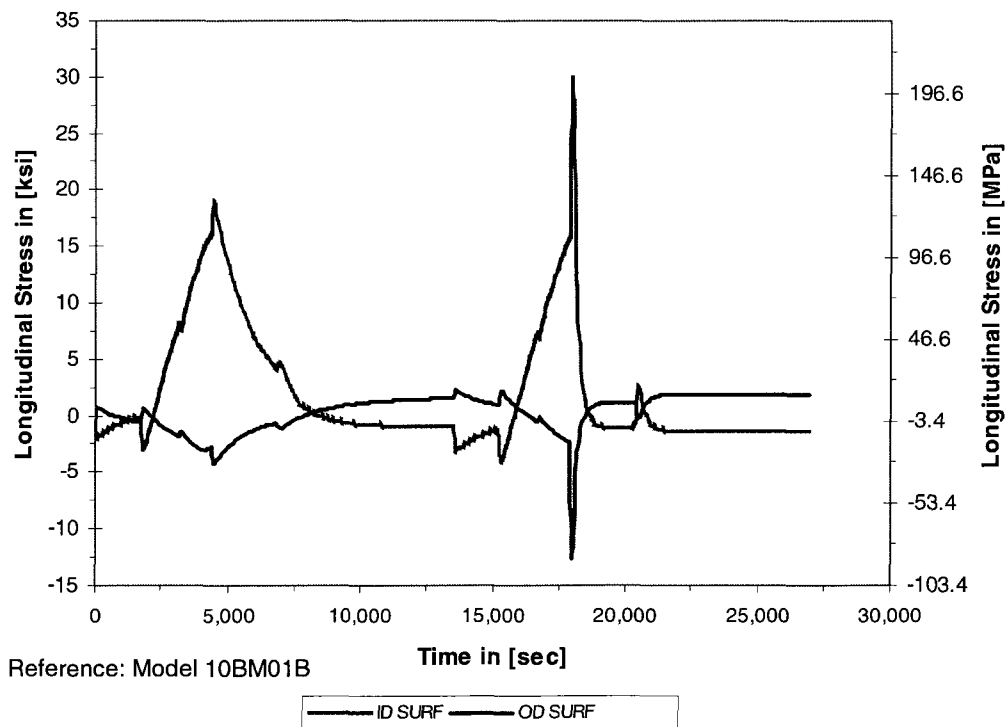
Notes to Figure 7.1

1. Model element is a 2D axisymmetric stress element with two translational degrees of freedom per node
2. The base material thickness is taken as 1" [25 mm] thick, clad liner is 0.100" [2.54 mm] thick
3. Four distinct metallurgical and geometric areas are modeled, 1– base material, 2 – base material weld , 3 – clad restoration weld, 4 – clad liner
4. The differing metallurgical areas are considered fully bonded with no transition properties
5. Displacement boundary conditions are to fix the bottom edge [y = 0] against vertical displacement, the top edge is constrained to remain plane as vertical displacement occurs due to thermal displacement, and free, unconstrained displacement in radial direction [x] is allowed
6. A multi-discipline analysis is completed which requires determination of temperatures and using these as the loads for the stress analysis

7.4.1 Radial Temperature Model – No Defect

To economize computer resources, the long steady state portion of the oil in step, amounting to several hours in duration, is curtailed. Results are also reported as stresses rather than strains to facilitate comprehension by a majority of industry readers who are better acquainted with evaluation of fatigue in terms of stress units and who wish to make comparisons to the more popular form of the data available in the industry, especially code documents. Secondly, since the stress results for the most part remain in the elastic or elasto-plastic regime, the data is more conveniently presented in stress units.

Figure 7.2 Stress Profile for Radial Temperature Model



Several observations are made from the simple model of Figure 7.2

1. An inside diameter [ID] surface tensile stress occurs on temperature loading due to the difference in coefficient of expansion between the TP 410S clad and low alloy steel base plate materials. Refer to Table 4.1 for the temperature dependant values.
2. The outside diameter [OD] surface experiences a compressive stress. Refer to Figure 6.5 which shows a negative strain reading for the coker drum prior to the water quenching, a rise and then severe decline on injection of quench water.
3. The nominal loading cycle [1st cycle shown in Figure 7.2] shows that the OD surface stress increases positively as water quenching occurs; however, during accelerated loading [2nd cycle shown in Figure 7.2] the ID surface experiences a severe up spike and the OD surface stress experiences a severe down spike
4. The maximum stress results should occur at a temperature of 650 °F [343 °C] shell metal temperature. The closed form solution, using the detailed expression of [6.27], is:

$$\sigma_{2-x,z} = -\frac{(\alpha_2 - \alpha_1) \cdot (T_1 - T_0) \cdot E_1}{1 + \frac{t_2}{t_1} \cdot \frac{E_1}{E_2}} \cdot \frac{1}{1 - \mu} \quad [7.1]$$

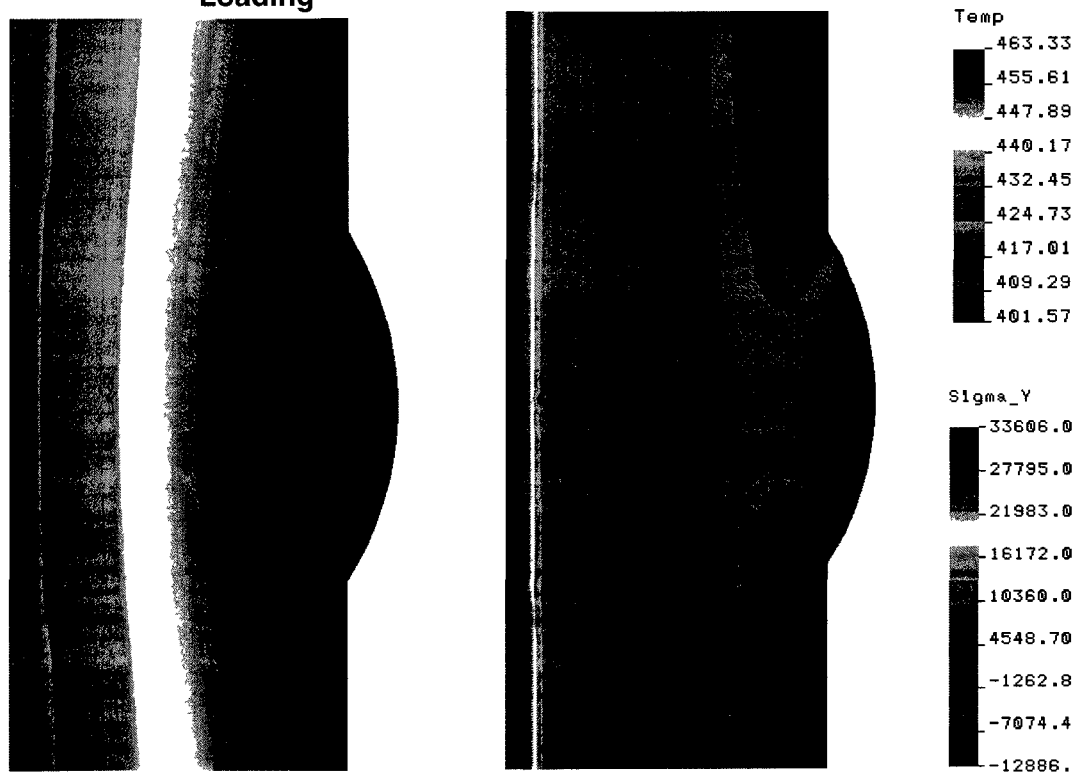
$$= -\frac{(6.9 - 8.5) \cdot (650 - 100) \cdot 26.6}{1 + \frac{0.100}{1} \cdot \frac{26.6}{25.9}} \cdot \frac{1}{1 - 0.3} = 30,325 \text{ psi } [209.1 \text{ MPa}]$$

using the data of Table 4.1 and evaluated at a metal temperature of 650 °F [343 °C] in this instance. The stress levels for the steady state stress part of the FEA model of Figure 7.2 are approximately ½ of calculated, or:

$$\frac{16,250}{30,325} \approx 0.54 \rightarrow \frac{1}{2}$$

The severe up-spike on the ID surface is caused by the superposing of two effects. A “skin” effect is created on the inside surface at the time that the transient has just started because there has been insufficient time for heat conduction to occur. This results in a severe thermal gradient adjacent the surface. The second effect is the added stress attributed to differential temperature between clad and base material. Figure 7.3 shows the temperature and stress profile of the shell approximately 150 seconds after exposure to the accelerated heat transfer coefficient.

Figure 7.3 Temperature – Stress Comparison during Accelerated Loading



(a) Temperature in [°F]

(b) Longitudinal stress Sigma_Y in [psi]

Notes to Figure 7.3

1. View this figure with the graph of Figure 7.5

Plots of the temperature difference between the ID surface and a point at the interface and between the ID and another point at mid-depth of the base material are presented in Figure 7.4 for the nominal temperature loading and in Figure 7.5 for the accelerated temperature loading.

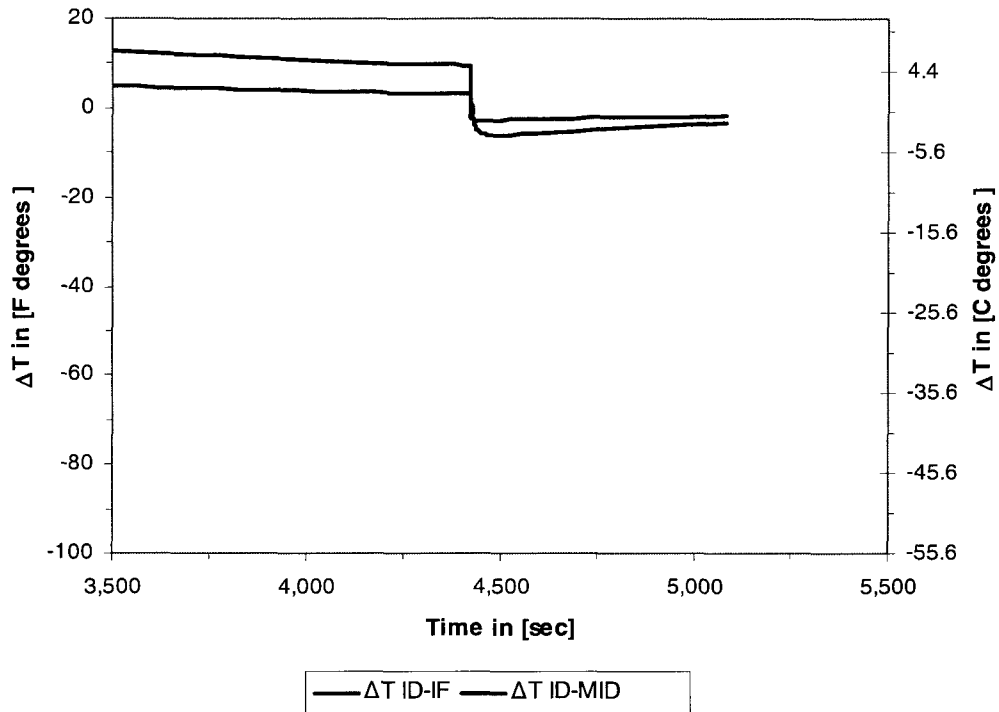
In Figure 7.4, the maximum temperature difference between shell ID and mid wall is 10 F degrees [6 C°] during quench, the ID surface being cooler. The corresponding thermal stress, which occurs since the ID surface contracts in relation to the midwall, calculates as approximately,

$$\sigma = \frac{\alpha \cdot \Delta T \cdot E}{1 - \mu} = \frac{(8.0) \cdot 10^{-6} \cdot 10 \cdot 25.9 \cdot 10^6}{1 - 0.3} = 2,960 \text{ psi [20.4 MPa]} \quad [7.3]$$

The expression of equation [6.11] is used to provide an upper bound estimate of stress due to differences in through-wall temperature under transient heat transfer.

Comparing the result of equation [7.3] to the maximum stress values indicated in Figure 7.2, it is apparent that the major stress contribution is due to the difference in thermal expansion between the coefficients of expansion of TP 410S clad and low alloy base material. Note that the low alloy Cr – Mo materials for coke drum fabrication have similar physical properties and are classed, in specific instances as being in the same material group [10].

Figure 7.4 Temperature Differentials – Nominal Loading



Notes to Figure 7.4

1. ΔT ID-IF \equiv temperature difference between point on ID surface and point on interface along same radial line
2. ΔT ID-MID \equiv temperature difference between point on ID surface and point mid depth of base material along same radial line
3. View this figure with the 1st cycle shown in graph of Figure 7.2

In Figure 7.2, the additional up-spike exhibiting during the 2nd cycle is indicative of the accelerated heat transfer coefficient. The maximum temperature difference between the ID surface and midwall is shown in Figure 7.5, showing a temperature difference of 90 F degrees [50 C°]. The thermal stress calculates, for simplicity, as

$$\sigma = \frac{\alpha \cdot \Delta T \cdot E}{1 - \mu} = \frac{(7.7) \cdot 10^{-6} \cdot 90 \cdot 27.8 \cdot 10^6}{1 - 0.3} = 27,500 \text{ psi } [189.8 \text{ MPa}], \quad [7.4]$$

with properties evaluated at 430 °F [221 °C]. An increase in stress of 15,000 psi [103 MPa] from approximately 15,000 psi [103 MPa] to 30,000 psi [206 MPa] is evident in Figure 7.2.

The clad interface stress, at 430 °F [221 °C] is calculated from equation [6.25] as

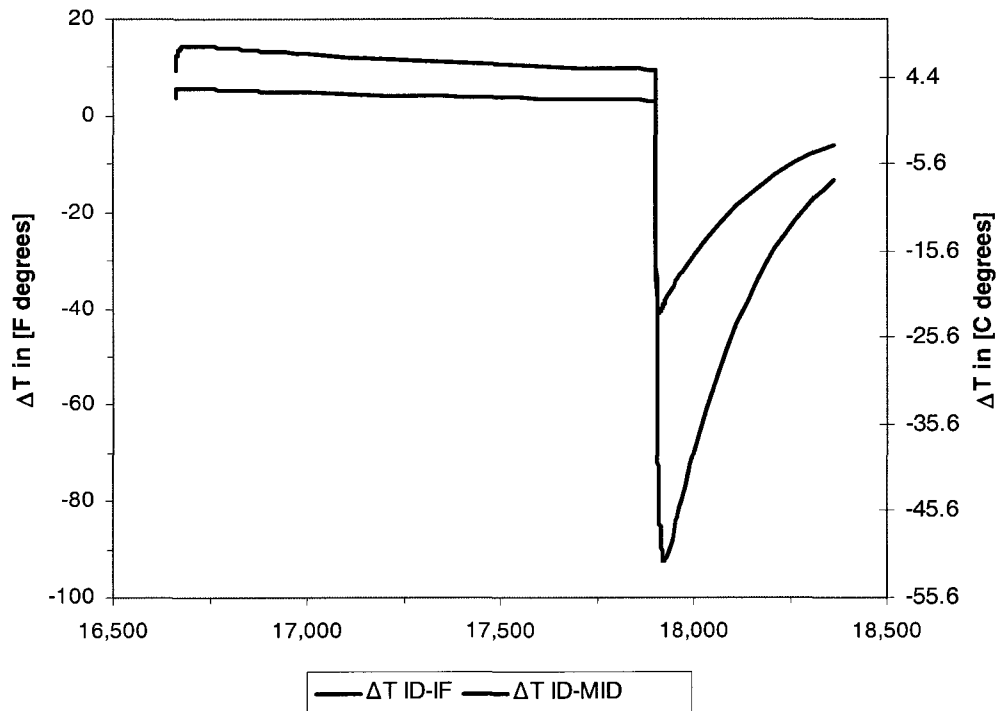
$$\sigma_{clad} = -\frac{(6.7 - 7.8) \cdot (430 - 100) \cdot 27.7}{1 + \frac{0.100}{1} \cdot \frac{27.7}{27.0}} \cdot \frac{1}{1 - 0.3} = 13,030 \text{ psi } [89.8 \text{ MPa}] \quad [7.5]$$

It is apparent then, that an additional restraint mechanism is created when a large thermal gradient is created at the ID surface by rapid cooling. A similar result would occur with rapid heating but the stress component directions would be compressive.

Referring to Figure 6.5, the measured time lapse between start of water quench flow and minimum strain indication is approximately 10 minutes or 600 seconds. The drum wall temperature is seen to decline from approximately 700 °F [371 °C] to 250 °F [121 °C] with a steep drop of 450 F° [250 C°] occurring in 7 minutes. The corresponding strain gauge readings track the temperature gradient.

The measured temperature response indicated in Figure 6.2 displays a time response occurring over a period of several hours for the same temperature difference; the temperature decline from 650 °F [343 °C] to 150 °F [66 °C] occurring between time 33 hours to 42 hours. It is apparent that whether temperature responses occur quickly or occur over a time period of several hours is dependant on the ability of quench water to flow through the pores and channels created in the coke mass residual and to make contact with the coke drum shell. When water contacts the hot shell, the response is immediate and in conformance to the governing heat transfer mechanisms. The structural response of the vessel materials is also consistent with the nature of the applied loadings and the consequent stresses and strains being either mild or severe in response to the severity of the thermal transients.

Figure 7.5 Temperature Differentials – Accelerated Loading



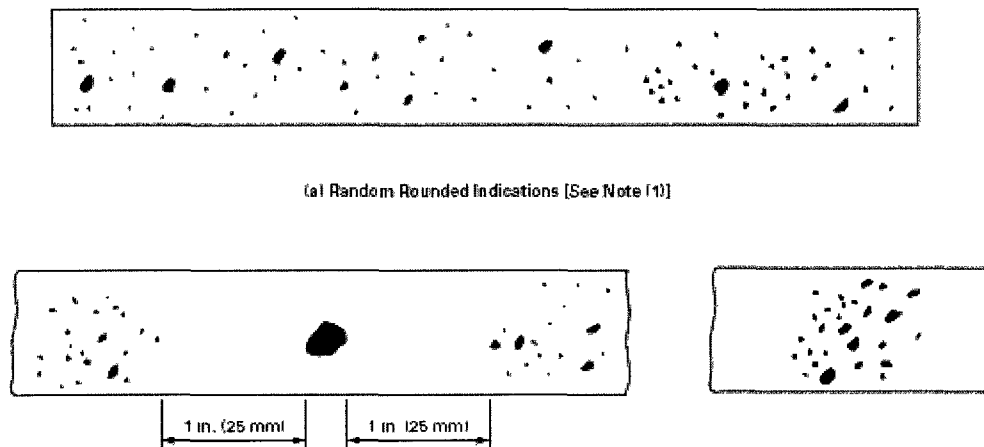
Notes to Figure 7.5

1. ΔT ID-IF \equiv temperature difference between point on ID surface and point on interface along same radial line
2. ΔT ID-MID \equiv temperature difference between point on ID surface and point mid depth of base material along same radial line

7.4.2 Radial Temperature Model – Defect Present

Industry practice recognizes that defect free fabrications are not practical. The practice is to accept pressure vessels, such as a coke drum, with certain known defects that are limited in size and distribution. The term used for these acceptable defects in pressure equipment is “rounded indication”. Figure 7.6 is taken from [3] and specifies the maximize size and distribution of rounded indications in the fabrication welds.

Figure 7.6 Rounded Indications Chart Acceptance Standard in Welds



Notes to Figure 7.6

1. For material thickness over $\frac{3}{4}$ inch to 2 inch, inclusive [19 mm to 50.8 mm]
2. Maximum size for isolated indication is $\frac{1}{4}$ " [6.4 mm] diameter, lower left chart
3. Table limiting defect size is given in [3]

The role of stress and strain concentrations in causing failures in equipment under cyclic loading is well recognized [35, 36, 66]. The severity of a defect is dependant on its geometry. A range of values may be determined if the specific size and distribution of these defects is known. For illustration, assuming that a specific sized ellipsoidal defect within the limits of acceptance given in Figure 7.6 is present, a non-conservative stress concentration value of 2.3 may be established using [67]. By the methodology used in paragraph 6.5.3 above, the calculated fatigue life for the two spectra presented in Figure 6.8 and Figure 6.9 is determined to be 1,076 and 1,635 cycles. Table 6.2 is presented as Table 7.3 and includes consideration of such a defect present in the weld.

Table 7.3 Comparison of Cyclic Life Determinations for Coke Drum Shell

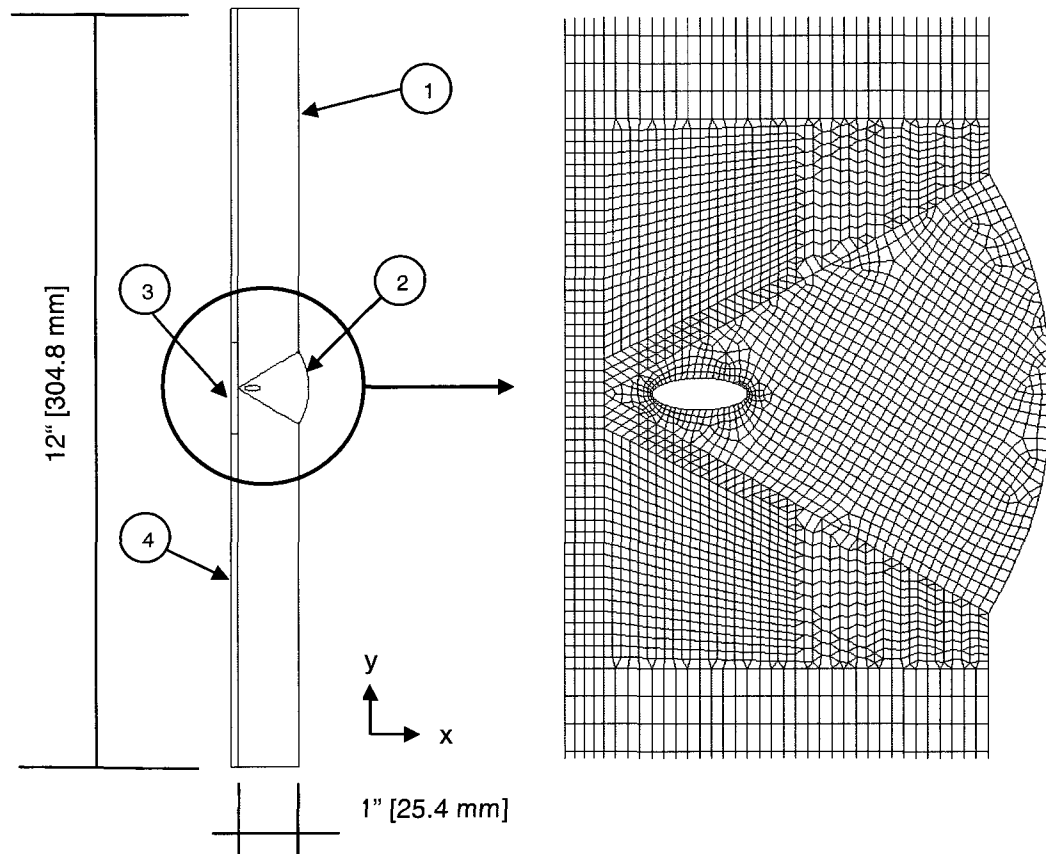
	Strain Profile Distribution [cycles]	
	Figure 6.9	Figure 6.8
Uncorrected, as measured [1]	93,205	99,970
7,200 ue upper bound [2]	28,593	73,490
14,400 ue upper bound [3]	4,603	3,948
with $K_e = 2.3$ [4]	1,635	1, 076

Notes to Table 7.2

1. Uncorrected, as measured \equiv refers to the strain or stress profile as presented in the reference
2. 7,200 ue upper bound \equiv an upper bound strain limit defined in Table 6.1
3. 14,400 ue upper bound \equiv an alternate upper bound strain limit defined in Table 6.1
4. $K_e \equiv$ stress or strain concentration, calculated as 2.3 from Table 7.5 for an assumed, acceptable rounded indication allowed per industry practice

Figure 7.7 is the axisymmetric model for the thermal finite element model illustrating the prototype defect. An elliptical shape was chosen arbitrarily. Placement was made near the weld root for conservatism due to the dissimilar materials of construction and the dissimilar weld joint.

Figure 7.7 Axisymmetric FEA Model with Defect in Circumferential Weld

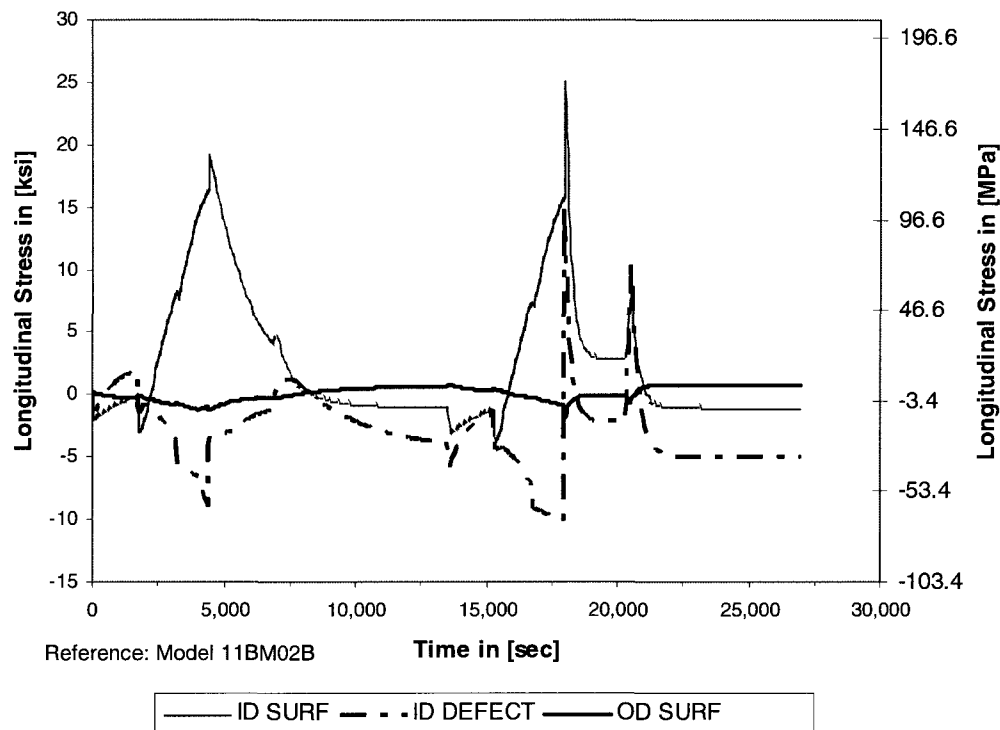


Notes to Figure 7.7

1. Model element is a 2D axisymmetric stress element with two translational degrees of freedom per node
2. The base material thickness is taken as 1" [25 mm] thick, clad liner is 0.100" [2.54 mm] thick
3. Four distinct metallurgical and geometric areas are modeled, 1– base material, 2 – base material weld , 3 – clad restoration weld, 4 – clad liner
4. The differing metallurgical areas are considered fully bonded with no transition properties
5. Displacement boundary conditions are to fix the bottom edge [$y = 0$] against vertical displacement, the top edge is constrained to remain plane as vertical displacement occurs due to thermal displacement, and free, unconstrained displacement in radial direction [x] is allowed
6. A multi-discipline analysis is completed which requires determination of temperatures and using these as the loads for the stress analysis

The stress profile given in Figure 7.8 shows the results from adding a defect in the weld close to the cladding. The dimensions of the defect are considered acceptable per industry practice.

Figure 7.8 Stress Profile for Axisymmetric Model with Defect



Notes to Figure 7.8

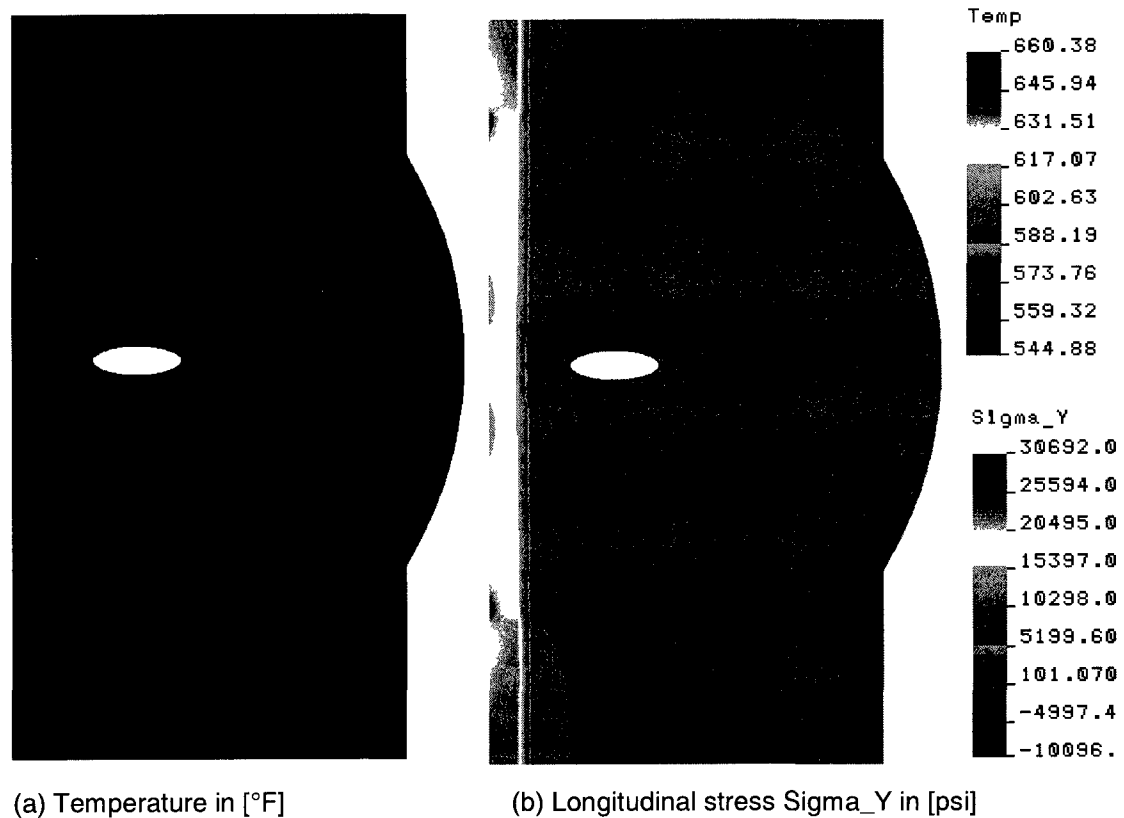
1. ID SURF \equiv a node location at ID surface of model
2. ID DEFECT \equiv the node location on major axis of the elliptical defect nearest to surface representing the ID surface
3. OD SURF \equiv a node location on the surface representing the OD surface
4. The three nodes of interest are collinear along a radial line.

The additional observations from this model are

1. The OD surface stress is altered by the presence of an internal defect showing slightly less sensitivity to temperature loading, a minimum stress of -10,000 psi [-69.0 MPa] compared to a stress of -12,500 psi [-86.2 MPa] in Figure 7.2.

-
2. The stress at the ID DEFECT node location is influenced by the rate of temperature loading showing a spiking in the second cycle when an accelerated temperature loading is applied
 3. The sudden reversal is not due to the presence of the defect, but is a result of the temperature distribution during the more severe transient caused by the accelerated loading. The magnitude of the stresses at the defect is related to the presence of the defect, i.e. a stress concentration. See Figure 7.9 and Figure 7.10 showing the temperature and stress profiles immediately prior to and immediately subsequent to the start of accelerated thermal loading.

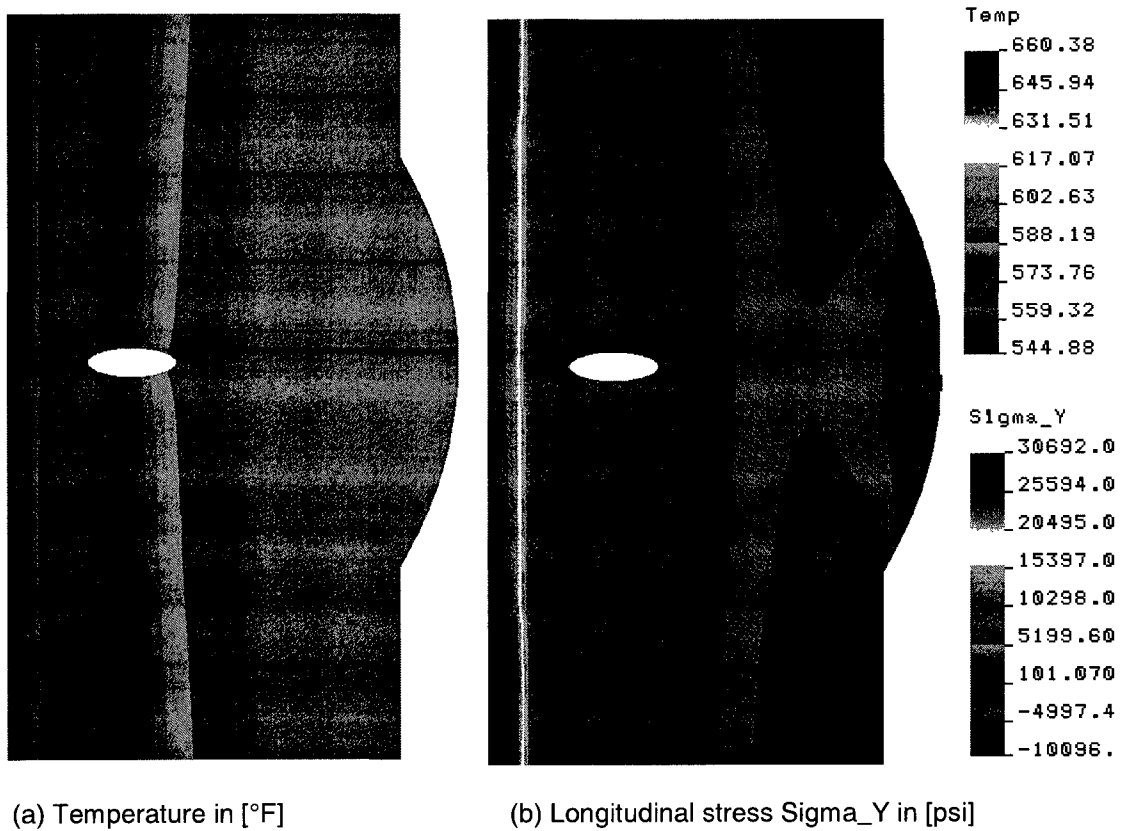
Figure 7.9 Temperature - Stress Comparison with Defect
[time = 17,901 sec]



Notes to Figure 7.9

1. Profiles are at time = 17,901 sec, coinciding with minimum stress determination of -10,096 psi [-69.6 MPa] at the left side edge of the elliptical defect, prior to accelerated temperature loading.

Figure 7.10 Temperature - Stress Profile Comparisons [time = 17,965 sec]



Notes to Figure 7.10

1. Profiles are at time = 17,965 sec, coinciding with maximum stress determination of -15,124 psi [104.3 MPa] at the left side edge of the elliptical defect, subsequent to start of accelerated temperature loading.

7.5 Longitudinal Temperature Loading Model

A long length axisymmetric model is shown in Figure 7.11. The model is intended to investigate more accurately the effects during the water quench step, namely

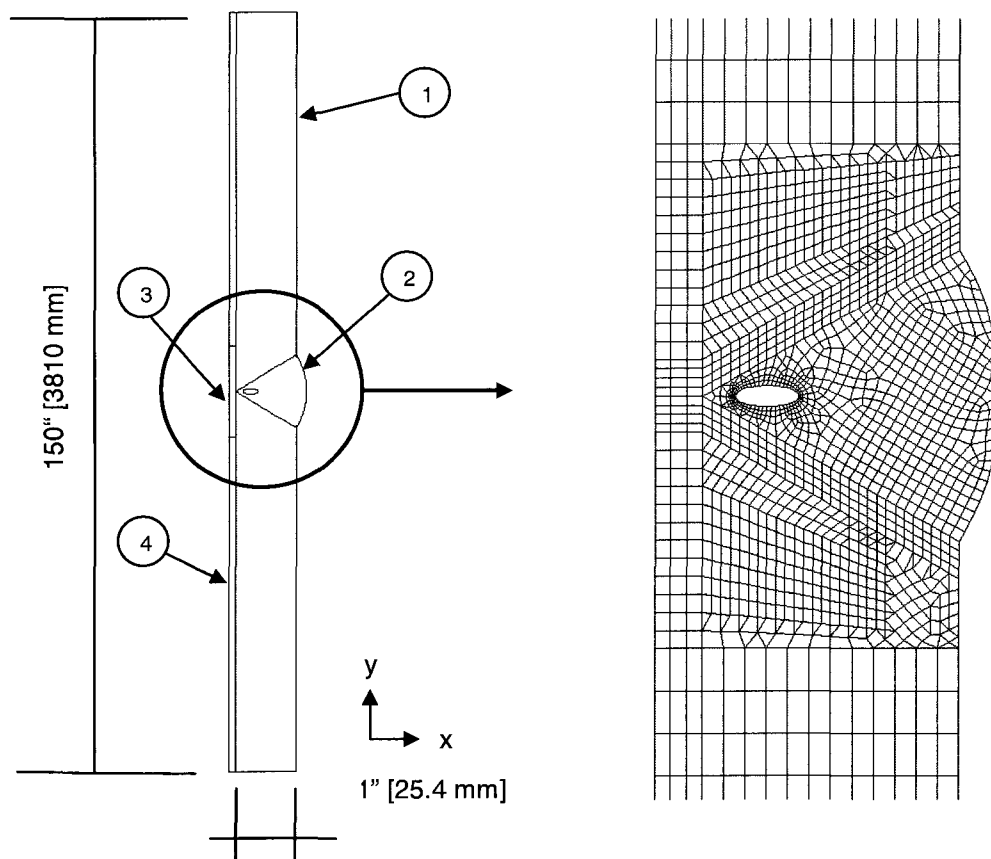
- an axial thermal gradient occurs as water fills the coke drum vessel
- a mechanical bending load occurs as the vessel contracts and causes the radius of the vessel to decrease in response to the decreasing temperature at the lower elevation as quench water fills the coke drum vessel

As stated before, the radial model was posed to only examine the temperature effect as it acted through-thickness. The long length model provides a means to examine additional loads caused by the axial temperature gradient.

The model is as per the short axisymmetric model depicted in Figure 7.7, but extended to a height of 150" [3810 mm] in order to allow simulation of a rising water level in a shell course height of ~120 " [~3048 mm]. A water level rise of 2 inches per minute [50.8 mm] is imposed to provide an upper bound estimate and for practicality of modeling. This value is somewhat less than the nominal water fill rate rise of 2¾ inch [70 mm] per minute so that results will need to be interpreted accordingly. At this time in the operational sequence, the coke drum is filled with a coke residual that is of variable porosity, contains discontinuous flow channels, and with coke drum shell temperatures ranging from at least 650 °F [343 °C] to 850 °F [454 °C]. The effect on drum shell temperatures is evident in Figure 5.1 where a drum shell temperature rise is seen to occur about midway during the water quench step. This effect could be physically interpreted to be a location where water has migrated and then evaporated due to collapse of the flow channel. Thus, water fill may have occurred initially very quickly and subsequently reduced or even blocked for a period of time. Temperature variations of greater or lesser severity occur at each cycle.

The first cycle uses the nominal heat transfer coefficients established in Table 5.4. The second cycle uses the heat transfer coefficients that have been increased to simulate an accelerated temperature loading, as described in section 7.4. The mesh density is reduced slightly to help computational turnaround. A two step procedure is required wherein a thermal FEA is completed which then is input into the stress FEA model.

Figure 7.11 Long Axisymmetric FEA Model with Defect in Weld

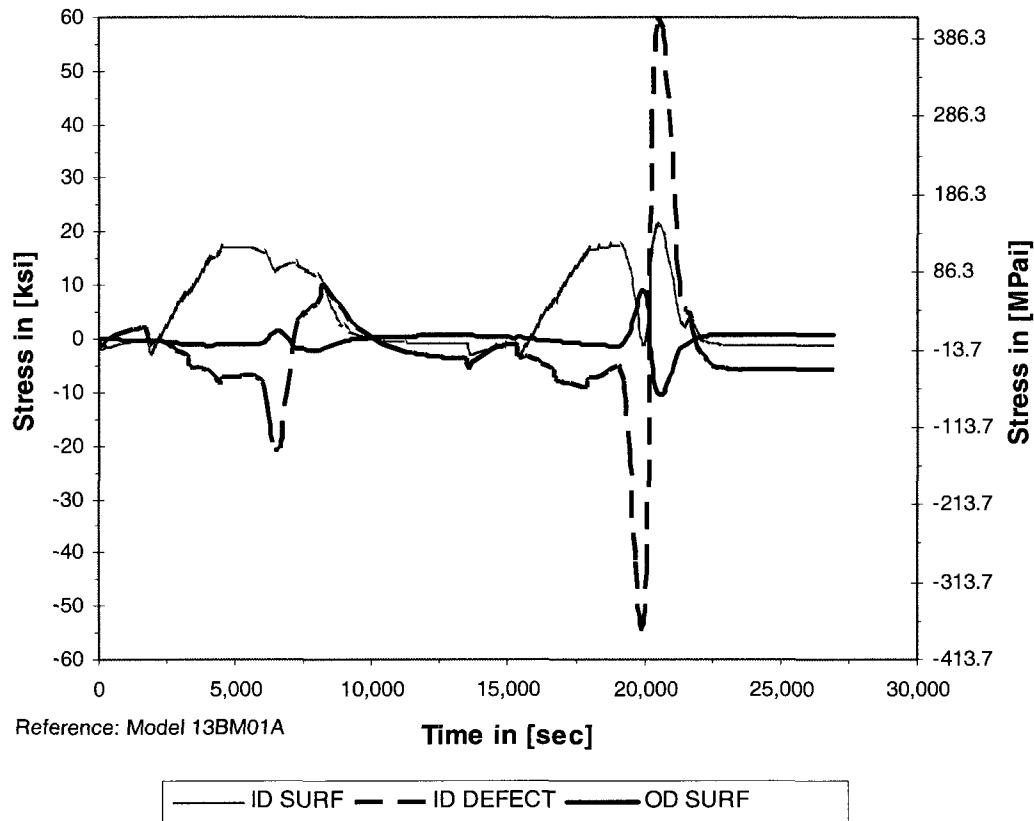


Notes to Figure 7.11

1. Model element is a 2D axisymmetric stress element with two translational degrees of freedom per node
2. The base material thickness is taken as 1" [25 mm] thick, clad liner is 0.100" [2.54 mm] thick
3. Four distinct metallurgical and geometric areas are modeled, 1– base material, 2 – base material weld, 3 – clad restoration weld, 4 – clad liner
4. The differing metallurgical areas are considered fully bonded with no transition properties
5. Displacement boundary conditions are to fix the bottom edge [$y = 0$] against vertical displacement, the top edge is constrained to remain plane as vertical displacement occurs due to thermal displacement, and free, unconstrained displacement in radial direction [x] is allowed
6. A multi-discipline analysis is completed which requires determination of temperatures and using these as the loads for the stress analysis
7. The validity of using a 2D axisymmetric model to represent a 3D feature is addressed below

The stress range experienced by the defect increases for both nominal temperature and accelerated temperature loading as shown in Figure 7.12. This is in conformance to expectation as both a longitudinal temperature gradient is imposed as well as a mechanical bending load due to the difference in radius between the lower, cooled portions of shell versus the upper, hotter portions of shell. The latter has been called the vasing effect. [8, 20, 68]

Figure 7.12 Stress Profile for Long Axisymmetric FEA Model with Defect



Notes to Figure 7.12

1. ID SURF \equiv a node location at ID surface of model
2. ID DEFECT \equiv the node location on major axis of the elliptical defect nearest to surface representing ID surface
3. OD SURF \equiv a node location on the surface representing the OD surface
4. The three nodes of interest are co-linear

The observations from the model shown in Figure 7.12 are

1. The ID surface stress is comparable to the stress results presented in Figure 7.2 and Figure 7.8.
2. The OD surface stress is comparable to the stress results presented in Figure 7.2 and Figure 7.8. There is a sine wave type response corresponding to the imposition of the axial temperature for both the nominal temperature loading and accelerated temperature loading.

-
3. The simulation of an accelerated water quench rate occurring as an axial loading is justified on the basis of there being a confined liquid column rising against the coke drum shell for a portion of the height. As previously stated, severe variations in drum shell temperature were measured by Ramos et al. [15].
 4. The accelerated load cycle stress results at the defect have approached a stress range of $\pm 60,000$ psi [414 MPa]. Referring to Figure 4.3, we see the monotonic curve shows strain well into the plastic stress regime. Due to cyclic hardening, repeated cycling will cause the stress-strain response to return to the elasto-plastic regime.

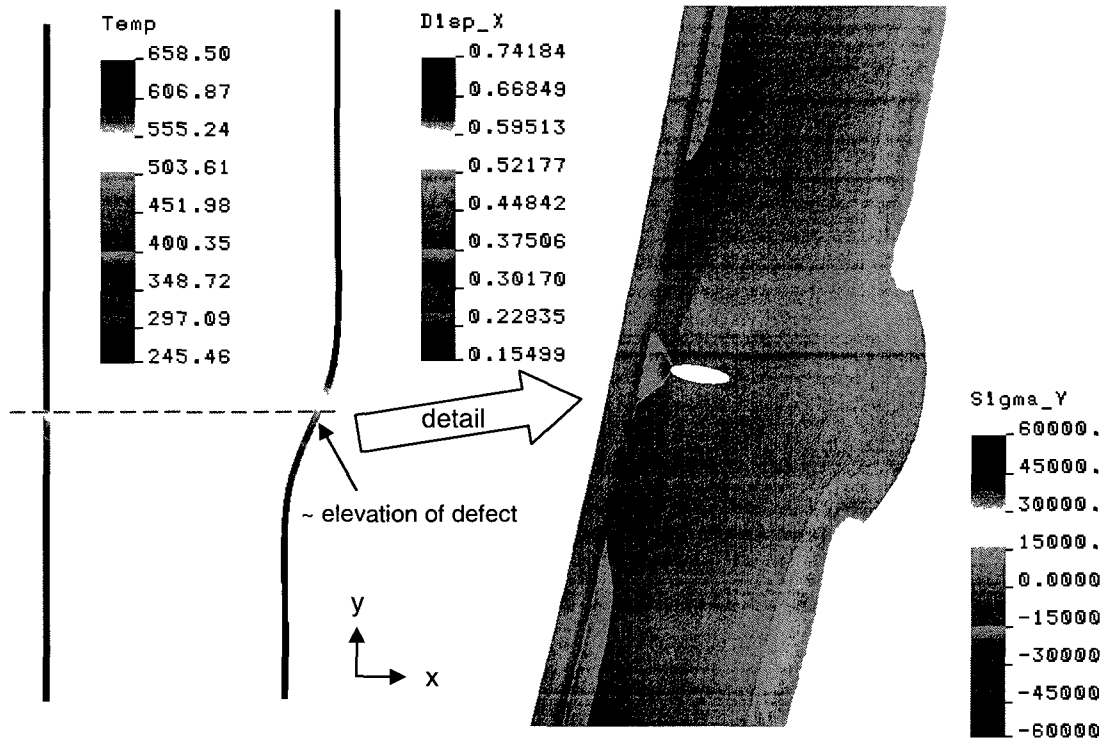
In each of Figure 7.13 and Figure 7.14, the following plots are presented to illustrate the condition of the shell as the temperature wave progresses from bottom to top of the modeled shell section

- temperature plot
- radial displacement plot
- longitudinal stress plot detailed at defect

prior to passage of the temperature wave and then subsequent to passage of the temperature wave.

The snapshots reflect temperature and displacement states associated with the minimum stress state occurring prior to passage of the temperature wave and the temperature and displacement states associated with the maximum stress state occurring subsequent to passage of the temperature wave.

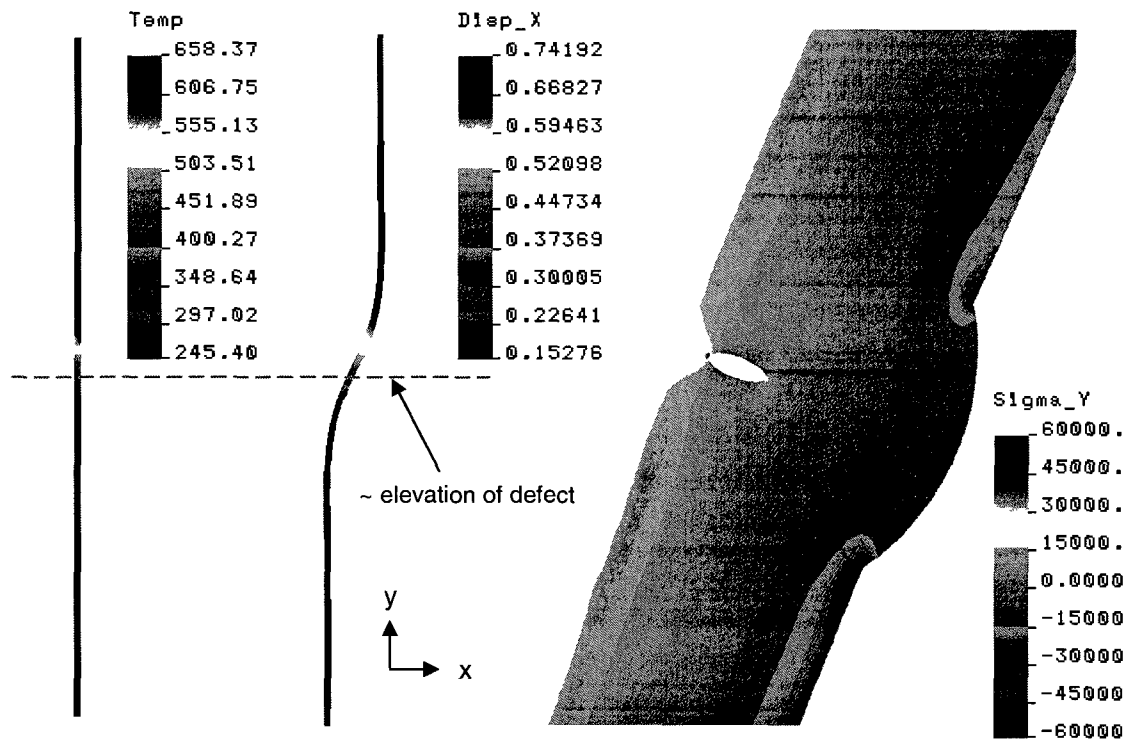
Figure 7.13 Thermal – Displacement – Detailed Stress Profiles at 19,868 sec



Notes to Figure 7.13

1. Time coincides with minimum stress value depicted in Figure 7.12
2. Temp \equiv temperature in [°F]
3. Disp_X \equiv displacement in radial direction in [inches]
4. SIGMA_Y \equiv stress in axial / longitudinal direction in [psi]

Figure 7.14 Thermal – Displacement – Detailed Stress Profiles at 20,468 sec



Notes to Figure 7.14

1. Time coincides with maximum stress value depicted in Figure 7.12
2. Temp \equiv temperature in [°F]
3. Disp_X \equiv displacement in radial direction in [inches]
4. SIGMA_Y \equiv stress in axial / longitudinal direction in [psi]

7.6 Reconciliation of Measured to Calculated Data

In Table 7.4, the measured stresses and strains as given in the references are tabulated along with the calculated quantities from the closed form and numerical modeling. The corresponding strain or stress is simply calculated in order to facilitate a notional comparison. Detailed comparison is not meaningful due to the lack of accuracy listed in the field data, previously.

Table 7.4 Comparison of Measured to Calculated OD Surface Behaviour

	stress [ksi]		strain [ue]		comments
	max	range	max	range	
field data					
[8]	[37.2]	[52.0]	1,215	1,699	axial direction
[49]	[23.0]	[78.0]	750	2,550	axial direction
[48]	60	60	[1,960]	[1,960]	axial direction
Boswell [18]	120	120	[3,922]	[3,922]	axial direction
Ramos [15]	[104.0]	[104.0]	-	3,400	direction, not stated
models					
[6.11, $\Delta T = 350\text{ F}^\circ$]	[154.2]	[308.5]	5,040	10,080	bi-directional
[6.12, $\Delta T = 500\text{ F}^\circ$]	[220.3]	[440.6]	7,200	14,400	bi-directional
fea					
radial	2.5	15.0	[82]	[490]	axial
longitudinal	10.0	20.0	[328]	[654]	axial

Notes to Table 7.4

1. Data shown in [] is computed from corresponding stress or strain quantity to facilitate comparison between reported primary quantities by various authors.
2. Table 7.3M provides the data in SI units, following

The numerical computations significantly under report OD stresses in comparison to the upper bound closed form models and the measured [imputed] stresses. The measured stresses by [15, 18] do compare favourably to the upper bound closed model. Unfortunately, it is not known whether or how, in each instance, these measured values were conditioned to account for the thermal strain experienced by the drum shell. In reviewing the calculated strains for the numerical models, note that these values correspond well with the nominal strains depicted in Figure 6.3 and Figure 6.4.

In order to make this comparison, the suspected thermal strains need to be deducted from the full strain measured during the water quench period and the resulting strain then is comparable to the calculated strains given in Table 7.4. In Figure 6.3, the apparent thermal strain range appears to be 600 ue; deducting this from a total strain range of 1000 ue results in a strain range of 400 ue. In Figure 6.4, the apparent thermal strain range appears to be 500 ue; deducting this from a total strain range of 1100 ue results in a strain range of 600 ue. These values compare well with the strain ranges listed for the numerical models.

An important observation from Table 7.4 is that the largest strains and stresses do not occur at the OD surface. As indicated in Figure 7.2, Figure 7.8 and Figure 7.12, the largest stresses [and, corresponding strains] occur at the ID surface and at interior defects. These locations are not accessible to direct field measurement.

From Figure 7.12, the stress range experienced by the defect is 120 ksi [827.4 MPa] or equivalently, a strain range of 4,000 ue and occurs simultaneously with an OD surface stress range of 20 ksi [137.9 MPa]. From Table 7.4, the surface stresses could be as much as an order of magnitude larger according to the two closed form models being used to upper bound the results. This would result in a maximum stress value leading to failure in a several hundred cycles [using Figure 6.7]. A more rigorous computation, accounting for plasticity at the defect tip is not warranted at this time for reasons already stated. This line of reasoning supports the argument that interior defects are a significant source of structure failure within the time spans being experienced by this equipment.

Table 7.4M Comparison of Measured to Calculated OD Surface Behaviour

	stress [MPa]		strain [ue]		comments
	max	range	max	range	
field data					
[8]	[256.5]	[358.5]	1,215	1,699	axial direction
[49]	[158.6]	[537.8]	750	2,550	axial direction
[48]	413.7	413.7	[1,960]	[1,960]	axial direction
Boswell [18]	827.4	827.4	[3,922]	[3,922]	axial direction
Ramos [15]	[717.1]	[717.1]	-	3,400	direction, not stated
models					
[6.11, $\Delta T = 194\text{ C}^\circ$]	[1063.2]	[2126.3]	5,040	10,800	bi-directional
[6.12, $\Delta T = 278\text{ C}^\circ$]	[1518.9]	[3037.8]	7,200	14,400	bi-directional
fea					
radial	17.2	103.4	[82]	[490]	axial
longitudinal	69.0	137.9	[328]	[654]	axial

Notes to Table 7.3M

1. Data shown in [] is computed from corresponding stress or strain quantity to facilitate comparison between reported primary quantities by various authors.
2. Table 7.3 provides the data in US Customary units, above

7.7 On Modeling of a Non-axisymmetric Defect

For simplicity, an axisymmetric model was used to estimate stresses. The model is a 2D depiction of a structure with an axis of symmetry about its longitudinal axis and thus, is meant to extend 360 degrees about its longitudinal axis. The defect, as depicted in the axisymmetric models does not represent a true defect that would exist in the structure. The quality assurance requirements of actual fabrication preclude the existence of such a defect. However, the axisymmetric model is convenient and efficient, and its construct is effective in providing a reasonable estimate to the three dimensional structure.

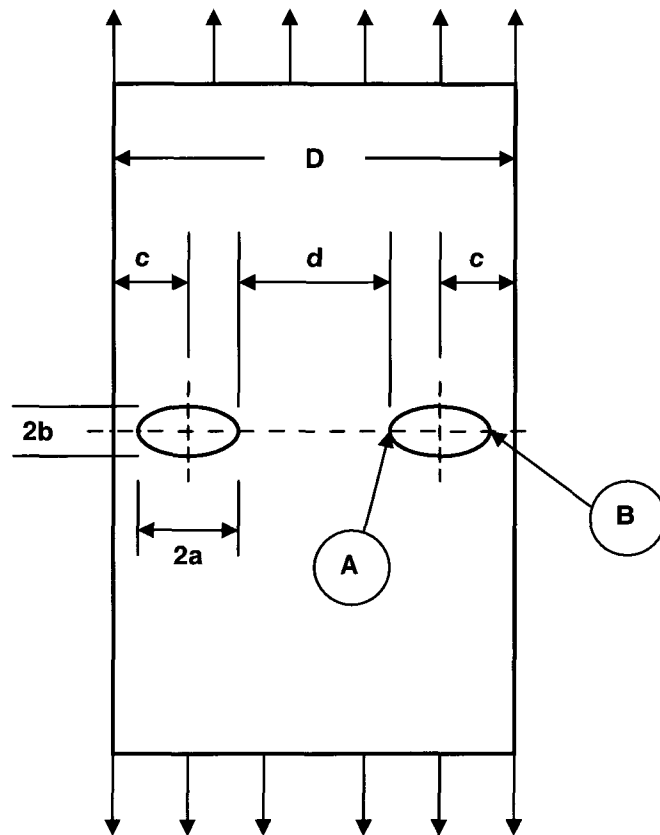
Dowling [39] gives the stress concentration factor at the edge of an elliptical opening in a wide, two-dimensional plate under uniaxial loading, normal to the major axis as

$$\sigma_y = S \cdot \left(1 + 2 \cdot \frac{a}{b} \right) \quad [7.6]$$

where, a and b represent the length of major to minor axis, and the maximum stress σ_y represents the maximum stress parallel to the direction of loading.

Hanus and Burger [69] extend this model to the case where the elliptical flaw is near the free surface of a finite width plate. The motivation for the experimental study was recognition of shallow-buried defects in structures. The aim was to determine the interaction between holes and free edges. The experimental study investigated elliptical holes close to each edge of a tension plate. The holes were symmetric with respect to the longitudinal axis of the models and had their major axes normal to the edge of the plate. The ellipse ratio and distance between centre of the ellipse and the free edge were varied.

Figure 7.15 Geometric Model for Experimental Photoelastic Studies of Hanus [64]



The parameter “c” in Table 7.5 is the distance from the centre of the ellipse to the free edge.

Table 7.5 Stress Concentration Factors for Elliptical Hole Models

a/b	a/c	Hanus [69]		Dowling [39]
		SCF @ B	SCF @ A	SCF @ either edge
3	0.50	5.95	5.81	7
	0.58	7.27	6.19	7
	0.67	7.01	6.36	7

Since the biaxial stress field in the coke drum may be bound between a ratio of 2:1 and 1:1, depending upon the source of loading, we may also bound the maximum stress at an elliptical void of 3:1 ratio in a cylinder, assuming linear elastic conditions and using the expression of Dowling [39], as follows:

For a 2:1 biaxial stress field –

$$\sigma_y = S \cdot \left(1 + 2 \cdot \frac{a}{b}\right) - \frac{S}{2} = S \cdot \left(\frac{1}{2} + 2 \cdot \frac{a}{b}\right) = 6.5 \cdot S \quad \text{and,} \quad [7.7]$$

for a 1:1 stress field

$$\sigma_y = S \cdot \left(1 + 2 \cdot \frac{a}{b}\right) - S = S \cdot \left(2 \cdot \frac{a}{b}\right) = 6.0 \cdot S \quad [7.8]$$

Referring to Figure 7.14, the nominal longitudinal far-field stress is 11,500 psi [79.3 MPa]. The maximum longitudinal stress at the edge of the 3:1 elliptical flaw is 59,400 psi [409.6 MPa] resulting in an apparent stress concentration factor of

$$SCF = \frac{S}{\sigma_y} = \frac{59,400}{11,500} = 5.2 \quad \left[\frac{409.6}{79.3} = 5.2 \right] \quad [7.9]$$

Therefore, the axisymmetric numerical model is not conservative regarding the determination of stresses at the elliptical defect and understates the maximum stress developed at the defect.

The work of Sadowsky [67] provides exact, closed forms solutions for the stress distribution around a general triaxial ellipsoidal cavity in an infinite elastic body in a uniform state of stress. Table 7.6 summarizes stress concentration factors for various ratios of ellipsoid dimensions in uniaxial and biaxial stress fields.

Table 7.6 Stress Concentration Factors for Ellipsoidal Cavity of Varying Ratios

Stress Field [2]		Ratio of axes [1]			
		1 : 1 : 1 [3]	1 : 1 : ½	1 : 3 : 3	1 : 3 : 20
SCF	1:0	2	2.5	5.3	7.5
	2:1	1.9	2.4	4.8	6.9
	1:1	1.8	2.3	4.3	6.3

Notes to Table 7.6

1. Ratio of axes as aligned with model directions – longitudinal : tangential : radial
2. Uniaxial stress field, 1:0; bi-axial, 2:1; biaxial, 1:1
3. Physical interpretation of defect ratio dimensions
 - 1 : 1 : 1 \equiv a spheroidal defect [included for comparison] appearing as a rounded indication on RT film
 - 1 : 1 : ½ \equiv an ellipsoidal defect but appearing as a rounded indication on RT film
 - 1 : 3 : 3 \equiv an ellipsoidal defect and appearing as an elliptical defect on RT film
 - 1 : 3 : 20 \equiv an elongated ellipsoidal defect and appearing as an elliptical defect on RT film, physically this would be a pinhole, weld sidewall lack of fusion, lack of fusion between adjacent weld passes or lack of filling at root all depending on the ratio of dimensions for the specific defect
4. Industry practice allows for indications with a maximum length of three times the width or less on the radiograph to be defined as rounded indications.

The elliptical defect used in the axisymmetric model is best compared using the 1:3:3 axes ratio for the ellipsoidal defect and thus the range of theoretical SCF's of 4.3 to 5.3 also compare favourably with the model SCF of 5.2. Therefore, the model represents a conservative assessment of the defect.

This establishes the suitability of using a 2D axisymmetric numerical model to examine the biaxial stress fields in the actual, 3D structure under linear elastic conditions where superposition holds. Referring to Table 4.2, the measured yield point strength of 64.4 ksi [444.0 MPa] is well in excess of the specified minimum yield strength of 35.0 ksi [241.3 MPa]. At 800 °F [427 °C], the yield point strength reduces to 50.0 ksi [344.7 MPa]. Therefore, some plasticity effects are anticipated at the higher temperatures but the suitability of the approach is generally adequate for this effort.

7.8 Summary

Numerical models were developed to examine the upper bound strain and stress determinations from the closed form solutions presented in Chapter 6. As detailed in that chapter, various expressions and assumptions used in industry practice were found to be incorrect or deficient.

Two axisymmetric models were used. The first model was a short length model to test aspects of the radial thermal loading. The clad interface stress from differential thermal expansion due to differences in the coefficient of expansion of clad to base material caused large stresses at the higher operating temperatures. The calculated values compare well to the closed form expression which accounts for relative thickness, coefficient of expansion and Young's modulus of both clad and base materials. This model also illustrated the impact of accelerated heat transfer during the quench phase of operation and indicates transient heat transfer conditions must be taken into account.

The second numerical model consisted of an extended length model and examined the effects of a longitudinal temperature loading which simulated a rising liquid level.

Both models contained a simulated defect allowed by industry practices. The models examined the effect of nominal and accelerated heat transfer rates and illustrated the more severe impact of the defect under accelerated longitudinal temperature loading where shell distortion would occur over a shorter longitudinal length in comparison to the length over which distortion occurs under nominal loading.

A reconciliation was made to show the ability of the two dimensional axisymmetric model to adequately reflect the stress regime at an internal three dimensional defect to expedite this portion of the work.

CHAPTER 8 CONCLUSIONS

The primary objective of this thesis was to identify the leading failure mechanism causing shell cracking in the vertical, cylindrical side shell of a coke drum.

Data was retrieved from site installations which provided operational data concerning the various fluid streams temperatures and pressures and the time durations for the various operational phases during an operating cycle. Data was also retrieved for measurements of shell metal strains and temperatures during the operational phases.

Properties for the materials of construction for coke drum were retrieved from the literature. Industry practice is to base material strengths on the specified minimum values for tensile and yield strength. From the experimental work, it was found that actual material strengths are much greater than the minimums mandated for use by industry practice.

Various loadings were identified and evaluated for potential to cause cracking damage to the coke drum shell. Pressure loading, live weight loading and dead weight loading were shown to be unlikely causes leading to shell cracking. Thermal loading was demonstrated to be the leading failure mechanism causing shell cracking in a number of ways.

The evaluation methods being used to assess the thermal loading in industry practice were found to be incorrect. The major deficiencies found, included

- inconsistent measurement of shell temperatures
- incorrect assessment of thermal strains as mechanical strains
- incorrect calculation of stresses from measured strains

To advance the work of this thesis, an upper bound estimate approach was taken to evaluate the thermal loads. This involved examining closed form solution methods and numerical analysis. Input variables were taken from measurements that were reasonably accurate, such as fluid stream temperatures and shell metal temperatures that were correctly determined. The closed form solution methods found in the literature were examined and were found to require modification to better account for multi-axial strain and stress effects. This resulted in much larger strain and stress values being derived than given in the literature. These values were then evaluated for the normalized strain distribution values cited in the literature. The presumption was that although the measured values were incorrect, the distribution could be taken as reasonably correct. Evaluation on this basis provided fatigue life comparable to the industry survey data.

Numerical analysis was then performed. Comparable results to the closed form solution approach were found for the determination of clad interface stresses. Numerical analysis was also used to evaluate the effect of internal fabrication defects, called rounded indications. It was found that defects in the vicinity of the clad interface were strongly influenced by the stresses developed in the clad during thermal loading and also by the intensity of shell distortion during a thermal transient associated with rising liquid level. However, the calculated stresses and associated strains were less than those associated with the formation of localized “hot” and “cold” spots occasioned by system fluid hydraulics effects occurring during the water quench operational phase.

Thermal loading is the governing load affecting the fatigue life of coke drum shells. These loadings occur on account of the construction design and operational requirements of the process unit. Specifically, including:

1. the use of clad plate results in high stresses caused by differential thermal expansion between the TP 410S SS clad liner and the low alloy carbon steel base material
2. the differential thermal expansion occasioned by the use of clad plate causes a change in stress field from a predominant 2:1 biaxial stress field under pressure loading, to a 1:1 biaxial stress field under temperature loading increasing the effective strain occurring in the shell
3. during water quench, a large temperature difference is introduced to the system creating the potential for large thermal stresses when relatively cold water contacts the relatively high temperature shell, this resulting in surface boiling and development of a large temperature gradient at the shell ID surface or “skin” effect
4. the high volumetric flow rate of water quench creates the potential for localized “cold” spots where local portions of the shell are cooled preferentially to adjacent portions of the shell that are not in contact with quench water
5. the large self constraint imposed in the shell due to formation of “hot” and “cold” spots in the vessel shell due to non-uniform and intermittent exposure of the shell to quench water
6. by inducing mechanical loads due to radial distortion in the shell caused by the longitudinal temperature loading

The upper bound closed form solutions and numerical solutions indicate that higher strains and stresses exist in the coke drum shell and align with the $\epsilon - N$ fatigue life methodology for the materials of construction and with the failure survey from industry.

CHAPTER 9 RECOMMENDATIONS FOR FUTURE WORK

The findings presented in this thesis suggests that there are opportunities for future study in the determination and definition of the failure mechanisms leading to coker drum shell cracking, their mitigation and prediction of failure. Possible research opportunities are:

1. further data development of monotonic and cyclic material properties of base material and clad alloy material at elevated temperatures
2. determination of fatigue properties of base material and clad alloy material at room temperature and elevated temperatures
3. determination of alternate materials of construction better suited to high strain, low cycle fatigue failure
4. determination of present status of fabrication quality and characterization of defect populations and consequent contribution to shell cracking
5. determination of present status of non-destructive examination methods of volumetric defects in welding of base materials and clad liner materials of construction
6. further definition of strain concentration effects at elevated temperatures under multiaxial loading
7. better experimental techniques to accurately measure strains and temperatures in actual equipment to allow for improved characterization of structure loading

REFERENCES

1. Little, J.F., Great Canadian Oil Sands Limited, Toronto, Canada "Method of Controlling the Feed Rate of Quench Water to a Coking Drum in Response to the Internal Pressure therein" 1974 US Patent 3,936,358
2. Stress Engineering Services, "2008 Coke Drum Seminar", 18 & 19 Nov 2008, Houston TX
3. ASME, "VIII Division 1 Rules for Construction of Pressure Vessels", 2007 ASME, New York, NY
4. ASME, "Section II Part A Ferrous Material Specifications", ASME Boiler and Pressure Vessel Code for 2007, New York, NY
5. Weil, N.A., Rapasky, F.S. "Experience with Vessels of Delayed Coking Units" Proceedings, v. 38 [III] 214-232 1958 Division of Refining, American Petroleum Institute, Washington, DC
6. Thomas, J.W. "API Survey of Coke Drum Experience" 1980 American Petroleum Institute, Washington, DC
7. API Proceedings "1996 API Coke Drum Survey – Final Report", 1996 American Petroleum Institute, Washington, DC
8. CRD Partner Information Package
9. Samman, M., DuPlessis, P., "The Bulging Intensity Factor (BIF), A technique for assessing the bulging severity of coke drums", RMC-07-100 2007 NPRA Reliability & Maintenance Conference, NPRA Houston, TX
10. ASME, "Section II Part D Properties", ASME Boiler and Pressure Vessel Code for 2001, New York, NY
11. Stewart, C.W., Stryk, A.M., Presley, L., "Coke drum design", PTQ Q3 2006 from website <http://www.cbi.com/about/articles/PTQq32006.pdf> accessed 6 Sep 2008
12. Ellis, P.J., Paul, C.A., "Tutorial: Delayed Coking Fundamentals", Session Paper 29a, AIChE Spring National Meeting, New Orleans, LA March, 1998
13. Elliot, J.D., "Shot Coke: Design & Operations", accessed from http://www.fwc.com/publications/tech_papers/oil_gas/shotcoke.pdf, 7 Sep 2008
14. Ramos, A., Rios, C.C., Vargas, J., Tahara, T., Hasegawa, T., "Mechanical Integrity Evaluation of Delayed Coke Drums", PVP v 359 1997: 291-298 ASME, New York, NY

-
15. Ramos, A., Rios, C.C., Vargas, J., Johnsen, E., Gonzalez, M., "Delayed Coking Assessment Using Field Measurements & FEA", PVP v 368 1998: 231-237 ASME, New York, NY
 16. Penso, J.A., Lattarulo, Y.M., Seijas, A.J., Torres, J., Howden, D., Tsai, C.L., "Understanding Failure Mechanisms to Improve Reliability of Coke Drums", PVP v 395 1999: 243-253, ASME, New York, NY
 17. Kirkpatrick, K.D., Miller, G.A., Millet, B.J., Malek, D.W., Antalffy, L.P., "Transient Profile Development and the Fatigue Impact for Cyclic Thermal Conditions", Proceedings, ICPVT – 10, July 2003, Vienna, Austria
 18. Boswell, R.S., Farraro, T., Sober, M.J., "Remaining Life Evaluation of Coke Drums", 1997 Energy Week Conference and Plant Engineering, Operations, Design & Reliability Symposium ASME / API, Houston, TX
 19. McGowin & White, "Coke Drum Fracture Experience and Analysis", Proceedings / Division of Refining, American Petroleum Institute, v. 51 1971: 778-807
 20. Church, J.M., Lim, L.B., Brear, J.M., Jarvis, P., Lant, R.P.D., Middleton, C.J., "Crack growth modeling and probabilistic life assessment of coke drums operating under fatigue conditions", International Journal of Pressure Vessels and Piping, v 78 2001:1011-1020, Elsevier Science Ltd.
 21. API, "Publication 581 Base Resource Document - Risk Based Inspection", 1st Edition, 2000 American Petroleum Institute, Washington, DC
 22. BSI, "PD 5500:2009 Specification of unfired fusion welded pressure vessels", BSI British Standards London, UK
 23. Clark, R.D., Rutt, D.K., Boswell, R., Allevato, C., Wright, B., "Coke Drum Life Improvement – A Combined Approach", Advances in Coking, 2002 Spring National Meeting, AIChE, New Orleans, LA
 24. Milford, R.E., General Electric Company, United States, "Waveform Recognition System" 1965 Canada Patent CA 701165
 25. Selker, H.P., New England Medical Center Hospitals, Inc., United States, "Device for Determining the Probability of Death of Cardiac Patients", 1993 Canada Patent CA 1323431
 26. Fitness4Service.com website,
<http://www.fitness4service.com/software/MPC.htm> accessed 4 Sep 2008
 27. Material Property Council, from website
<http://www.forengineers.org/mpc/index.html> accessed 4 Sep 2008

-
28. Anderson, T.L., "Software for Life Prediction in Pressure Vessels and Piping", PVP v 380, 1998: 191-196 Fitness for Service Evaluations in Petroleum and Fossil Power Plants, ASME, New York, NY
 29. Rees, D.W.A., "Basic Engineering Plasticity – An Introduction with Engineering and Manufacturing Applications", 2006 Butterworth Heinemann Elsevier, Burlington, MA
 30. Ellyin, F. "Fatigue Damage, Crack Growth and Life Prediction", 1997 Chapman & Hall, London UK
 31. Hoffman, O., Sachs, G., "Introduction to the Theory of Plasticity for Engineers", 1957 McGraw Hill Book Company, New York, NY
 32. ASTM, "E 6 – 06 Standard Methodology Relating to Methods of Mechanical Testing" ASTM, West Conshohocken PA 2006
 33. ASTM, "E 370 – 07 Standard Test Methods and Definitions for Mechanical Testing of Steel Products", 2007 ASTM, West Conshohocken PA
 34. Chandrupatla, T.R., Belegundu, A.D., "Introduction to Finite Elements in Engineering", 1991 Prentice Hall, Englewood Cliffs, N.J.
 35. Collins, J.A., "Failure of Materials in Mechanical Design – Analysis, Prediction and Prevention", 2nd Ed., 1993 John Wiley & Sons, New York, NY
 36. Harvey, J.F., "Theory and Design of Pressure Vessels", 1985 Van Nostrand Reinhold Company, New York, NY
 37. Dill, E.H., "Continuum Mechanics – Elasticity, Plasticity, Viscoelasticity", 2007 CRC Press Taylor & Francis Group, Boca Raton, FL
 38. Del Puglia, A., Manfredi, E., "High-Temperature Low-Cycle Fatigue Damage", Creep of Engineering Materials and Structures, edited by Bernasconi, G., Piatti, G., pp 229 -265 1979 Applied Science Publishers Ltd., London, U.K.
 39. Dowling, N.E., "Mechanical Behaviour of Materials – Engineering Methods for Deformation, Fracture, and Fatigue", 3rd Ed., 2007 Pearson Prentice Hall, Upper Saddle River, N.J.
 40. Duryagin, V.A., Kuslitskiy, A.B., Pistun, I.P., "Development of Slip Bands in Medium-Carbon Steel During Low Cycle Fatigue", vol 50, n 5 p 197 July 1974 Metallurgical Transactions, Metals Park OH
 41. Frandsen, J.D., Paton, N.E., Marcus, H.L., "The Influence of Gaseous Environments on Fatigue Crack Growth in a Nickel-Copper Alloy, vol 5, n7 Jul 1974 Metallurgical Transactions, Metals Park, OH

-
42. Manson, S.S., "Thermal Stress and Low-Cycle Fatigue", 1966 McGraw-Hill Inc., New York, NY
 43. Wundt, B.M., "ASTM STP 490 Effect of Notches on Low Cycle Fatigue – A Literature Survey", 1972 The Metals Properties Council for ASTM, Philadelphia, PA
 44. ASME, "VIII Division 2 Alternative Rules: Rules for Construction of Pressure Vessels", 2007 ASME, New York, NY
 45. ASME, "III Rules for Construction of Nuclear Facility Components", 2007 ASME, New York, NY
 46. Kreith, F., "Principles of Heat Transfer", 3rd Ed., Intext Press Inc., 1973 New York, NY
 47. Ju, F., "Coke Drum Progress Report – Computation of Temperature Field of Coke Drum at Different Processing Stages", Mechanical Engineering Department, U. of Alberta, Edmonton, AB 31 Jul 2008
 48. CRD Partner Information Package – Item 33
 49. CRD Partner Information Package – Attachment 17
 50. Salter, R.A.C., "Engineering Plasticity", 1977 The McMillan Press Ltd., London, Great Britain
 51. Stress Engineering Services, "2008 Coke Drum Seminar", 18 & 19 Nov 2008, Houston TX
 52. Beckwith, T.G., Buck, N.L., "Mechanical Measurements", 2nd Ed, 1973 Addison Wesley Publishing, Reading, MA
 53. Lawton, C.W. "Use of Low Cycle Fatigue Data for Pressure Vessel Design" STP 770 Low Cycle Fatigue and Life Prediction, ASTM Philadelphia, PA 1982
 54. Moguerou, A., Vassal, R., Vessiere, G., Bahuaud, J., "Low Cycle Fatigue under Biaxial Strain", STP 770 Low Cycle Fatigue and Life Prediction, ASTM Philadelphia, PA 1982
 55. Young, W.C., "Roark's Formulas for Stress and Strain", 6th Ed 1989 McGraw Hill Book Company, New York, NY
 56. Sheshadri, R., "Integrity Assessment of Pressure Components With Local Hot Spots", Journal of Pressure Vessel Technology, v 127 pp 137 – 142 May 2005, ASME, New York, NY

-
57. Goodier, J.N., "Thermal Stress", Transactions of the American Society of Mechanical Engineers, v 4 n 1 1937 A 33 – A 36, ASME, New York, NY
 58. Goodier, J.N., "Thermal Stress and Deformation", ASME Transactions Journal of Applied Mechanics, v 24 n 3 1957, ASME, New York, NY
 59. Sonoya, K., Nonaka, I., Kitagawa, M., "Prediction of Creep-fatigue Lives of Cr-Mo Steels with Diercks Equation", ISIJ International, v 31 (1991) n 12 pp 1424 – 1430
 60. Burr, I.W., "Applied Statistical Methods", Academic Press, 1974 New York, NY
 61. Timoshenko, S., "Strength of Materials – Part II", 3rd Ed 1956 Robert E. Krieger Publishing Company, Malabar, FL
 62. WRC, "Bulletin 432 Fatigue Strength Reduction and Stress Concentration Factors for Welds in Pressure Vessels and Piping", June 1998 Welding Research Council, New York, NY
 63. Streeter, V.L., Wylie, E.B., "Fluid Mechanics", 6th Edition 1975 McGraw Hill Boo Company, New York, N.Y.
 64. ASME, "Section II Part C Specifications for Welding Rods, Electrodes, and Filler Metals", ASME Boiler and Pressure Vessel Code 2007, New York, NY
 65. Anderson, T.L., "Fracture Mechanics – Fundamentals and Applications", 3rd Ed CRC Press Taylor & Francis 2005, Boca Raton, FL
 66. Gray, T.G.F., Spence, J., North, T.H., "Rational Welding Design", 1975 Butterworth & Co. Publishers Ltd., London, U.K.
 67. Sadowsky, M.A., Sternberg, E., "Stress Concentration Around a Triaxial Ellipsoidal Cavity", Journal of Applied Mechanics, v 16 issue 2 pp 149 – 157, 1949 ASME, New York, NY
 68. Boswell et al., Citgo Petroleum Corporation, Tulsa, OK "Method of Designing and Manufacturing a Delayed Coker Drum" 1998S US Patent 5,827,403
 69. Hanus, J.B., Burger, C.P., "Stress Concentration Factors for Elliptical Holes Near an Edge", Experimental Mechanics, v 21 n 9 1981 p 336 – 340 Springer Boston, New York, NY

APPENDICES

,

APPENDIX 1

DISCONTINUITY STRESS IN CLAD PLATE

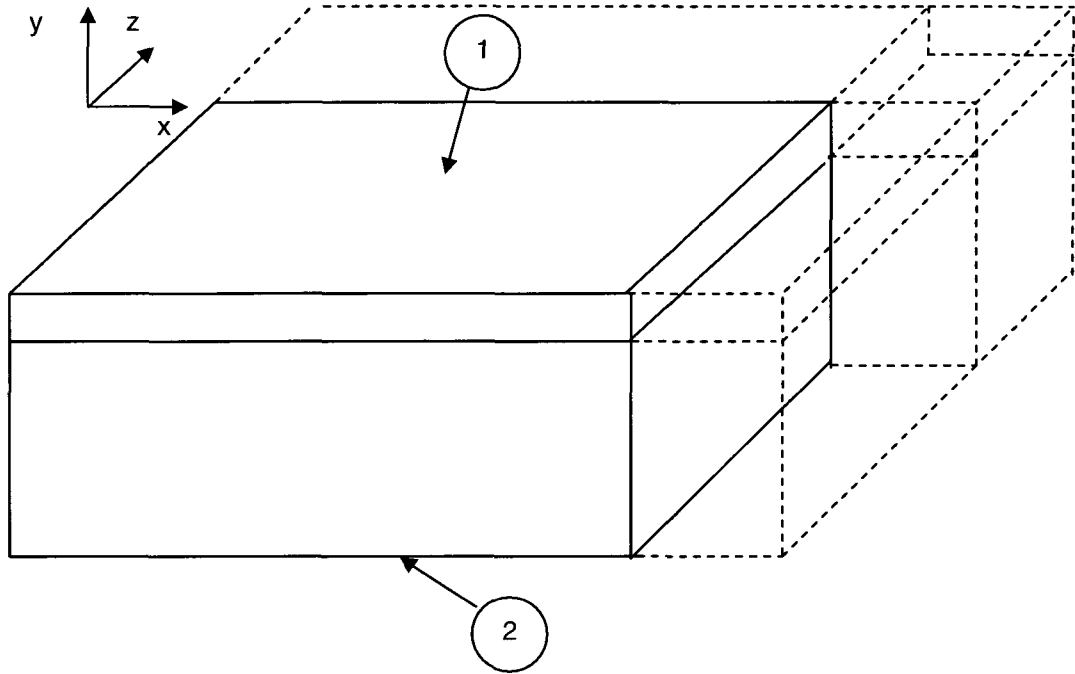
The discontinuity stress between the TP 410S clad and Cr – Mo base material occurs from the difference in coefficient of expansion [CTE] between the two materials when heating occurs, assuming that no stresses exist at ambient temperature. This is likely conservative, as there are likely residual compressive stresses in the clad due to mill fabrication practices for production of clad plate. Most clad plate used in coker drum fabrication is made by the roll bond process, which uses a mechanical rolling technique at high temperature to manufacture the composite plate. The process will leave compressive stresses in the clad plate at room temperature. The magnitude of this compressive stress is not known and was not part of this work. An assumption of zero stress at ambient conditions is conservative.

The development of the expression for a two-dimensional clad plate to examine the resulting biaxial stress state on heating occurs as follows: For the two-dimensional [2D] plate shown in Figure 2.1, a bi-axial stress will occur, that is $\sigma_1, \sigma_2 \neq 0$ and, $\sigma_3 = 0$ when the plate is heated above room temperature and assuming the original biaxial stress state due to temperature is zero. The strain in the plate for each material can be separately described in the x and y directions and are given, since each material is now acted upon by restraint in two directions, as -

$$\epsilon_x = \frac{\sigma_x}{E} - \mu \cdot \frac{\sigma_z}{E} \quad [\text{A1.1}]$$

$$\epsilon_z = -\mu \cdot \frac{\sigma_x}{E} + \frac{\sigma_z}{E} \quad [\text{A1.2}]$$

Figure A – 2 Two Dimensional Stress in Clad Plate



In the case of thermal loading, the strains and stresses are symmetrical, $\sigma_x = \sigma_z$ and, thus for each material,

$$\varepsilon_x = \frac{\sigma_x}{E} - \mu \cdot \frac{\sigma_z}{E} = \frac{(1-\mu)}{E} \cdot \sigma_x \quad [\text{A1.3}]$$

$$\varepsilon_z = -\mu \cdot \frac{\sigma_x}{E} + \frac{\sigma_z}{E} = \frac{(1-\mu)}{E} \cdot \sigma_z \quad [\text{A1.4}]$$

For the 2D case, deformation is constrained such that the final deformation of the clad and base plates must be equal and the internal forces must sum to zero.

Therefore, for a temperature rise to T_1 , in the x – direction the sum of deformation due to thermal expansion plus the deformation due to internal restraint caused by the presence of a second material of differing coefficient of expansion results in –

$$\Delta_{L1-x} + \Delta_{\lambda 1-x} = \Delta_{L2-x} + \Delta_{\lambda 2-x} \quad [\text{A1.5}]$$

$$L_{1-x} \cdot \alpha_1 \cdot (T_1 - T_0) + \sigma_{1-x} \cdot L_{1-x} \cdot \frac{1-\mu}{E_1} = L_{2-x} \cdot \alpha_2 \cdot (T_1 - T_0) + \sigma_{2-x} \cdot L_{2-x} \cdot \frac{1-\mu}{E_2} \quad [\text{A1.6}]$$

and, since $L_{1-x} = L_{2-x}$ i.e., the plates are of equal size and $\sigma_{1-x} \cdot A_{1-x} = -\sigma_{2-x} \cdot A_{2-x}$ from which one obtains –

$$\begin{aligned} \sigma_{1-x} &= \left[(\alpha_2 - \alpha_1) \cdot (T_1 - T_0) \cdot L_{1-x} - \sigma_{1-x} \cdot \frac{A_{1-x}}{A_{2-x}} \cdot \frac{L_{1-x}}{E_2} \cdot 1 - \mu \right] \cdot \frac{E_1}{L_{1-x} \cdot 1 - \mu} \quad [\text{A1.7}] \\ &= \left[(\alpha_2 - \alpha_1) \cdot (T_1 - T_0) \cdot E_1 - \sigma_{1-x} \cdot \frac{A_{1-x}}{A_{2-x}} \cdot \frac{E_1}{E_2} \cdot \frac{1-\mu}{E_2} \right] \cdot \frac{1}{1-\mu} \\ &= \left[\frac{(\alpha_2 - \alpha_1) \cdot (T_1 - T_0) \cdot E_1}{1 + \frac{A_{1-x}}{A_{2-x}} \cdot \frac{E_1}{E_2}} \right] \cdot \frac{1}{1-\mu} \end{aligned}$$

By substitution,

$$\begin{aligned} \sigma_{2-x} &= -\sigma_{1-x} \cdot \frac{A_{1-x}}{A_{2-x}} \quad [\text{A1.8}] \\ &= \left[\frac{(\alpha_2 - \alpha_1) \cdot (T_1 - T_0) \cdot E_1}{1 + \frac{A_{1-x}}{A_{2-x}} \cdot \frac{E_1}{E_2}} \right] \cdot \frac{1}{1-\mu} \cdot \frac{A_{1-x}}{A_{2-x}} \end{aligned}$$

Similar derivation is obtained from consideration of the Z – direction.

As an illustration, use the material properties given in Table 4.1 to determine the discontinuity stress between TP 410S clad and Cr – Mo base material for a plate subject to a temperature rise from 100 °F [38 °C] to 800 °F [427 °C] where the base material [material 1] is 1" [25.4 mm] thick and the clad is 0.118" thick [3 mm] [material 2]. The respective stresses developed during heat up are then:

$$\begin{aligned}\sigma_{1-x} &= \left[\frac{(\alpha_2 - \alpha_1) \cdot (T_1 - T_0) \cdot E_1}{1 + \frac{A_{1-x}}{A_{2-x}} \cdot \frac{E_1}{E_2}} \right] \cdot \frac{1}{1 - \mu} \quad [\text{A1.9}] \\ &= \left[\frac{(7.1 - 8.9) \cdot 10^{-6} \cdot (800 - 100) \cdot 26.3 \cdot 10^6}{1 + \frac{1}{0.118} \cdot \frac{26.3 \cdot 10^6}{24.7 \cdot 10^6}} \right] \cdot \frac{1}{1 - 0.3} \\ &= -3,306 \cdot \frac{1}{1 - 0.3} = -4,723 \text{ psi } [-32.6 \text{ MPa}]\end{aligned}$$

The FEA model following shows a compressive stress of -4,730 psi [-32.6 MPa] in the backing plate. For the clad plate,

$$\begin{aligned}\sigma_{2-x} &= -\sigma_{1-x} \cdot \frac{A_{1-x}}{A_{2-x}} \quad [\text{A1.10}] \\ &= -4,723 \cdot \frac{1}{1 - 0.3} \cdot \frac{1}{0.118} = 40,025 \text{ psi } [276 \text{ MPa}]\end{aligned}$$

Note that for unit widths, A_1 and A_2 may be replaced by t_1 and t_2 . The clad plate experiences a stress of 40,040 psi [276.1 MPa].

The backing plate experiences compressive stress while the clad plate experiences tensile stress on heating where the clad plate coefficient of expansion is less than that for the backing plate.

COMPARISON TO NUMERICAL EVALUATION

The results from a linear elastic FEA evaluation is shown in Figure A -2 and Figure A -3 for the two dimensional plate. For simplicity and direct comparison, the physical properties are taken as constant for the numerical evaluation.

Figure A – 2 Two Dimensional Stress in Bimetal Plate – X Direction

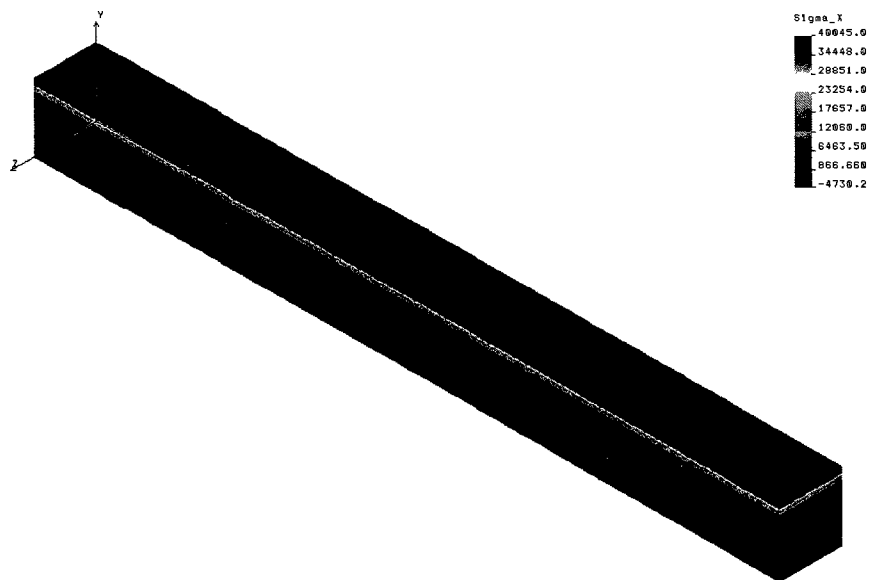
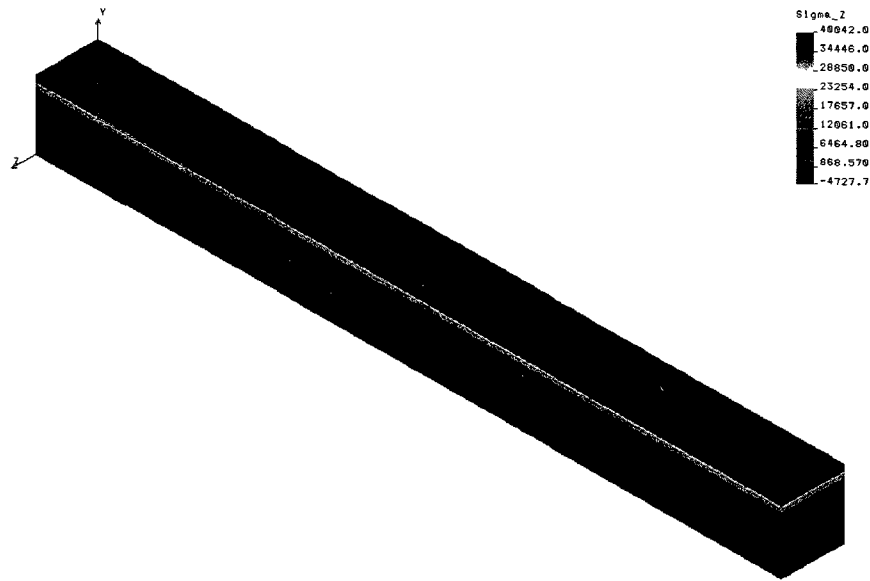


Figure A – 3 Two Dimensional Stress in Bimetal Plate – Z Direction

Lin STRESS Lc=1



Notes

1. Figure A – 2 shows SX stresses, Figure A -3 shows orthogonal SZ stress in horizontal plane.

The maximum tensile stresses shown in Figure A – 2 and Figure A – 3 are equal in both horizontal directions and equal to 40,045 psi [276.1 MPa] which compares very well with the calculated stress in the clad material of 40,025 psi [276.0 MPa].

The maximum compressive stresses shown in Figure A – 2 and Figure A – 3 are equal in both horizontal directions and equal to – 4,730 psi [- 32.6 MPa] which compares very well with the calculated stress in the base material of – 4,725 psi [-32.6 MPa].